

**AN INTEGRATED APPROACH TO THE DESIGN OF
SUPERCAVITATING UNDERWATER VEHICLES**

A Thesis
Presented to
The Academic Faculty

by

Seong Sik Ahn

In Partial Fulfillment
of the Requirements for the Degree
Doctor of Philosophy
in the School of Aerospace Engineering

Georgia Institute of Technology
August 2007

AN INTEGRATED APPROACH TO THE DESIGN OF SUPERCAVITATING UNDERWATER VEHICLES

Approved by:

Dr. Massimo Ruzzene, Committee Chair
School of Aerospace Engineering
Georgia Institute of Technology

Dr. Carlo L. Bottasso
Dipartimento di Ingegneria Aerospaziale
Politecnico di Milano

Dr. Mark Costello
School of Aerospace Engineering
Georgia Institute of Technology

Dr. Dewey H. Hodges
School of Aerospace Engineering
Georgia Institute of Technology

Dr. Neil Weston
School of Aerospace Engineering
Georgia Institute of Technology

Date Approved: 16 April 2007

*To my parents,
for their love and support.
You have helped me to be what I am.*

ACKNOWLEDGEMENTS

I would like to express my sincere gratitude to my advisor, Dr. Massimo Ruzzene for his valuable guidance and support throughout the past five years. His assistance and encouragement has been an essential driving force for me to accomplish my doctoral degree at Georgia Institute of Technology. Especially, I am grateful for his providing great opportunities in many research areas with patience and for his sharing creative insight on the research. Working with him on a broad topic of research has been such a great pleasure to me. I would also like to thank Dr. Carlo L. Bottasso, who has provided valuable insight and suggestions through detailed discussion on this dissertation. In addition, I am grateful to Drs. Dewey H. Hodges, Mark Costello, and Neil Weston for being on my dissertation committee and their constructive comments. I would like to mention that taking Dr. Hodges's dynamics classes has been my delight and it has been very helpful for the work.

There are also many people who have helped me during my pursuit of the doctoral degree. Special thanks go to lab members Sang Min Jeong, Alessandro Spadoni and Stefano Gonella who have showed sincere help and concerns. Particularly, I would like to mention Francesco Scorcelletti's efforts, Dr. Bottasso's graduate student, for developing the maneuvering code (TOP). Also, I would like to extend thanks to all of my colleagues at Georgia Tech, especially to Chong-Seok Chang for a creative and delightful discussion on academic topics, Jieun Ku and Taewoo Nam for valuable suggestions on design problems, Jincheol Ha for discussions on dynamics and control, Chang-Yong Lee and Gilsoo Kim for their sincere help, Dr. Jouyoung Choi for valuable suggestions during my master program. In addition, I would like to thank to many of my classmates at Korea University, especially Jin-Ho Ha for his sincere encouragement that inspired me to further pursue my academic career in graduate school.

I wish to show my love and thanks with greatest gratitude to my parents (Taedong Ahn and Nahmsook Lee) and sisters (Miejeong Ahn, Miera Ahn, Miesook Ahn, and Mieyoung

Ahn) for their love, trust and support.

Contents

DEDICATION	iii
ACKNOWLEDGEMENTS	iv
LIST OF TABLES	x
LIST OF FIGURES	xii
SUMMARY	xvi
I INTRODUCTION	1
1.1 Introduction to Supercavitating Vehicles	1
1.1.1 Dynamics of supercavitating vehicles	3
1.1.2 Control strategies for supercavitating vehicles	5
1.1.3 Structural analysis of supercavitating vehicles	7
1.1.4 Trajectory optimization of supercavitating vehicles	9
1.2 Objectives and Motivation	11
1.3 Outline	11
II FLIGHT MECHANICS MODEL	13
2.1 Overview	13
2.2 Equations of Motion	13
2.3 Cavity Models	16
2.3.1 Munzer-Reichardt’s model	17
2.3.2 Logvinovich’s model	18
2.3.3 Cavity memory effects	21
2.4 Cavitator Force Model	23
2.5 Fin Force Model	24
2.6 Vehicle/Cavity Interactions	27
2.6.1 Tail-slap	28
2.6.2 Hassan’s model for planing forces	28
2.7 Computation of Immersion Depths for Afterbody and Fins	32
2.7.1 Planing immersion depth of the afterbody	32
2.7.2 Fins’ immersion depth	34

2.8	Conclusions	36
III	ANALYSIS OF TRIM CONDITIONS	37
3.1	Overview	37
3.2	Nominal Vehicle Configuration	37
3.3	General Formulation of The Trim Problem	39
3.4	Constraints on Trim Conditions	40
3.4.1	Level flight	41
3.4.2	Turning flight	42
3.5	Practical Implementation of Trim	42
3.5.1	Level flight	44
3.5.2	Turning flight	45
3.5.3	Cavity memory effects	46
3.6	Results for Level Flight	47
3.6.1	Influence of pitch angle and velocity of forward motion	47
3.6.2	Dynamic simulations	51
3.7	Results for Level Turning Flight	59
3.7.1	Influence of angular velocity	60
3.7.2	Cavity memory effects	62
3.7.3	Simulations in level turning flight	62
3.8	Conclusions	69
IV	VEHICLE CONFIGURATIONAL OPTIMIZATION FOR PERFORMANCE IN TRIM FLIGHT	70
4.1	Overview	70
4.2	Formulation of The Optimization Problem	70
4.3	Optimization for Straight Level Flight	71
4.3.1	Range as a performance index	71
4.3.2	Constraints	72
4.3.3	Analysis of parameters sensitivity	73
4.3.4	Results	75
4.4	Optimization for Level Turning Flight	79
4.4.1	Turn rate and load factor	79

4.4.2	Flight envelope limitations	81
4.4.3	V-n diagram	86
4.4.4	Considered performance index	89
4.4.5	Constraints	89
4.4.6	Implementation of optimization procedure	89
4.4.7	Parameters sensitivity	90
4.4.8	Results	91
4.5	Optimization Based on A Combined Performance Index	95
4.5.1	Objective function	95
4.5.2	Implementation of optimization procedure	95
4.5.3	Results	96
4.6	Conclusions	100
V	OPTIMIZATION OF MANEUVERING SUPERCAVITATING VEHICLES	101
5.1	Overview	101
5.2	Overview of the Trajectory Optimization Technique	101
5.2.1	The Maneuver Optimal Control Problem	102
5.2.2	Numerical Solution	103
5.2.3	Implementation issues	104
5.2.4	Examples	106
5.3	Optimization of Maneuvering Vehicles	112
5.3.1	Design variables and objective function	112
5.3.2	Constraints	113
5.3.3	Implementation of optimization procedure	114
5.3.4	Optimization for minimum flight time	115
5.3.5	Optimization for minimum average thrust	119
5.4	Conclusions	125
VI	INTEGRATED VEHICLE OPTIMIZATION	127
6.1	Overview	127
6.2	Formulation of The Optimization Problem	128
6.3	Exploration of the Design Space	129

6.4	A Simple Optimization Strategy	131
6.4.1	Methodology	131
6.4.2	Example	133
6.5	Optimization results	137
6.5.1	Preliminary optimization with reduced set of design variables . . .	137
6.5.2	Optimization with full set of design variables	141
6.6	Conclusions	146
VII	CONCLUDING REMARKS AND RECOMMENDATIONS	147
7.1	Conclusions	147
7.2	Recommendations for Future Research	149
VITA	160

List of Tables

1	Nominal vehicle dimensions.	39
2	Fins-supported straight level trimmed flight.	52
3	Fins and planing-supported straight level trim flight.	56
4	Fins-supported level turning flight.	65
5	Reduced optimal design configuration for fins-supported level flight.	75
6	Performance of reduced optimal vehicle in fins-supported level flight.	75
7	Optimal design configuration for fins-supported level flight.	77
8	Performance of optimal vehicle in fins-supported level flight.	77
9	Optimal design configuration for fins and planing-supported level flight.	77
10	Performance of optimal vehicle in fins and planing-supported level flight.	78
11	Reduced optimal design configuration for fins-supported level turning flight.	92
12	Performance of reduced optimal vehicle in fins-supported level turning flight.	93
13	Optimal design configuration for fins-supported level turning flight.	94
14	Performance of optimal vehicle in fins-supported level turning flight.	94
15	Reduced optimal design configuration for a combined performance of fins-supported flight.	97
16	Performances of reduced optimal vehicle in fins-supported flight.	97
17	Optimal design configuration for a combined performance of fins-supported flight.	98
18	Controls and states of optimal configuration.	99
19	Performances of optimal vehicle in fins-supported flight.	99
20	Optimal design configuration for reduced design variable set: minimum time 40° heading-change maneuver.	119
21	Performance of optimal design configuration for reduced design variable set: minimum time 40° heading-change maneuver.	119
22	optimal design configuration for full design variable set: minimum time 40° heading-change maneuver.	120
23	Performance of optimal design configuration for full design variable set: minimum time 40° heading-change maneuver.	120
24	Optimal design configuration for full design variable set: minimum average thrust 40° heading-change maneuver.	123

25	Performance of optimal design configuration for full design variable set: minimum average thrust 40° heading-change maneuver.	123
26	Optimal design configuration for full design variable set: minimum average thrust 40° heading-change maneuver (without RSM).	124
27	Performance of optimal design configuration for full design variable set: minimum average thrust 40° heading-change maneuver (without RSM).	124
28	Comparison of solutions between standard and heuristic methods for $N = 3$	135
29	Comparison of solutions between standard and heuristic methods for $N = 4$	135
30	Reduced optimal design configuration with relaxed constraints.	138
31	Performance of reduced optimal vehicle with relaxed constraints.	138
32	Reduced optimal design configuration with active constraints.	138
33	Performance of reduced optimal vehicle with active constraints.	141
34	Optimal design configuration with relaxed constraints.	142
35	Performance of optimal vehicle with relaxed constraints.	142
36	Optimal design configuration with active constraints.	142
37	Performance of optimal vehicle with active constraints.	143
38	Performance of optimal vehicle with various constraint limitations	145

List of Figures

1	A schematics and prototype of RAMICS [1].	2
2	Four possible motions of a supercavitating vehicle.	4
3	Configuration of supercavitating vehicle and applied forces.	14
4	Body-fixed and inertial frames.	14
5	Non-dimensional cavity shape.	18
6	Comparison of cavity shapes and radial expansion rate for cavitation number $\sigma = 0.03$	20
7	Cavity shapes varying with the cavitation number $\sigma = 0.05, 0.03, 0.02, 0.01$	21
8	Cavity memory effects.	22
9	Cavitator reference frame.	24
10	Fin reference frame and angle of attack.	25
11	Fin hydrodynamic force and moment coefficients.	26
12	Configuration of planing vehicle and wetted cross section (all forces and moments are described for positive value).	30
13	A schematic of vehicle-cavity system over the evolving time.	33
14	A schematic of fin-cavity system over the evolving time.	35
15	Considered flight configurations.	38
16	Vehicle configuration.	38
17	Variation of controls in terms of pitch angle (cavitation number $\sigma = 0.0294$).	48
18	Variation of elevator angle of attack with respect to pitch angle (cavitation number $\sigma = 0.0294$).	49
19	Variation of controls in terms of forward velocity V (the planing depth is fixed $h_p _{\xi_1} = 0.01R_{veh}$ when the vehicle is planing).	50
20	Fin immersion depth versus speed of forward motion.	51
21	Trajectory of vehicle during fins-supported trimmed flight.	53
22	Time history of perturbed control angle.	53
23	Simulation results during perturbed fins-supported trimmed flight considering cavity with and without memory effects.	54
24	Forces without memory effects.	55
25	Forces with memory effects.	55

26	Trajectory in fins and planing-supported flight: vehicle configuration at 1.5, 1.8, 2.2, 2.5 sec.	56
27	Linear and angular velocities of the vehicle during fins and planing-supported trimmed flight.	57
28	Simulation results during perturbed fins and planing-supported trimmed flight.	58
29	Forces on fins and afterbody resulting from control perturbation.	58
30	Detail of forces on the afterbody during perturbed fins and planing-supported trimmed flight.	59
31	Variation of controls in terms of angular velocity of turning flight Ω	61
32	Variation of normalized Euler angles in terms of angular velocity of turning flight Ω	62
33	Variation of controls with and without memory effects.	63
34	Pitch and yaw versus roll angle with and without memory effects.	64
35	Schematic of variation of fin immersion depth versus roll with (solid lines) and without (dotted lines) memory effects.	64
36	Trajectory of vehicle during fins-supported level turning flight.	66
37	The comparison of trajectory of vehicle during fins-supported steady and perturbed level turning flight.	67
38	The hydrodynamic forces and moments applied to the fins and afterbody of the vehicle during perturbed fins-supported trimmed turning flight.	68
39	Effect of individual design variables on thrust and range for fins-supported level flight.	73
40	Variation of thrust force and range with respect to the vehicle design variables for fins-supported level flight.	74
41	Optimal configurations of supercavitating vehicles based on the Logvinovich's cavity model.	78
42	Optimal configurations of supercavitating vehicles based on the Munzer-Reichardt's cavity model.	78
43	Variation of turn rate and radius in terms of speed and load factor.	80
44	Difference between roll angles predicted from eq. (77) and eq. (78) at $V = 85$ m/s, $n = 5$).	81
45	V-n diagram for a rocket-propelled medium-range missile based on the AIM-7 Sparrow [2].	82
46	The variation of thrust with respect to the velocity and load factor for level turning flight of the nominal supercavitating vehicle (thrust normalized by nominal value 18.3176 kN).	82

47	Lift and drag coefficients for the cavitator of a supercavitating vehicle and for a conventional missile (a rocket-propelled medium-range missile based on the AIM-7 Sparrow).	83
48	The variation of bending moment on the fin's root with respect to the velocity and load factor (moment is normalized by the vehicle weight).	84
49	V-n diagram of the nominal supercavitating vehicle based on hydrodynamics but neglecting aerodynamics inside a cavity.	87
50	The variation of V-n diagram with respect to the cavitator diameter and fin span length when $\alpha_{N \max} = 30^\circ$ and $\gamma_{F_i \max} = 30^\circ$ (the contour lines denote constant turn rates).	88
51	Effect of individual design variables on thrust, range, and maximum turn rate for fins-supported level flight.	91
52	Variation of maximum turn rate in terms of selected design variables. . . .	92
53	Optimal configurations of supercavitating vehicles based on maximum turn rate during fins-supported level turning flight.	93
54	Configuration of the existing supercavitating vehicle Shkval [3].	95
55	Flowchart of optimization using ModelCenter TM	97
56	Optimal configurations of supercavitating vehicles based on a combined performance of maximum range and maximum turn rate during fins-supported flight.	98
57	Convergence test regarding to the resolution of discretization for the minimum flight time of heading-changing fins-supported flight.	106
58	Family of dives for increasing final depth.	108
59	Control time histories for the diving problem.	108
60	State time histories for the diving problem.	109
61	Family of turns for heading change varying between 10 deg and 180 deg. . .	110
62	Time histories of Euler angles during representative turns.	111
63	Comparison of minimum flight time estimated through direct solution and response surface approximation.	116
64	Variation of the minimum flight time versus vehicle radius and cone length. .	116
65	Variation of the minimum flight time versus vehicle radius and fin location. .	117
66	Effects of individual design variables on various performance indexes. . . .	118
67	Optimal configurations of supercavitating vehicles based on minimum flight time during fins-supported heading-changing maneuver.	120
68	The comparison of trajectory between the optimal and nominal vehicle for minimum flight time for the heading-changing fins-supported maneuver. . .	121

69	The optimal-to-nominal maneuvering time ratio with respect to heading angle.	121
70	The trajectory of the optimal vehicle according to heading angles.	122
71	Optimal configurations of supercavitating vehicles based on minimum average thrust during fins-supported heading-changing maneuver.	124
72	Variation of the minimum flight time in terms of V and d_c for a heading-change maneuver.	130
73	Feasible design regions for different choices of minimum allowed time for the maneuver.	131
74	Example illustrating a heuristic optimization strategy.	132
75	Design space and solutions: red circle point is the solution from the developed method, while the blue square indicates solutions found through the standard gradient method.	134
76	Evolution of design variables during optimization procedure for $N = 3$ with i.g. $x_1 = x_2 = x_3 = 1.5$	136
77	Evolution of objective, constraints, and design variables during optimization process with relaxed constraints.	139
78	Evolution of objective, constraints, and design variables during optimization with active constraints.	140
79	Evolution of constraints during optimization process.	144
80	Optimal configurations of supercavitating vehicles.	145

SUMMARY

Supercavitating vehicles exploit supercavitation as a means to reduce drag and achieve an extremely high underwater speed. Supercavitation is achieved when a body moves through water at sufficient speed, so that the fluid pressure drops to the water vapor pressure. In supercavitating flows, a low-density gaseous cavity entirely envelops the vehicle and the skin drag of the vehicle is almost negligible. Hence, the vehicle can move at extremely high speed in a two-phase medium.

The development of a controllable, maneuvering supercavitating vehicle has been confronted with various challenging problems such as the potential instability of the vehicle, the unsteady nature of cavity dynamics, and the complex and non-linear nature of the interaction between vehicle and cavity. Furthermore, one of the major issues towards the development of the vehicle is associated with the fact that major questions still need to be resolved regarding the basic configuration of the vehicle itself, including its control surfaces, the control system, and the cavity dynamics. In order to answer these fundamental questions, together with many similar ones, this dissertation develops an integrated design tool to optimize the vehicle configuration given specific operational requirements, while predicting the complex coupled behavior of the vehicle for each design configuration. Particularly, this research attempts to include various operating trim conditions as well as maneuvering flight directly in the vehicle configurational optimization. This integrated approach provides significant improvements in performance in the preliminary design phase.

In addition to an integrated approach, this thesis investigates trim conditions and dynamic characteristics of supercavitating vehicles. The influence of operating conditions, and cavity models and their memory effects on trim is analyzed and discussed. Unique characteristics are identified, e.g. the cavity memory effects introduce a favorable stabilizing effect by providing restoring fins and planing forces. Furthermore, this research investigates the flight envelope for defining performance in turns. For a supercavitating vehicle, the flight

envelope is significantly different from that of a conventional vehicle due to different hydrodynamic coefficients as well as unique operational conditions. The constraints limiting the flight envelope are also identified and described.

This study presents configurational optimization for various cases: maximum range, maximum turn rate and high maneuverability. The results show that trade-offs between various performance indexes are required due to their conflicting requirements. Constraints related to maneuver are shown to be very complex and can reduce the robustness of optimization. As a conceptual attempt, a simple optimization strategy is developed to increase computational efficiency and improve the capability to capture global optimum of this class of problems. This simple strategy shows better solution with better computational efficiency particularly for our problem.

Chapter I

INTRODUCTION

1.1 Introduction to Supercavitating Vehicles

The maximum speed of conventional underwater vehicles such as torpedoes and submarines is limited by the considerable skin friction drag on the hull. Speed of conventional underwater vehicles does not exceed 40 m/s as a maximum limit, and most practical systems are limited to less than half of this value [4]. While low speed is advantageous for acoustic and hydrodynamic efficiency, the achievement of high speed for the next-generation underwater torpedoes and projectiles is driven mainly by the requirements of modern marine warfare and, in civilian applications, by the development of conceptual designs of high-speed passenger submarines. The supercavitating Soviet torpedo Shkval, developed in 1977, has been reported to attain underwater speeds of the order of 100 m/s.

Supercavitation is achieved when a body moves through water at sufficient speed, so that the fluid pressure drops to the water vapor pressure. The process generally begins at the trailing edge of the body, where a phase change occurs and a low-density gaseous cavity forms. Flows exhibiting cavities entirely enveloping the moving body are called “supercavitating”. A supercavity may be maintained through vaporous cavitation sustained by sufficiently high speed or by ventilated cavitation through the artificial injection of gases. When supercavitating flows are developed, the moving body is in contact with liquid water only at its nose and partially over the afterbody. Hence, it experiences a substantially reduced drag and can achieve much higher speed than conventional vehicles. Several new and projected supercavitating underwater vehicles exploit supercavitation as a means to achieve extremely high submerged speeds and low drag. The size of existing or notional supercavitating high-speed bodies ranges from that of projectiles to heavyweight full-scale torpedoes [5]. Recently, the Office of Naval Research (ONR) has supported the development of small-scale supercavitating projectiles known as RAMICS in fig. 1 (Rapid Airborne Mine

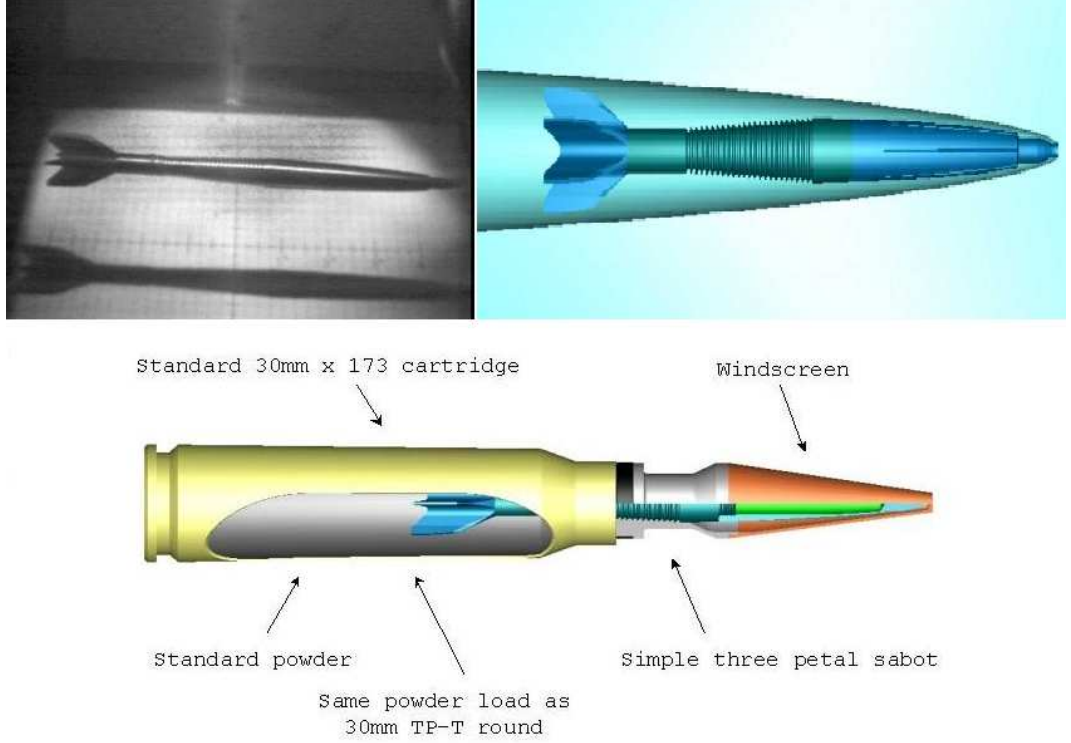


Figure 1: A schematics and prototype of RAMICS [1].

Clearance System) and AHSUM (Adaptable High Speed Undersea Munitions) [4, 6] as self-protection marine munitions. The former is a supercavitating projectile targeting near-surface mines, it is fired from a gun carried by a helicopter and travels in air as well as water. The latter targets incoming torpedoes, and is fired from a submerged gun carried by ships and submarines and travels under water at extremely high speed (~ 1500 m/s).

The challenges in using the supercavitating flow scheme for underwater vehicles are mostly associated with the strong and complex interactions between the cavity and the vehicle. The interactions are nonlinear and exhibit memory effects caused by the cavity shape being dependent upon the history of the vehicle motion and the trajectory. Other challenges in controlling and maneuvering the vehicles are related to the fact that the center of hydrodynamic pressure is placed forward of the mass center, thus violating the classic condition of hydrodynamic stability. Also, a supercavitating vehicle may not experience sufficient lift to sustain its level flight, and the drag force axially compressing the vehicle may be the cause of vibrations and possibly structural failure as a result of buckling [7, 8, 9].

1.1.1 Dynamics of supercavitating vehicles

The fundamental dynamic equations of motion for supercavitating vehicles are formulated as equations accounting for flight dynamics of aircraft except that the operating motion is in a complex two-phase medium, which features an inhomogeneous and unsteadiness-prone interface between vapor and water. In usual operating conditions, the control surfaces of a supercavitating vehicle are only partially immersed into water, which limits the control forces and may impose difficulties on maneuvering the vehicle. The hydrodynamic loads are affected by the interaction with the cavity which is highly nonlinear and depends on the vehicle's motion and trajectory. Also, due to the considerable role of the cavitator as a lifting control surface, the center of pressure is located in the front part of the vehicle, which is generally ahead of the center of gravity. Thus, uncontrolled motion of the vehicle tends to be unstable.

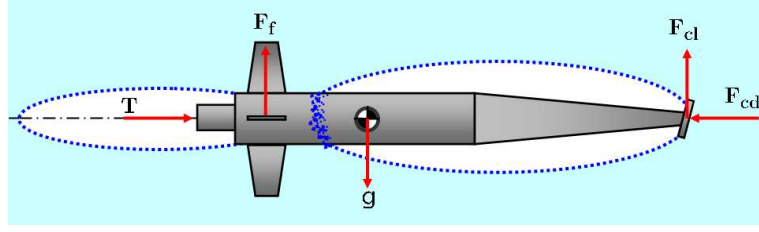
Savchenko [10] summarized four possible modes of vehicle motion arising according to vehicle velocity and supercavity development (see fig. 2):

1. *Motion inside a two-cavity flow* ($V \sim 70$ m/s):

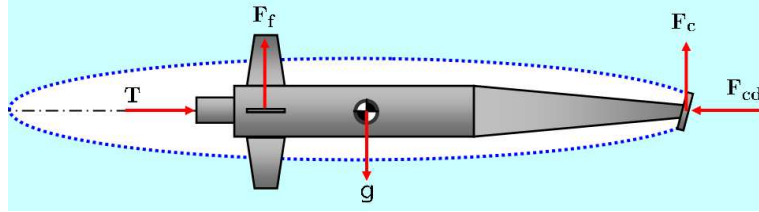
Due to low velocity, two partial cavities are developed at the leading edge and at the trailing edge of the vehicle. A fully-wetted afterbody can exert a buoyant force to counteract the vehicle weight in addition to the fins' lift. The extended contact of the afterbody with the fluid produces an additional drag force, which relocates the hydrodynamic drag center behind the center of mass and thus acts on the vehicle as a stabilizing moment, while however increasing the undesirable drag force.

2. *Motion inside a fully-developed supercavity* ($V \sim 50 - 200$ m/s):

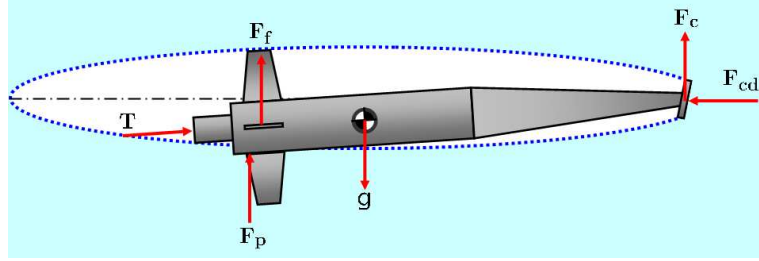
A vehicle has two possible attitudes at this stage mainly due to the absence of the buoyant force on the afterbody. First, a vehicle with control surfaces such as fins at the trailing edge can maintain straight level flight without contact with the cavity boundary. Secondly, for a vehicle without sufficient lift force at the afterbody such as finless projectiles, the small portion of the afterbody of the vehicle can be planing on the lower cavity surface. Planing occurs on the ellipsoidal cavity surface which may be inherently unsteady and its interface may be partially broken up. In this configuration, the capacity of simulating the



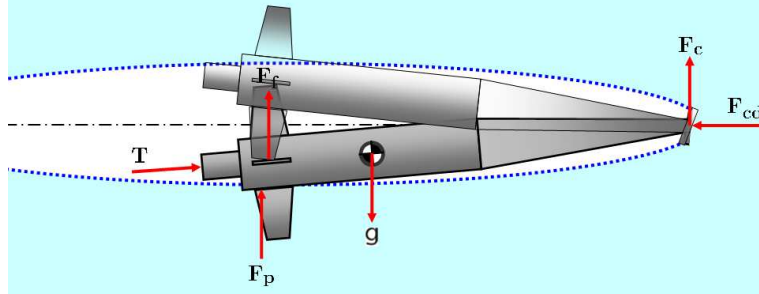
(a) Vehicle motion inside a two-cavity flow ($V \sim 70$ m/s)



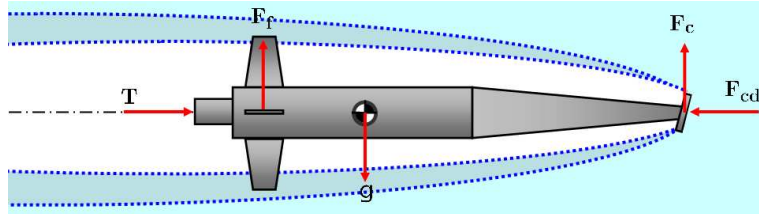
(b) Vehicle motion inside a fully-developed supercavity ($V \sim 50 - 200$ m/s)



(c) Vehicle motion with planing inside a fully-developed supercavity ($V \sim 50 - 200$ m/s)



(d) Vehicle motion with tail-slapping inside a fully-developed supercavity ($V \sim 300 - 900$ m/s)



(e) Vehicle motion with aerodynamic interaction inside a fully-developed supercavity ($V \sim 1000$ m/s and higher)

Figure 2: Four possible motions of a supercavitating vehicle.

vehicle dynamics highly depends on the degree of accuracy in predicting cavity shape and its dynamics.

3. *Motion with tail-slap inside a fully-developed supercavity* ($V \sim 300 - 900$ m/s):

At high speed, a supercavitating vehicle experiences periodic impacts against the cavity at the afterbody. These periodic impacts (tail-slaps) are induced by initial disturbances on the pitching angle and on velocity, and may produce steady or damped oscillatory motion with respect to the cavity. For example, tail-slap motion is observed for high-speed projectiles such as AHSUM, where the frequency of oscillation is of the order of 600 Hz for speeds of 600 m/s [4].

4. *Motion including aerodynamic interactions inside a fully-developed supercavity* ($V \geq 1000$ m/s):

At extremely high speed, a supercavitating vehicle experiences considerable aerodynamic forces inside the vaporous cavity, which requires near-wall aerodynamic analysis due to the relatively small intervening space between the vehicle hull and the cavity boundary. In addition, the vehicle motion may be affected by vapor splashes near the cavity boundary.

1.1.2 Control strategies for supercavitating vehicles

A great amount of research has been devoted to the development of control strategies and the analysis of stability of supercavitating vehicles. Previous investigations mostly considered simplified rigid body models which allow the study of the complex interactions between vehicle and surrounding cavity. For example in [11], a simplified single-degree-of-freedom (SDOF) model for longitudinal dynamics has been developed in order to investigate the vehicle stability with respect to memory effects and discontinuous nonlinearities associated with planing. In the model, memory effects are described as a time delay representing the interval required for a perturbation at the nose to affect the cavity shape on the afterbody. A magnification factor also accounts for the dive motion of the vehicle with respect to the cavity. The magnification factor depends on the magnitude ratio of pitching and diving modes. The SDOF model captures some of the dynamic characteristics of a full 6 DOF model and allows assessing the dynamic performance of the vehicle in a preliminary, yet

efficient way. Further, the model shows evidence of chaotic behavior in certain conditions. The pitch-dive longitudinal dynamics of supercavitating bodies has been investigated in [12, 4, 13, 14]. Rand et al. [4] for example, studied the characteristics of impacts between the vehicle's tail and cavity boundary (tail-slap) using a simplified model based on experimental observations. The formulation considers a 2 DOF model which describes the motion of the vehicle with respect to a horizontal cavity. The presented analytical results indicate that in the considered configuration, the tail-slap leads to a harmonic motion at frequencies which depend mostly upon the vehicle's velocity. Kulkarni and Pratap [13] also investigated dynamic behavior with tail-slaps, thus extending Rand's work by eliminating the restriction of straight flight. The authors evaluate impact loads by employing approximate added mass expressions based on the theory of Milwitzky [15]. The results agree with those of Rand et al., although it should be noted that their work still uses a very simplified model from the viewpoint of dynamics, as it ignores gravity force and the vehicle is assumed to be rotating about the nose. Dzielski and Kurdila [12] investigated control strategies for a model with vertical and pitch DOF, which are modes susceptible to instabilities. Linear and nonlinear control schemes have been developed to stabilize the vehicle's oscillatory motion with respect to the cavity. This oscillatory motion causes impulsive forces on the vehicle due to large restoring planing forces and their short duration and thus, causes challenging problems in designing appropriate actuation. Abed et al. [14] extended the previous pitch-dive dynamic model of [12] by focusing on the tail-slap behavior also occurring in the presence of partial cavities. They approximate a planing force as a piecewise linear function and apply switching linear feedback control to stabilize the vehicle. They also investigated bifurcations of solutions with regard to the cavitation parameters and found supercritical Hopf bifurcations of fixed points and period-doubling solutions.

The dynamic characteristics and control scheme based on a full 6 DOF model has been investigated in [16, 17, 6]. Goel [16] studied a 6 DOF model based on the strong assumption that the cavity is fixed and the vehicle moves symmetrically inside the cavity. Stability investigations on the linearized model at trim shows that the longitudinal and lateral motions are both unstable without a control scheme. The results also indicate that an

LQR (Linear Quadratic Regulator) controller achieves stable and good performance for the pitch and roll rate tracking commands. Kirschner et al. [17] studied the trajectory stability and dynamic performance of the vehicle under fins-supported and planing-supported level flight and during a steady bank-to-turn. The fins-supported case shows violent pitching oscillation as a result of initial perturbations. This behavior can be stabilized through an LQR-based feedforward/feedback control. In [6], Kirschner and co-authors presented a valuable overview of recent research and developments associated with supercavitating high-speed bodies. They describe tests on free-running models such as AHSUMs and discuss some results of supersonic underwater flight tests. Numerical and experimental results also show the highly nonlinear and three dimensional behavior of the cavity. A real cavity may hardly achieve axisymmetric shape in even well-controlled environments due to highly nonlinear turbulent flow. A cavity usually has helical flows revolving circumferentially, which are caused by a complex re-entrant flow. Also the cavity may undergo axial cyclic oscillations associated with the re-entrant flow, which induce spike-like cyclic variations in the drag coefficient. Finally, they conducted large-scale simulations using comprehensive and highly-accurate hydrodynamic model (UNCLE-M) based on Reynolds averaged Navier-Stokes. This code captures the considerable perturbations in cavity shape caused by a varying angle of attack of the cavitator. The results indicate that the cavity can strike the body during maneuvering and suggest that dynamic simulations based on simple hydrodynamic models may not represent the real behavior of the vehicle.

1.1.3 Structural analysis of supercavitating vehicles

Limited investigations have been performed on the structural behavior of supercavitating vehicles. Most of the work on simulation and control discussed above only considers rigid models and does not account for the influence of elastic modes of deformation on performance. Ruzzene and Soranna [18] investigated the dynamic response of a supercavitating vehicle during tail-slap using a beam elastic model combined with a 2 DOF rigid model. For rigid body motion, they used the same model presented in [4], which accounts for horizontal translation and rotation about the nose. The effect of periodically placed ring

stiffeners on the impact interaction between vehicle and cavity was investigated to demonstrate how corresponding vibrations can be significantly reduced through the addition of periodic ring stiffeners along the vehicle length. The dynamic behavior associated with the vehicle flexibility has also been investigated by Choi et al. [19], who applied a modal superposition technique to analyze the effect of flexibility on the stability of level flight and on the forces and structural strains associated with specific maneuvers. Their results indicate that the flexibility of the vehicle may be an additional source of instability. Drag and thrust can act as large compressive forces on the vehicle and can produce structural instabilities. Buckling of the vehicle has in fact been identified as one of the limiting factors for the speed of operation of supercavitating projectiles and should be investigated also for larger torpedoes [7]. The unsteady nature of supercavitation typically causes relative, small amplitude oscillations between cavity and vehicle. A full investigation of the stability of supercavitating vehicles hence requires to account for drag on the afterbody, and for its time dependency. Static and dynamic buckling stability has been investigated in [9, 8, 20, 21, 22]. Ruzzene [9, 8] used axisymmetric shells subjected to time-varying axial forces to capture cavity-vehicle interaction and cavity dynamics. Harmonic loads and step-wise periodic loads were considered as first approximations to highlight the possibility of parametric resonance conditions. The extension of the stability regions was estimated for varying velocity of the vehicle, frequency and amplitude of the force oscillations, and pulse duration. In addition, the effect of periodically placed circumferential stiffening rings on dynamic buckling stability was investigated. Alyanak et al. [20] conducted a detailed investigation on the structural characteristics of supercavitating vehicles using a high fidelity finite element model developed using the commercial package GENESIS. Structural failures during vehicle operation, stresses and natural frequencies as well as global buckling were investigated along with the effect of longitudinal and ring stiffeners. In addition, multi-disciplinary optimization was conducted to improve the stability of the vehicle. In [21], Alyanak and co-authors extended their previous investigation through optimization of the overall vehicle size (length and diameter), shape, and structural configuration. The optimal size was identified in terms of length and maximum diameter of the vehicle under the spatial

restrictions imposed by the cavity shape. Ahn and Ruzzene [22] extended studies of [9, 8] through configurational optimization of the vehicle which investigates optimally tapered and circumferentially stiffened designs to enhance the static and dynamic stability. They exploited nine-node general shell formulation in order to account for non-uniform thickness as well as time-varying non-axisymmetric axial forces.

1.1.4 Trajectory optimization of supercavitating vehicles

Although there are few applications of trajectory optimization to supercavitating vehicles, trajectory optimization in aerospace applications has been one of the important and successful branches of optimal control. The interest in optimal control has grown rapidly with the advent of digital computers along with needs in aerospace applications such as civil and military aviation and space exploration [23]. The goals of trajectory optimization in aerospace applications are of diverse kinds as [24]: minimum fuel flight or maximum range flight in civil airplanes, minimum flight time for reaching an assigned target state [25], safety-related trajectory to avoid crash [26, 27] and engine failure [28, 29], optimal pursuit-evasion flight [24], optimal interplanetary and orbital transfer [30, 31, 32], optimal launch and re-entry trajectories [33], optimal rocket trajectories [34], trajectory based on onboard guidance [35, 36], etc.

The optimal control problem, which is often called dynamic optimization, can be defined as finding optimal control functions for certain performance indexes subject to dynamic system equations and associated initial and boundary conditions. The performance index is a function of states and controls. Its maximization provides trade-offs between cost of terminal error, transient error, and control efforts [37]. A historical review of optimal control can be found in [38, 39] and comprehensive introductions are found in [40, 41, 42, 37].

In practice, optimal control problems have been solved by two categories of numerical methods: direct and indirect methods [23]. Indirect methods numerically solve the optimal control problem as a boundary value problem imposed by the first order necessary conditions of optimality according to the Pontryagin maximum principle. In contrast, direct

methods numerically solve the optimal control problem transcribing an original continuous problem into a parameter optimization one by means of discretization and suitable basis functions, in which system equations are transformed to defect constraints by suitable numerical integration schemes. In general, approximate formulations can be obtained by various numerical integration schemes such as second-order midpoint rule, second-order trapezoid rule, fourth-order Hermite-Simpson formulation, and high-order Gauss-Lobatto quadrature rules [31]. Comprehensive review and detail discussion on numerical methods for trajectory optimization are provided by Betts [23], Hull [43], and Ross [44]. Particularly, Hull [43] categorizes the various numerical methods according to the selected unknowns (four different methods in terms of control and states parameters).

Various maneuvers of supercavitating vehicles can be found through the solution of an optimal control problem, in which the time histories of vehicle controls and corresponding states are determined according to a certain performance index. Although vast research has been conducted for trajectory optimization in aerospace applications, few studies have been performed for supercavitating vehicles. Kamada et al. [45] investigated and developed a general framework for the maneuvers of a supercavitating vehicle through trajectory optimization. They employed the direct transcription method to solve for simple maneuvers such as dives and turns and demonstrated that this methodology is effective for a supercavitating vehicle and general. In their work, the integrated square of the magnitude of the controls is considered as a cost function, and a simple midpoint rule is used to discretize the states equations. Scorcelletti et al. [46] also investigated turn and target-tracking maneuvers of a supercavitating vehicle through the direct transcription method. One interesting result is that they obtained three dimensional trajectories for optimal turn maneuvers instead of in-plane turning trajectories as observed in [45, 47]. Although their work showed interesting results, the following limitations must be highlighted : 1) memory effects from cavity advection have not been considered, 2) the cavitation number is considered as constant regardless of underwater depth, which affects the vehicle maneuvers particularly during dive-climb and three-dimensional trajectories.

1.2 Objectives and Motivation

Supercavitating vehicles are high performance vehicles which operate at the boundaries of the flight envelope. The development of a controllable, maneuvering supercavitating vehicle has been confronted with various challenging problems such as the potential instability of the vehicle, the unsteady nature of cavity dynamics, the complex and non-linear nature of the interaction between vehicle and cavity, and the presence of hull vibrations induced by strong vehicle/cavity interaction. Furthermore, one of the major issues towards the development of the vehicle is associated with the fact that major questions still need to be resolved regarding the basic configuration of the vehicle itself, including its control surfaces, the control system, and the cavity dynamics. The answer to these fundamental questions, together with many similar ones, requires integrated design tools capable of optimizing the vehicle configuration subjected to realistic constraints. The objective of the thesis is the development of a simulation-based design tool that answers the above needs and which is capable of vehicle configuration optimization according to requirements dictated by operational configurations. The posteriori analysis of the structural performance of the optimized vehicles can assess of the feasibility of the considered configurations from a structural perspective. This approach potentially provides a methodology to achieve performance improvements that would not be otherwise obtainable.

1.3 Outline

Following this introductory chapter, chapter 2 presents the equations governing the dynamic behavior of a supercavitating vehicle and introduces simplified models for the description of cavity shapes and dynamics, and of the interaction forces between vehicle and cavity. Chapter 3 presents investigations on trim operating conditions for level flight and level turning flight. Also, a series of examples of flight simulations in response to assigned control actions is provided. Two trimmed configurations are in particular considered with two cavity models : fins-supported and fins and planing-supported. Chapter 4 presents the configurational optimization of a supercavitating vehicle operating at trim where maximum range and maximum turn rate are considered as primary performance indexes. The design

conflicts between optimal vehicles of two performances are identified. The chapter also provides a description of the flight envelope essential for evaluating turning performance index. Configurational optimization studies follow in Chapter 5 where a maneuverability is the considered performance index. Various vehicle maneuvers are defined through the trajectory optimization tool developed at the Politecnico di Milano. The optimization procedure developed in previous chapters is extended to account for trim performances and maneuverability in Chapter 6. Finally, chapter 7 presents concluding remarks and recommendations for potential extension of this research.

Chapter II

FLIGHT MECHANICS MODEL

2.1 *Overview*

This chapter presents the equations governing the dynamic behavior of a supercavitating vehicle and introduces simplified models for the description of cavity shapes and dynamics, and of the interactions forces between vehicle and cavity. The model is used as a flight simulator for supercavitating vehicles and as an engine for the optimization of the vehicle's configurational design.

A 6 DOF rigid body model describes the dynamic behavior of the vehicle. A schematic of the vehicle configuration and of the applied forces is shown in fig. 3. The body is acted upon by a system of forces corresponding to the interaction of the vehicle control surfaces with the cavity boundaries. The control surfaces include the fins at the back of the vehicle and the cavitator, whose primary function is the generation of the supercavity. The control surfaces provide lift, and allow for roll, pitch and yaw control. Finally, the vehicle motion is sustained by a propulsion force directed along the vehicle's axis.

2.2 *Equations of Motion*

The equations of motion are conveniently formulated in a body-fixed reference frame $\mathcal{F}_{P,\mathcal{B}}$, with origin in P and triad $\mathcal{B} = (\mathbf{b}_1, \mathbf{b}_2, \mathbf{b}_3)$. A reference inertial frame $\mathcal{F}_{O,\mathcal{I}}$ is centered at point O and has a triad of unit vectors $\mathcal{I} = (\mathbf{i}_1, \mathbf{i}_2, \mathbf{i}_3)$, as shown in fig. 4.

The equations of balance of linear and angular momentum (Euler's equations) in the body-attached frame can be written as

$$\begin{aligned} \dot{\mathbf{l}}^{\mathcal{B}} + \boldsymbol{\omega}^{\mathcal{B}} \times \mathbf{l}^{\mathcal{B}} &= \mathbf{s}^{\mathcal{B}}, \\ \dot{\mathbf{h}}_P^{\mathcal{B}} + \mathbf{v}_P^{\mathcal{B}} \times \mathbf{l}^{\mathcal{B}} + \boldsymbol{\omega}^{\mathcal{B}} \times \mathbf{h}_P^{\mathcal{B}} &= \mathbf{m}_P^{\mathcal{B}}, \end{aligned} \tag{1}$$

where the linear momentum is $\mathbf{l} = m\mathbf{v}_P + \mathbf{S}_P^T \boldsymbol{\omega}$ and the angular momentum is given by $\mathbf{h}_P = \mathbf{S}_P \mathbf{v}_P + \mathbf{J}_P \boldsymbol{\omega}$. Letting ρ_V be the vehicle density, $m = \int_V \rho_V dV$ is the mass of the

vehicle, $\mathbf{S}_P = \int_V \rho_V \mathbf{r}_\times dV$ is the first moment of inertia, $\mathbf{J}_P = -\int_V \rho_V \mathbf{r}_\times \mathbf{r}_\times dV$ is the inertia dyadic, \mathbf{v}_P and $\boldsymbol{\omega}$ denote the linear velocity of point P and the angular velocity of the body, respectively, while \mathbf{s} and \mathbf{m}_P are the resultants of the applied forces and moments, respectively. Here and in the following, the notation $(\cdot)^{\mathcal{A}}$ denotes components in the generic \mathcal{A} triad. If \mathbf{R} is the rotation tensor that brings triad \mathcal{I} into triad \mathcal{B} , then the components of a generic vector \mathbf{a} in the two triads are related as $\mathbf{a}^{\mathcal{I}} = \mathbf{R}_{\mathcal{I} \rightarrow \mathcal{B}}^{\mathcal{I}} \mathbf{a}^{\mathcal{B}}$. Furthermore, \mathbf{a}_\times is the skew-symmetric tensor associated with \mathbf{a} . Finally, the symbol $\dot{(\cdot)} = d \cdot / dt$ indicates differentiation with respect to time.

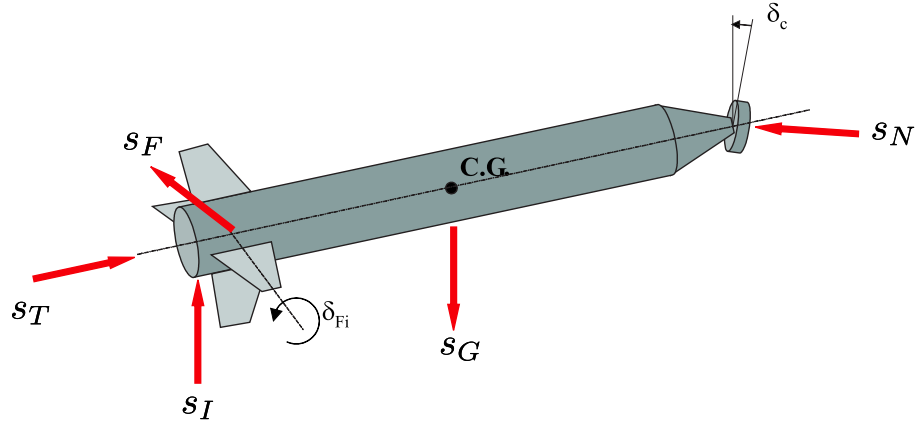


Figure 3: Configuration of supercavitating vehicle and applied forces.

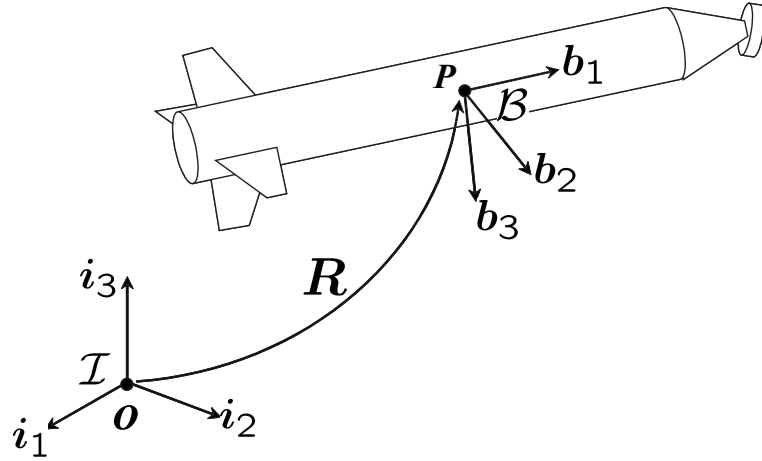


Figure 4: Body-fixed and inertial frames.

Equations (1) can be conveniently rewritten in the following compact form:

$$\mathbf{M}^{\mathcal{B}} \dot{\mathbf{w}}^{\mathcal{B}} + \mathbf{w}^{\mathcal{B}} \times \mathbf{M}^{\mathcal{B}} \mathbf{w}^{\mathcal{B}} = \mathbf{f}^{\mathcal{B}}, \quad (2)$$

where the generalized inertia tensor is defined as

$$\mathbf{M} = \begin{bmatrix} m\mathbf{I} & \mathbf{S}_P^T \\ \mathbf{S}_P & \mathbf{J}_P \end{bmatrix}, \quad (3)$$

and the generalized velocity \mathbf{w} and generalized force \mathbf{f} are respectively given by:

$$\mathbf{w} = (\mathbf{v}_P^T, \boldsymbol{\omega}^T)^T, \quad \mathbf{f} = (\mathbf{s}^T, \mathbf{m}_P^T)^T. \quad (4)$$

In equation (2), $(\cdot) \times$ is the South-West cross product operator [48]:

$$\mathbf{w} \times = \begin{bmatrix} \boldsymbol{\omega}_{\times} & \mathbf{0} \\ \mathbf{v}_{P \times} & \boldsymbol{\omega}_{\times} \end{bmatrix}. \quad (5)$$

The position and orientation of the vehicle with respect to the inertial frame can be expressed through the position vector $\mathbf{u}_P = (P - O)$ and a set of rotation parameters, more specifically Euler parameters arranged in quaternion form for this work. The vehicle kinematic equations can be written as

$$\dot{\mathbf{d}} = \begin{bmatrix} \mathbf{R}^{\mathcal{I}} & \mathbf{0} \\ \mathbf{0} & \mathbf{E} \end{bmatrix} \mathbf{w}^{\mathcal{B}}, \quad (6)$$

where \mathbf{d} is the vector of the generalized coordinates defined as

$$\mathbf{d} = (\mathbf{u}_P^T, \mathbf{q}_4^T)^T, \quad (7)$$

with $\mathbf{q}_4 = (q_0, \mathbf{q}^T)^T$ denoting the quaternion. Again with reference to equation (6), \mathbf{E} relates the time rates of the rotation parameters with the body-frame components of the angular velocity and is defined as:

$$\mathbf{E} = \frac{1}{2} \begin{bmatrix} -\mathbf{q}^T \\ q_0 \mathbf{I} + \mathbf{q}_{\times} \end{bmatrix}. \quad (8)$$

Equation (6) implicitly enforces the derivative of the unit quaternion condition, which can be expressed as:

$$\dot{\mathbf{q}}_4 \cdot \mathbf{q}_4 = 0. \quad (9)$$

The forces \mathbf{s} acting on the vehicle can be written as

$$\mathbf{s} = \mathbf{s}_T + \mathbf{s}_N + \sum_{i=1}^{n_F} \mathbf{s}_{F_i} + \mathbf{s}_I + \mathbf{s}_G, \quad (10)$$

where $\mathbf{s}_T = \delta_T \mathbf{b}_1$ is the propulsive thrust, \mathbf{s}_N is the hydrodynamic force at the vehicle nose generated by the cavitator, \mathbf{s}_{F_i} are the hydrodynamic forces generated by the n_F fins, \mathbf{s}_I are the contact forces due to the interaction of the vehicle with the cavity, and finally $\mathbf{s}_G = -mg\mathbf{i}_3$ is the gravitational force. Similarly, the moments \mathbf{m}_P can be written as

$$\begin{aligned} \mathbf{m}_P = & \mathbf{r}_{PT} \times \mathbf{s}_T + \mathbf{r}_{PN} \times \mathbf{s}_N + \sum_{i=1}^{n_F} \mathbf{r}_{PF_i} \times \mathbf{s}_{F_i} \\ & + \mathbf{r}_{PI} \times \mathbf{s}_I + \mathbf{r}_{PG} \times \mathbf{s}_G + \sum_{i=1}^{n_F} \mathbf{m}_{F_i} + \mathbf{m}_I, \end{aligned} \quad (11)$$

where \mathbf{r}_{AB} indicates a distance vector from point A to point B , T is the point of application of the thrust, N is the cavitator location, F_i is the aerodynamic center of the i th fin, I is the tail-cavity contact point and G is the center of gravity.

2.3 Cavity Models

The behavior of the cavity affects the forces at the nose of the vehicle, the immersion of the fins in the fluid, and the contact forces between vehicle and cavity boundary. Particularly, the planing and fins forces strongly depend on the dynamic behavior of the vehicle and on the hydrodynamic characteristics of the cavity. The vehicle velocity affects the cavity shape and size, which in turn modify the extension of the immersed area of the vehicle and the magnitude of the resulting planing and fins forces. As a result, the vehicle-cavity system is highly coupled.

In this work, simple supercavity models suitable for time domain dynamic simulation are employed. It should be noted that supercavitation may in general be estimated more accurately by approaches based on slender-body theory, boundary element methods, and sophisticated computational methods relying on the solution of Navier-Stokes equations along with models for the cavity re-entrant jet. In particular, cavity shapes obtained from the approximate models presented below predict an unrealistically smooth closing of the cavity at the rear portion, whereas in general, gas leakage from the cavity occurs and gases

are turbulently mixed with liquid supplied by the re-entrant jet. Cavity perturbations due to its radial expansion and floating-up also affect the process of gas leakage along with the vehicle's shape and vibrations at the closing region [49]. These phenomena are neglected in the following simplified approximate models, which however are considered to be efficient and accurate enough to reproduce the overall dynamic behavior of a supercavitating vehicle.

2.3.1 Munzer-Reichardt's model

Munzer-Reichardt's is an early model based on low-order potential flow. It predicts an axisymmetric cavity shape described by the following expression [50]:

$$r_c(\xi) = \frac{d_{max}}{2} (4\xi(1-\xi))^{1/2.4}, \quad \xi = x/l_{max} \quad (12)$$

where $r_c(\xi)$, d_{max} , and l_{max} are the cavity radius at location ξ along the centerline of cavity, the maximum diameter and length of the cavity. The origin of the longitudinal coordinate ξ is located at the front nose. The cavity length l_{max} and maximum diameter d_{max} are given by [51]:

$$\begin{aligned} d_{max} &= d_c \sqrt{\frac{C_d(\sigma, 0)}{\sigma}} \\ l_{max} &= d_c \sqrt{\frac{C_d(\sigma, 0)}{\sigma^2} \ln \left(\frac{1}{\sigma} \right)} \end{aligned} \quad (13)$$

where d_c , C_d and σ are the cavitator diameter, the cavitator drag coefficient and the cavitation number. The hydrodynamic drag, lift, and moment coefficients for a disk-type cavitator with angle of attack, α_c are given by [52]:

$$\begin{aligned} C_d(\sigma, \alpha_c) &= C_{do}(1 + \sigma) \cos^2 \alpha_c \\ C_L(\sigma, \alpha_c) &= C_{do}(1 + \sigma) \cos \alpha_c \sin \alpha_c \\ C_m(\sigma, \alpha_c) &\simeq 0 \end{aligned} \quad (14)$$

The cavitation number σ is defined as:

$$\sigma = \frac{(p_\infty - p_c)}{\frac{1}{2}\rho_w V_N^2}, \quad p_\infty = \rho_w g h + p_{atm} \quad (15)$$

where p_∞ and p_c are respectively the ambient fluid pressure and cavity vapor pressure. Also, V_N , ρ_w , g , h , and p_{atm} are respectively the speed of the vehicle's nose, the fluid (water)

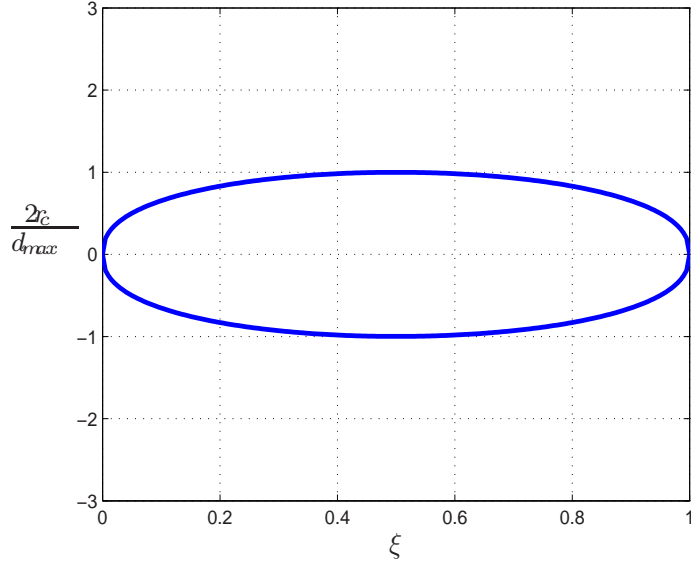


Figure 5: Non-dimensional cavity shape.

density, gravity acceleration, depth under water surface, and atmospheric pressure on the water surface. The drag coefficient at zero angle of attack and cavitation number, C_{do} , is chosen to be 0.815 according to empirical formulation presented in [53]. Munzer-Reichardt's cavity model neglects gravity distortion effects, and assumes a steady cavity with internal constant pressure p_c . An example of cavity shape predicted by Munzer-Reichardt's model is shown in fig. 5.

2.3.2 Logvinovich's model

Another formulation describing the shape of the cavity is based on Logvinovich's model [54]. The model assumes that each cavity section expands independently of adjacent sections without viscous effects (Logvinovich independence principle). Hence, the expansion depends on fluid inertia and on the pressure difference between the cavity and the ambient liquid. The cavity section obtains kinetic energy when it expands radially during separation at the nose. This initial kinetic energy equals the work done by the pressure difference during the cavity section expansion from initial radius to maximum radius. After expanding, the cavity section contracts and obtains an amount of kinetic energy equal to the work done by the pressure difference. Vasin derived the cavity radius based on the Logvinovich principle

and energy conservation [55]. A review of [55, 54] are presented in what follows.

The cavity radius r_c and radial expansion rate \dot{r}_c are defined as:

$$\begin{aligned} r_c &= r_{max} \sqrt{1 - \left(1 - \frac{r_o^2}{r_{max}^2}\right) \left(1 - \frac{t}{t_{max}}\right)^2} \\ \dot{r}_c &= \frac{r_{max}^2}{r_c} \frac{1}{t_{max}} \left(1 - \frac{r_o^2}{r_{max}^2}\right) \left(1 - \frac{t}{t_{max}}\right) \end{aligned} \quad (16)$$

where r_o , r_{max} , and t_{max} are the initial cavity radius, the maximum cavity radius defined in eq. (13), and the time required for the cavity to achieve its maximum radius. It should be noted that assuming the initial radius $r_o = 0$ and eliminating time leads to a formula equivalent to Munzer-Reichardt's model (eq. (12)) with a different exponent (2 instead of 2.4). From the physical viewpoint, the initial cavity radius r_o in eq. (16) can be considered as the cavitator radius $d_c/2$. In general, the prediction of cavity shape has been conducted through modified forms of eq. (16) based on the experimental data [54]:

$$\begin{aligned} r_c &= r_{max} \sqrt{1 - \left(1 - \frac{r_o^2}{r_{max}^2}\right) \left|1 - \frac{t}{t_{max}}\right|^{\frac{2}{\kappa}}} \\ \dot{r}_c &= \frac{r_{max}^2}{r_c} \frac{1}{\kappa t_{max}} \left(1 - \frac{r_o^2}{r_{max}^2}\right) \left(1 - \frac{t}{t_{max}}\right) \left|1 - \frac{t}{t_{max}}\right|^{\frac{2(1-\kappa)}{\kappa}} \end{aligned} \quad (17)$$

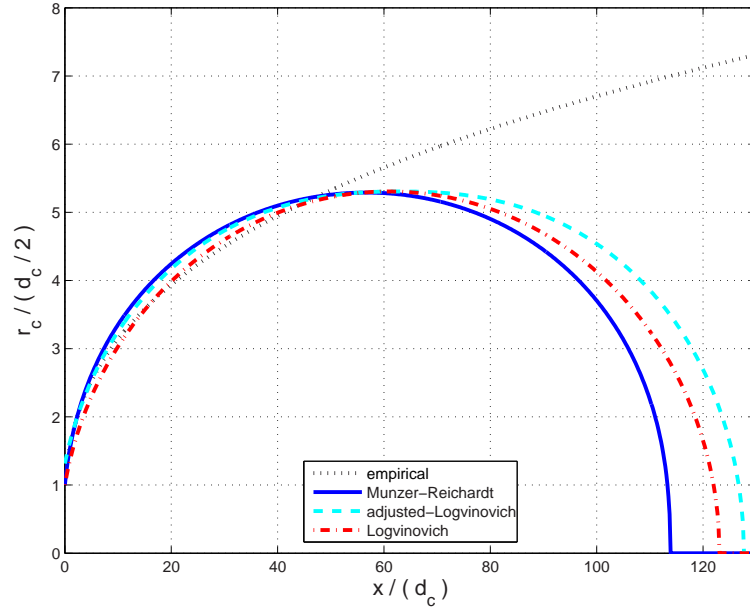
where the correction factor is selected as $\kappa = 0.85$ based on $C_{do} = 0.82$. The maximum length of the cavity l_{max} and the time t_{max} are given by [54]:

$$\begin{aligned} l_{max} &= d_c \left(\frac{1.92}{\sigma} - 3 \right) \\ t_{max} &= \frac{l_{max}}{2V} \end{aligned} \quad (18)$$

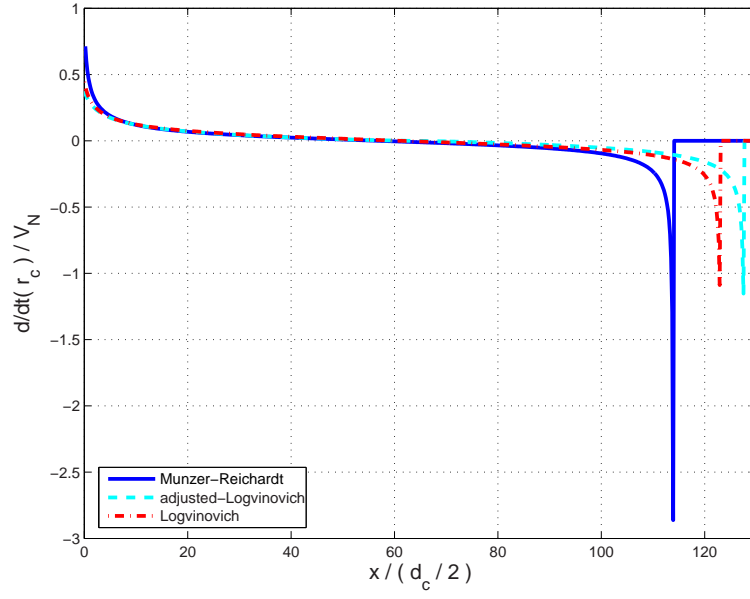
The initial cavity radius is selected as $r_o = (7)^{\frac{1}{3}} \frac{d_c}{2} = 1.92 \frac{d_c}{2}$, which matches the cavity radius r_o with one predicted by following empirical formula at $x = d_c$ [54]:

$$r_c = \frac{d_c}{2} \left(1 + \frac{3x}{d_c/2} \right)^{\frac{1}{3}} \quad (19)$$

The cavity shapes predicted by the various models are compared in fig. 6, where ‘adjusted Logvinovich’ and ‘empirical’ refer to eqs. (17) and (19), respectively. It should be noted that radial expansion rate of the cavity \dot{r}_c can considerably affect the apparent angle of attack when the afterbody is planing [12]. Indeed, the cavity surface at the contact region



(a) Radius



(b) Radial expansion rate

Figure 6: Comparison of cavity shapes and radial expansion rate for cavitation number $\sigma = 0.03$.

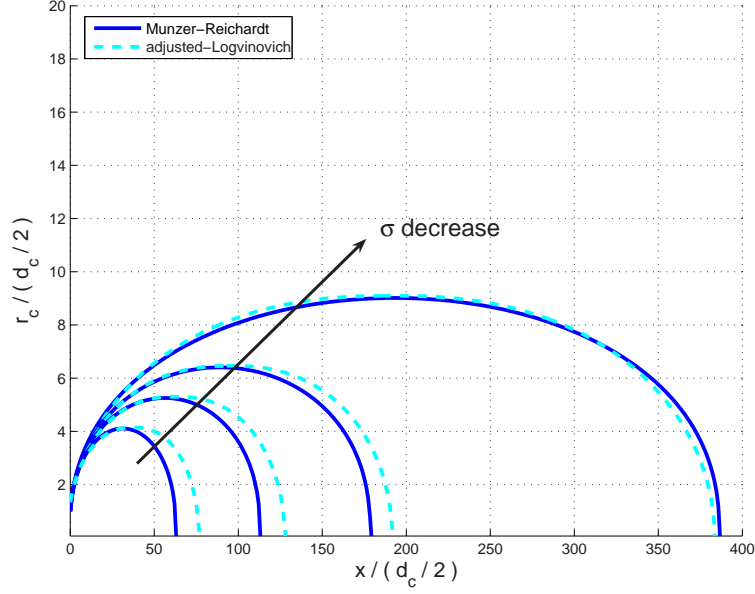


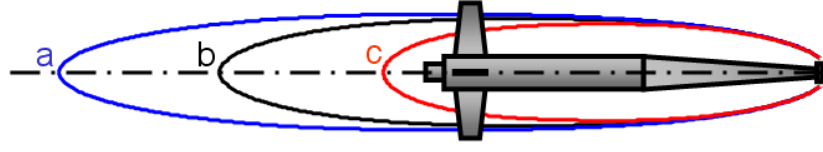
Figure 7: Cavity shapes varying with the cavitation number $\sigma = 0.05, 0.03, 0.02, 0.01$.

forms a wetted wedge having an additional angle of attack due to the radial contraction rate.

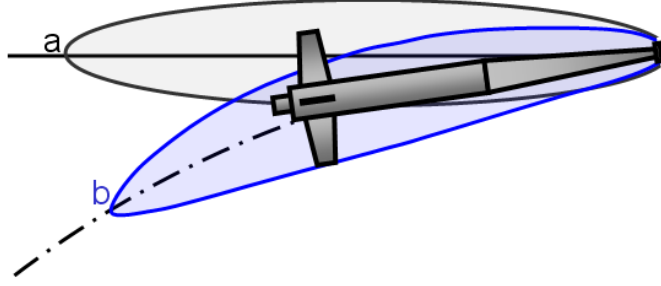
Fig. 7 shows how the cavity shape varies with the cavitation number particularly for two cavity models, Logvinovich's and Munzer-Reichardt's ones. The cavity size increases as the cavitation number decreases for both models. However, at high cavitation number the former predicts a larger cavity, while at low cavitation number the situation is reversed. This dependency of the cavity on the cavitation number significantly affects the trim conditions and dynamic properties of the vehicle according to the vehicle operating conditions (e.g. speed and altitude).

2.3.3 Cavity memory effects

By virtue of Logvinovich's independence principle, the cavity centerline always traces the trajectory of the cavitator and each cavity section radius is determined by the state of cavitator when it is generated. As a result, cavity distortions caused by a disturbance of the cavitator propagates towards the afterbody according to the vehicle speed with a certain time lag which affects the vehicle dynamic behavior by changing hydrodynamic forces and moment on the control surfaces. However, vehicle dynamic perturbations triggered by



(a) Steady, accelerating and decelerating level flight



(b) Steady turning flight

Figure 8: Cavity memory effects.

the cavitator generate corresponding transient cavity distortions. In general the time lag and related effects here denoted as memory effects, depend on the history of the vehicle motion, and vehicle dimensions and geometry. Normally, the cavitator generates a time-varying cavity radius and curved cavity centerline which causes the center of the cavity cross section at the fin's location and at the afterbody to deviate from the center of the vehicle cross section. This time-varying deviation and cavity radius at the afterbody produces asymmetric fin immersion and/or changes in the vehicle operating configurations.

Figure 8 shows how memory effects affect cavity shape according to flight conditions. The influence of memory effects on the cavity radius and length is shown in fig. 8 (a), where the cavity b is generated during constant-velocity level flight, while the cavities a and c are respectively generated during decelerating and accelerating level flight. The influence of memory effects on the cavity centerline is also shown in fig. 8 (b), where the vehicle performs a steady (constant speed) turning flight. The cavities a and b are respectively evaluated without and with memory effects. Particularly, the cavity a is evaluated by the instantaneous value of the cavitation number, which is determined on the basis of the

current state of the vehicle.

2.4 Cavitator Force Model

The hydrodynamic forces acting on a circular cavitator can be conveniently expressed in terms of a reference frame $\mathcal{F}_{N,\mathcal{N}}$ located at the cavitator center N and with triad of unit vectors $\mathcal{N} = (\mathbf{n}_1, \mathbf{n}_2, \mathbf{n}_3)$, as shown in fig. 9. Unit vector \mathbf{n}_1 is perpendicular to the disk surface. Its orientation with respect to the vehicle axis \mathbf{b}_1 is defined by the control angle δ_N , so that the components of \mathbf{n}_1 in the body-fixed triad \mathcal{B} , labeled $\mathbf{n}_1^{\mathcal{B}}$, are

$$\mathbf{n}_1^{\mathcal{B}} = (\cos \delta_N, 0, -\sin \delta_N)^T. \quad (20)$$

Unit vector \mathbf{n}_2 is orthogonal to the plane formed by the pair of vectors \mathbf{v}_N and \mathbf{n}_1 , i.e.

$$\mathbf{n}_2 = \frac{\mathbf{v}_N \times \mathbf{n}_1}{\|\mathbf{v}_N \times \mathbf{n}_1\|}, \quad (21)$$

where $\mathbf{v}_N = \mathbf{v}_P + \boldsymbol{\omega} \times \mathbf{r}_{PN}$ is the cavitator velocity, \mathbf{r}_{PN} being the distance vector between the reference point P on the vehicle and the cavitator center N . Finally, unit vector \mathbf{n}_3 completes a right handed triad: $\mathbf{n}_3 = \mathbf{n}_1 \times \mathbf{n}_2$. The components of the three unit vectors \mathbf{n}_1 , \mathbf{n}_2 and \mathbf{n}_3 measured in the body-attached triad \mathcal{B} readily give the components in \mathcal{B} of the rotation tensor that rotates the \mathcal{B} triad into the \mathcal{N} triad:

$$\mathbf{R}_{\mathcal{B} \rightarrow \mathcal{N}}^{\mathcal{B}} = [\mathbf{n}_1^{\mathcal{B}} | \mathbf{n}_2^{\mathcal{B}} | \mathbf{n}_3^{\mathcal{B}}]. \quad (22)$$

Hence, if $\mathbf{v}_N^{\mathcal{B}}$ denotes the components of the cavitator velocity in the \mathcal{B} triad, the components of the same vector in the cavitator triad \mathcal{N} are

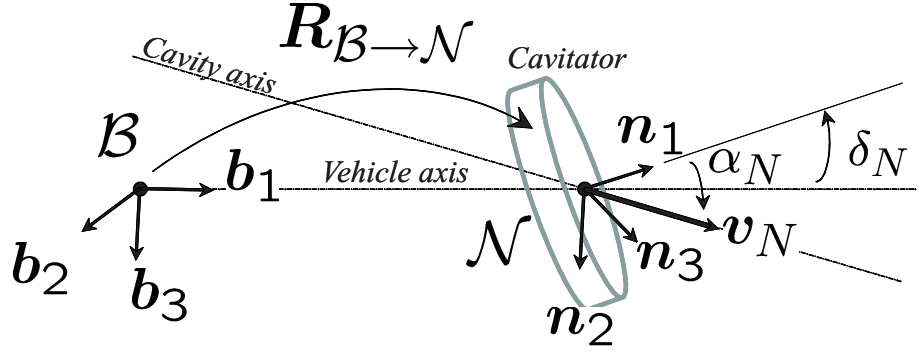
$$\mathbf{v}_N^{\mathcal{N}} = \mathbf{R}_{\mathcal{B} \rightarrow \mathcal{N}}^{\mathcal{B}T} \mathbf{v}_N^{\mathcal{B}} = (u_N^{\mathcal{N}}, 0, w_N^{\mathcal{N}})^T. \quad (23)$$

The cavitator angle of attack α_N is measured in the \mathbf{v}_N , \mathbf{n}_1 plane (see fig. 9), and it is computed as

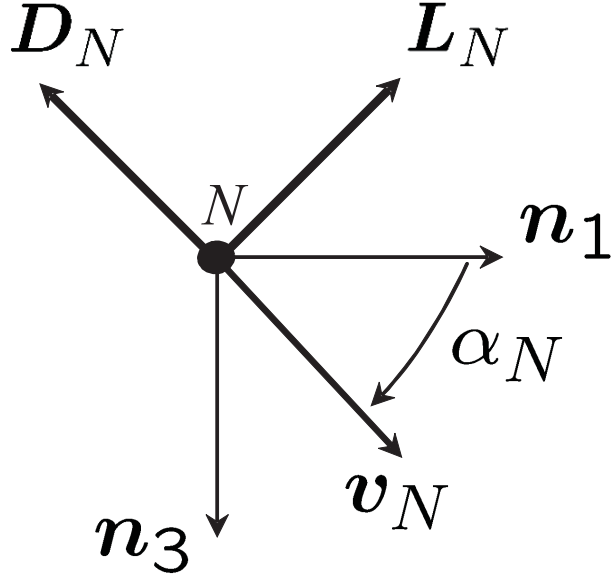
$$\tan \alpha_N = \frac{w_N^{\mathcal{N}}}{u_N^{\mathcal{N}}}. \quad (24)$$

In the \mathbf{v}_N , \mathbf{n}_1 plane, the hydrodynamic force acting on the cavitator can be decomposed into lift and drag components, which can be computed as [52]

$$\begin{aligned} L_N &= \frac{1}{2} \rho_w v_N^2 A_N C_d(\sigma, 0) \sin \alpha_N \cos \alpha_N, \\ D_N &= \frac{1}{2} \rho_w v_N^2 A_N C_d(\sigma, 0) \cos^2 \alpha_N, \end{aligned} \quad (25)$$



(a) Detail of cavitator



(b) Lift and drag components in the $\mathbf{v}_N, \mathbf{n}_1$ plane

Figure 9: Cavitator reference frame.

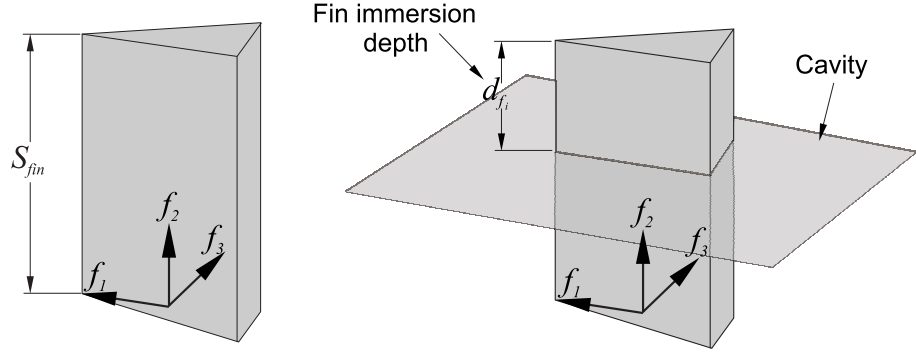
where A_N is the cavitator area. The hydrodynamic force can hence be expressed in the \mathcal{N} triad as

$$\mathbf{s}_N^{\mathcal{N}} = (-L_N \sin \alpha_N - D_N \cos \alpha_N, 0, L_N \cos \alpha_N - D_N \sin \alpha_N)^T, \quad (26)$$

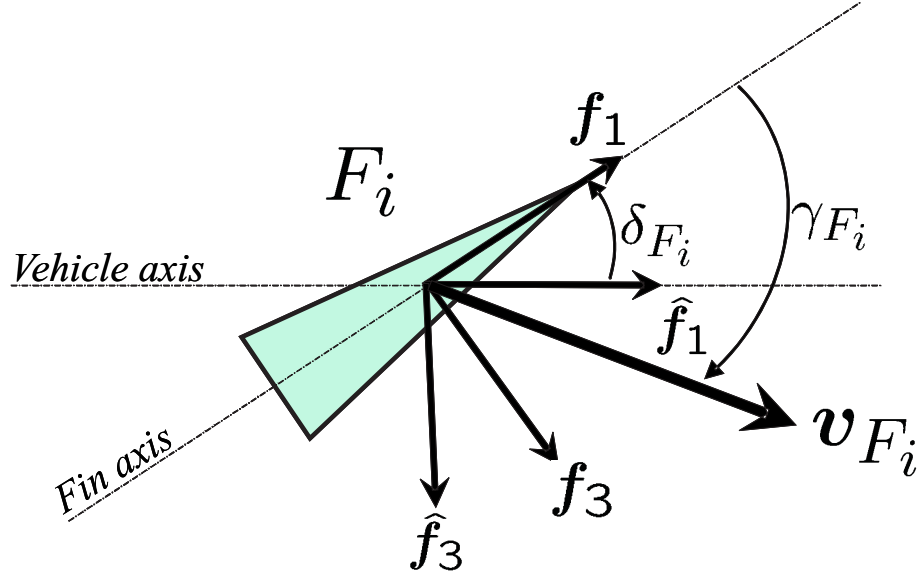
and transformed to the \mathcal{B} triad as $\mathbf{s}_N^{\mathcal{B}} = \mathbf{R}_{\mathcal{B} \rightarrow \mathcal{N}}^{\mathcal{B}} \mathbf{s}_N^{\mathcal{N}}$. This formulation for the cavitator force neglects the effects of hydrodynamic added mass and damping which are discussed in [56].

2.5 Fin Force Model

The fins are controlled to provide lift in the after-body section and to maneuver the vehicle. We consider the 4-fin configuration shown in fig. 3. Each fin interacts with the surrounding



(a) Detail of fin



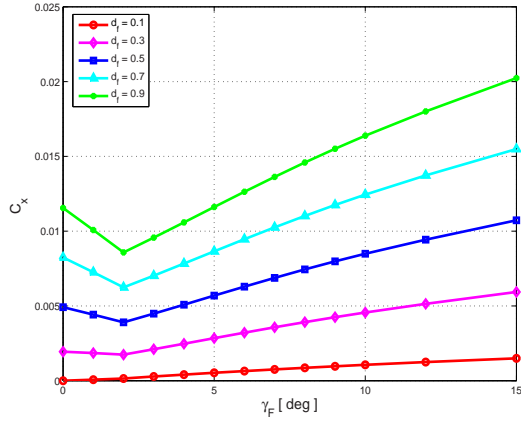
(b) Fin-fixed frame and fin velocity

Figure 10: Fin reference frame and angle of attack.

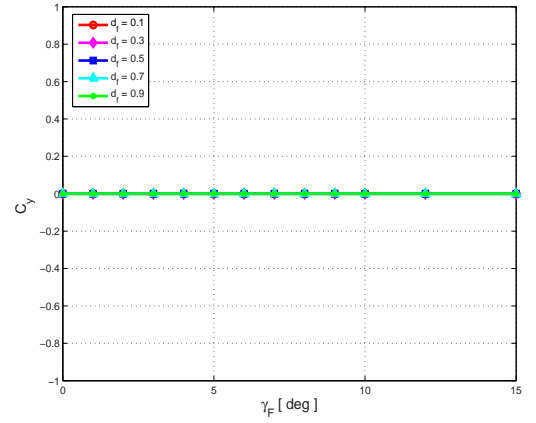
fluid with forces that depend on the immersion depth in the fluid, the velocity at the fin location with respect to the fluid, the fin geometry and the angle of attack.

For convenience, the forces are first expressed in a reference frame $\mathcal{F}_{F_i, \mathcal{F}_i}$, with origin F_i and triad $\mathcal{F}_i = (\mathbf{f}_1, \mathbf{f}_2, \mathbf{f}_3)$ fixed to the i th fin, as shown in fig. 10. Triad \mathcal{F}_i is obtained by a rotation that first brings \mathcal{B} into the undeflected fin configuration $\hat{\mathcal{F}}_i = (\hat{\mathbf{f}}_1, \hat{\mathbf{f}}_2, \hat{\mathbf{f}}_3)$, $\hat{\mathbf{f}}_k = \hat{\mathbf{R}}_i \mathbf{b}_k$, $k = 1, 2, 3$, followed by a rotation $\delta_{F_i} \hat{\mathbf{f}}_2$, with δ_{F_i} denoting the deflection of the i th fin, $\mathbf{f}_k = \mathbf{R}(\delta_{F_i} \hat{\mathbf{f}}_2) \hat{\mathbf{f}}_k$, $k = 1, 2, 3$. The total rotation from \mathcal{B} to \mathcal{F}_i is hence $\mathbf{f}_k = \mathbf{R}_{\mathcal{B} \rightarrow \mathcal{F}_i} \mathbf{b}_k$, $\mathbf{R}_{\mathcal{B} \rightarrow \mathcal{F}_i} = \mathbf{R}(\delta_{F_i} \hat{\mathbf{f}}_2) \hat{\mathbf{R}}_i$.

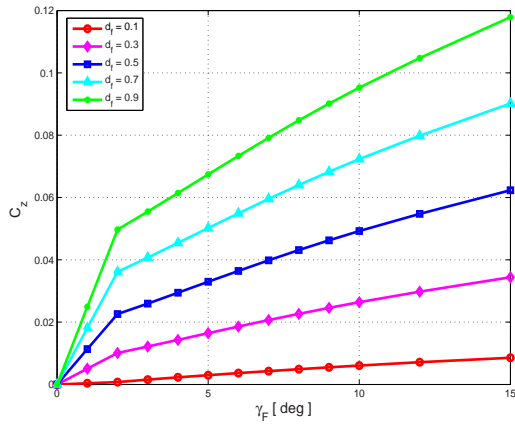
In the fin-fixed reference system, forces are determined in terms of the angle of attack



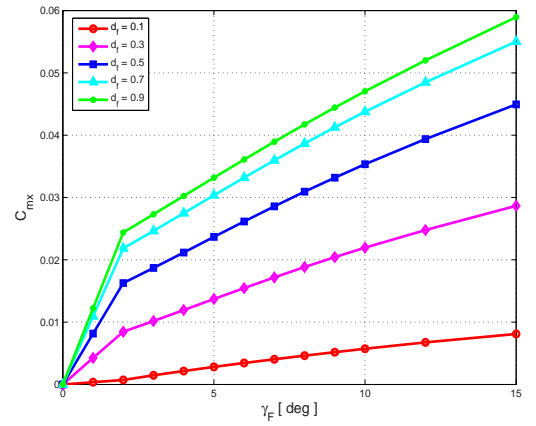
(a)



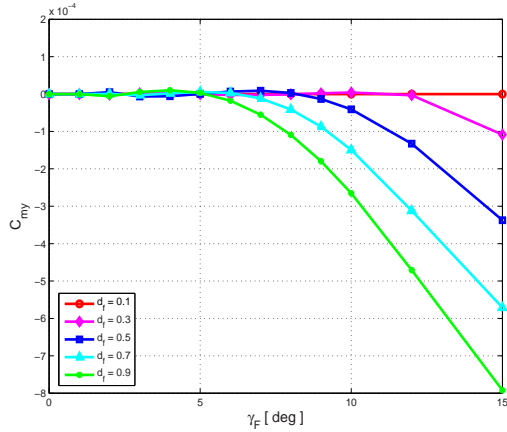
(b)



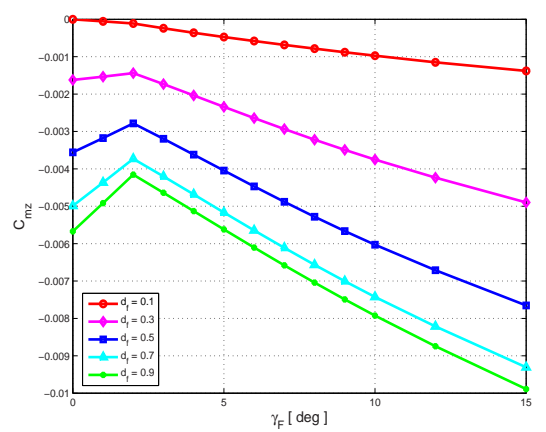
(c)



(d)



(e)



(f)

Figure 11: Fin hydrodynamic force and moment coefficients.

and of the immersion depth, according to previously published results for wedge-shaped fins [17]. The i th fin force and moment components in \mathcal{F}_i ($i = 1, \dots, 4$) are given by

$$\mathbf{s}_{F_i}^{\mathcal{F}_i} = \frac{1}{2} \rho_w v_{F_i}^2 S_{fin}^2 (C_x(\gamma_{F_i}, d_{F_i}), C_y(\gamma_{F_i}, d_{F_i}), C_z(\gamma_{F_i}, d_{F_i}))^T, \quad (27)$$

$$\mathbf{m}_{F_i}^{\mathcal{F}_i} = \frac{1}{2} \rho_w v_{F_i}^2 S_{fin}^3 (C_{mx}(\gamma_{F_i}, d_{F_i}), C_{my}(\gamma_{F_i}, d_{F_i}), C_{mz}(\gamma_{F_i}, d_{F_i}))^T, \quad (28)$$

where v_{F_i} is the magnitude of the velocity vector at the fin frame origin F_i , S_{fin} is the fin span length and C_x, C_y, C_z are force coefficients defined in terms of the fin angle of attack γ_{F_i} and of the immersion depth d_{F_i} . Plots of the force coefficients are shown in fig. 11. Their approximately bilinear behavior for assigned immersion depth ratio is associated with two different flow regimes developing on the fin. The first flow regime occurs for low angles of attack, when two separate cavities are formed at the base and at the leading edge of the fin. For larger angles of attack the two cavities merge to form a supercavity that envelopes all the surfaces except for the pressure face [17]. The procedure for the calculation of the fins' immersion depth is described in Section 2.7.

As in the case of the cavitator force, the considered formulation for the fin forces neglects the effects of hydrodynamic added mass and damping. The fin angle of attack in the local \mathcal{F}_i triad is obtained from the components of the velocity $\mathbf{v}_{F_i}^{\mathcal{F}_i} = (v_x, v_y, v_z)^T$. Accordingly, we have

$$\tan \gamma_{F_i} = \frac{v_z}{v_x}. \quad (29)$$

The fin force components are transformed from the \mathcal{F}_i to the body-fixed triad \mathcal{B} as $\mathbf{s}_{F_i}^{\mathcal{B}} = \mathbf{R}_{\mathcal{B} \rightarrow \mathcal{F}_i}^{\mathcal{B}} \mathbf{s}_{F_i}^{\mathcal{F}_i}$.

2.6 Vehicle/Cavity Interactions

Supercavitating vehicles operate over a wide speed range (50-900 m/s), and experience interactions with the cavity at the after body. Such interactions can be described according to two basic modes: tail-slap and planing. Planing usually occurs at speeds of the order of 50 – 200 m/s, while tail-slap motion is observed at 300 – 900 m/s [10]. During tail-slap conditions, the vehicle undergoes an oscillatory motion with periodic impacts with the cavity, while during planing the vehicle is in contact with the internal surface of the

cavity. The corresponding planing interaction provides lift contribute to counteract the vehicle weight and may stabilize the motion. As planing is expected to be the main mode of operation for torpedoes, our model specifically includes the planing forces by models described in [57] and summarized in section 2.6.2. In the next section, an overview of tail-slap models proposed in the literature is given. These models, whose validity is limited to specific operational conditions, are not used in our investigations.

2.6.1 Tail-slap

Tail-slaps are induced by disturbances and perturbations on the vehicle which result in steady or damped oscillatory motion. This oscillatory motion can be approximated as a rotational motion about the nose, and it has been observed in high-speed bullets such as AHSUM [4]. Two simplified models have been proposed in the past. A simple formulation describes the impact force as directly proportional to the immersion depth through a constant stiffness obtained through empirical observations [53, 47, 19]. A second model is obtained from the two-dimensional momentum-based formulation described in [4, 13], where a simplified expression for the added mass is provided. The general impact problem is described through the momentum conservation principle, which imposes that the momentum of a body before impact must equal the sum of the decreased momentum of the wetted body and the gained momentum of the added mass of fluid after impact [58]. Due to the absence of a refined impact model for a supercavitating vehicle, a more accurate model may be obtained using Hassan’s planing model presented in [57] and summarized in the following section, which may be extended to include a term related to the impact mass $m^*\ddot{h}$ defined in eq. (30) below.

2.6.2 Hassan’s model for planing forces

In [57], Hassan presents a theory that describes forces and moments experienced by a cylindrical body steadily planing on flat and cylindrical free surfaces. The model is in good agreement with experimental data and it is intended for application to supercavitating vehicles. The formulation extends the theory based on Logvinovich’s work for inviscid flow [54, 59] by adding the skin friction force induced by fluid viscosity. The model considers

a planing slender body in steady forward motion on an undisturbed free surface under the assumption of small ratio of immersion depth to body radius and large Froude numbers. A brief review of [54, 59, 57] are presented in what follows. The specific vertical force on the foil planing along the undisturbed horizontal free surface can be expressed as [54, 59]:

$$P = m^* \ddot{h} + \dot{h} \dot{M} \quad (30)$$

The impact mass (m^*) and apparent added mass (M) associated with the non-holonomic dynamics of spray sheet are related as [59, 57]:

$$\dot{m}^* = \frac{2(1+k)}{2k+1} \dot{M}$$

where the parameter k is defined as $V_s/(2\dot{h} \sin \beta)$, with V_s denoting the average spray sheet velocity, while β is the angle between V_s and the horizontal surface as shown in fig. 12. Hassan's model considers the steady planing force associated with the apparent added mass in eq. (30) assuming a constant immersion rate ($\ddot{h} = 0$). Accordingly, the specific force on the planar section reduces to:

$$P = \dot{h} \dot{M} = \dot{h}^2 \frac{\partial M}{\partial h} \quad (31)$$

The planing force on the immersed portion of the body can be obtained by integrating the specific force P (eq. (31)) over the planar section of the wetted surface measured along the longitudinal axis. The planing moment about the center of the cross section at the trailing edge of the immersed body is readily obtained. For the integration, the effective immersion rate ($\dot{h}_e = V_\perp/\chi$) is introduced to account for the average velocity of the thin fluid layer as it is transported along the planing surface [57]. Hence, the planing force and moment are given by:

$$\begin{aligned} \mathbf{s}_p^{\mathcal{B}} &= - \int_0^{l_p} \left(\frac{V_\perp}{\chi} \right)^2 \frac{\partial M}{\partial h} dx \mathbf{n}_3 \\ \mathbf{m}_p^{\mathcal{B}} &= \int_0^{l_p} x \left(\frac{V_\perp}{\chi} \right)^2 \frac{\partial M}{\partial h} dx \mathbf{n}_2 \end{aligned} \quad (32)$$

where V_\perp is the component of the transverse flow velocity perpendicular to the body longitudinal axis, and l_p is the length of the wetted region along the body centerline. Also in eq. (32), the unit vectors $\mathbf{n}_1, \mathbf{n}_2, \mathbf{n}_3$ define a local triad on the vehicle/cavity contact area.

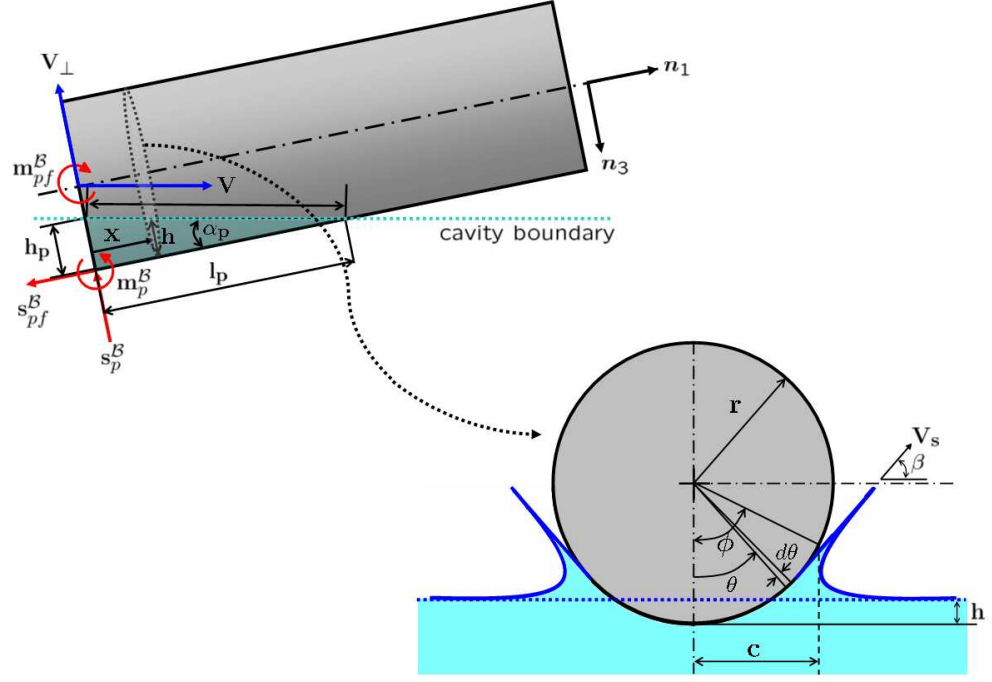


Figure 12: Configuration of planing vehicle and wetted cross section (all forces and moments are described for positive value).

The expression for the unit vectors in terms of the vehicle velocity and body reference is described in Section 2.7.

The transport parameter χ is defined as [57]:

$$\chi = 1 - \frac{\tan \alpha_p}{2\rho_w c} \frac{\partial m^*}{\partial x} \quad (33)$$

where ρ_w is the density of the fluid (water), α_p is the angle of attack between the longitudinal axes of the body and the horizontal free surface, and c is the lateral width of spray sheet shown in fig. 12. The drag and moment due to viscous effects can be written as:

$$\begin{aligned} s_{pf}^B &= -\frac{1}{2}\rho_w V^2 \cos^2 \alpha_p C_{dp} S_w \mathbf{n}_1 \\ \mathbf{m}_{pf}^B &= -\frac{1}{2}\rho_w V^2 \cos^2 \alpha_p C_{dp} S_{wm} \mathbf{n}_2 \end{aligned} \quad (34)$$

where C_{dp} is drag coefficient over a flat surface and V is the flow velocity along the horizontal free surface, which is equal to the component of the vehicle speed along the horizontal free

surface. The wetted area S_w and wetted area including moment arm, S_{wm} , are defined as:

$$\begin{aligned} S_w &= \int_0^{l_p} 2r\phi(x)dx \\ S_{wm} &= \int_0^{l_p} \int_0^{\phi(x)} 2r^2 \cos \theta d\theta dx = \int_0^{L_p} 2r^2 \sin \phi(x)dx \end{aligned} \quad (35)$$

where θ and $\phi(x)$ respectively are the circumferential and maximum angle along the wetted planar surface section shown in fig. 12, while x and r denote respectively the longitudinal coordinate and the cylindrical body radius. The drag coefficient for a fully turbulent flow as assumed in Hassan's model, can be obtained from two formulae [60]:

$$\begin{aligned} C_{dp} &= \frac{0.031}{(Re)^{1/7}} && \text{(over a smooth plate)} \\ C_{dp} &= \left(1.89 + 1.62 \log \left(\frac{l_p}{\epsilon}\right)\right)^{-2.5} && \text{(over a fully rough plate)} \end{aligned} \quad (36)$$

where Re is Reynolds number based on the wetted longitudinal length, which is given by $Re = Vl_p/\nu_k$, with ν_k denoting the kinematic viscosity and ϵ is the average roughness height of the wetted surface.

Assuming a small wetted portion of a cylindrical afterbody planing on a *cylindrical* free surface, the planing forces and moment are modified to read [57, 17]:

$$\begin{aligned} \mathbf{s}_p^B &= -\pi\rho_w r_c^2 V^2 \sin \alpha_p \cos \alpha_p \left(\frac{r+h_p}{r+2h_p}\right) \left(1 - \left(\frac{\Delta}{\Delta+h_p}\right)^2\right) \mathbf{n}_3 \\ \mathbf{m}_p^B &= \pi\rho_w r_c^2 V^2 \cos^2 \alpha_p \left(\frac{r+h_p}{r+2h_p}\right) \left(\frac{h_p^2}{\Delta+h_p}\right) \mathbf{n}_2 \\ \mathbf{s}_{pf}^B &= -\frac{1}{2}\rho_w V^2 \cos^2 \alpha_p C_{dp} \left[\frac{4r\frac{\Delta}{\tan(\alpha_p)}}{\frac{r^3}{2\Delta\tan(\alpha_p)}} \left((1+u_c^2)\tan^{-1}(u_c) - u_c \right) + \left((u_s^2 - \frac{1}{2})\sin^{-1}(u_s) + \frac{1}{2}u_s\sqrt{1-u_s^2} \right) \right] \mathbf{n}_1 \\ \mathbf{m}_{pf}^B &= \frac{1}{2}\rho_w V^2 \cos^2 \alpha_p C_{dp} \left[\frac{8\frac{\Delta}{h_p}\tan^{-1}\left(\sqrt{\frac{h_p}{\Delta}}\right)}{\frac{8}{3}(2\Delta+r)\sqrt{\Delta h_p} - 8\sqrt{\frac{\Delta}{h_p}}(r^2+2\Delta^2) - 16r\sqrt{\Delta}\frac{\Delta}{h_p}} \left(r^2 + 2r\Delta + 2\Delta^2 \right) + \right] l_p \mathbf{n}_2 \end{aligned} \quad (37)$$

where $\Delta = r_c - r$ is the difference between the cavity radius r_c and body radius r , $u_c = \sqrt{h_p/\Delta}$ and $u_s = (2/r)\sqrt{\Delta h_p}$. Accordingly, the cavity vehicle interaction force, \mathbf{s}_I in eq. (10) can be extended as: $\mathbf{s}_I = \mathbf{s}_p + \mathbf{s}_{pf}$, while the relative moments can be added to the moment equation (eq. (11)).

2.7 Computation of Immersion Depths for Afterbody and Fins

This section presents the procedure for the evaluation of the immersion depths required for the evaluation of planing forces and fin forces. The estimation is based on the expression of a time-dependent cavity whose centerline traces the cavitator trajectory based on Logvinovich's independence principle.

2.7.1 Planing immersion depth of the afterbody

The evaluation of the afterbody immersion into the fluid requires knowledge of the cavity shape at the corresponding location. The cavity shape is determined by the velocity of the cavitator at the time it occupied the current tail location, according to Logvinovich's independence principle. It is therefore required to establish the orientation of the cavity relative to the current position of the vehicle. A schematic of the vehicle-cavity system during a maneuver is shown in fig. 13. In the figure t and t_i respectively denote the current time and the instant of time corresponding to the previous integration step. Hence, the current time can be expressed as $t_i + \tau$, where τ is the current time integration step. It is assumed that the time discretization is sufficiently small for the cavity portion near the tail to be approximated as a cylindrical surface with axis parallel to the cavity axis $\underline{\mathbf{t}}$.

At a generic time t , the positions of the tail and of the cavitator can be expressed in the inertial frame as follows:

$$\begin{aligned}\mathbf{r}_T(t) &= \mathbf{r}_G(t) + \mathbf{R}_{\mathcal{B} \rightarrow \mathcal{I}}^{BT}(t) \mathbf{r}_{GT}^{\mathcal{B}} \\ \mathbf{r}_C(t) &= \mathbf{r}_G(t) + \mathbf{R}_{\mathcal{B} \rightarrow \mathcal{I}}^{BT}(t) \mathbf{r}_{GC}^{\mathcal{B}}\end{aligned}\tag{38}$$

where $\mathbf{r}_T(t)$, and $\mathbf{r}_C(t)$ denote the position vectors from the origin of the inertial frame O . Also $\mathbf{R}_{\mathcal{B} \rightarrow \mathcal{I}}^{BT}$, $\mathbf{r}_{GC}^{\mathcal{B}}$ and $\mathbf{r}_{GT}^{\mathcal{B}}$ are the rotation matrix and position vectors from the center of gravity in body fixed frame. The axis of the cavity section formed by the cavitator at instant t_j is identified by the unit vector $\underline{\mathbf{t}}_j$ defined as:

$$\underline{\mathbf{t}}_j = \frac{\mathbf{r}_C(t_{j-1}) - \mathbf{r}_C(t_j)}{|\mathbf{r}_C(t_{j-1}) - \mathbf{r}_C(t_j)|}\tag{39}$$

The evaluation of the unit vector $\underline{\mathbf{t}}_k$ defining the cavity axis at the contact region requires knowledge of the time instants t_k and t_{k-1} which denote the instants of time of cavity

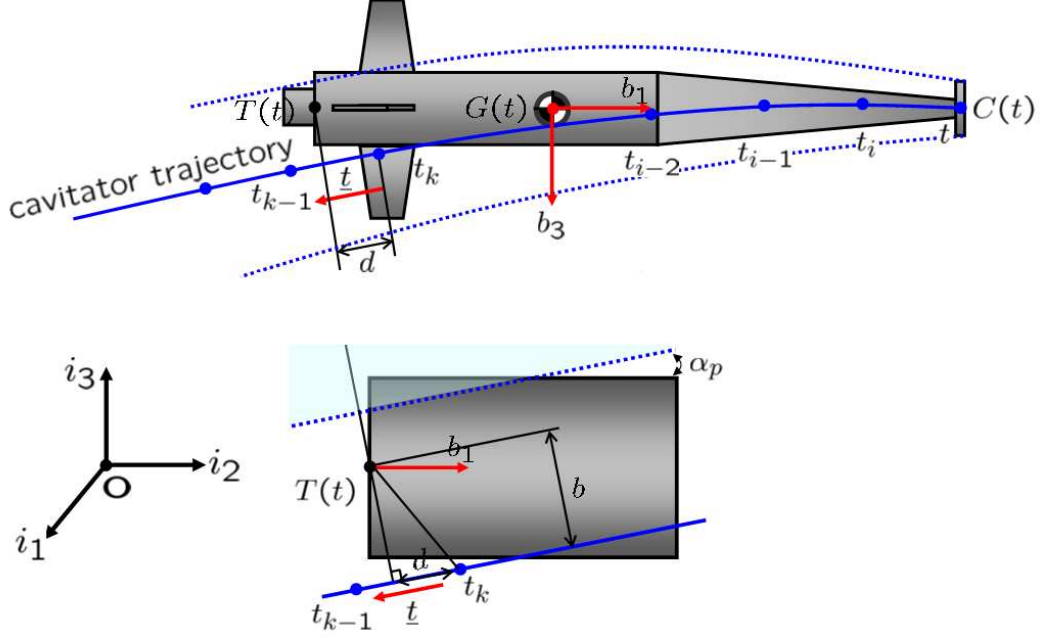


Figure 13: A schematic of vehicle-cavity system over the evolving time.

formation at the tail location. For this reason, it is convenient to define the projected length of the distance from the past cavitation trajectory to the current tail location on the cavity axis as follows:

$$d(t_j) = (\mathbf{r}_T(t) - \mathbf{r}_C(t_j)) \cdot \mathbf{t}_j, \quad j = 1, \dots, i \quad (40)$$

The projected length is positive ($d(t_j) > 0$) when $t_j > t_k$ and it is negative ($d(t_j) < 0$) when $t_j \leq t_{k-1}$. The evaluation of the sign of $d(t_j)$ is used as a criterion to identify t_k , whose search is based on a standard bisection method. From t_k and $d(t_k)$, one can estimate the cavity radius and radial expansion rate as follows:

$$\begin{aligned} r_c(t) &= r_c(\Delta t, \sigma) \\ \dot{r}_c(t) &= \dot{r}_c(\Delta t, \sigma) \end{aligned} \quad (41)$$

where Δt and σ are the passing time since the cavity section of contact region formed and the cavitation number when the cavity section formed. They are obtained as a linear

interpolation between the values at t_k and t_{k-1} :

$$\begin{aligned}\sigma &= (1 - \eta)\sigma(t_k) + \eta\sigma(t_{k-1}) \\ \Delta t &= t - ((1 - \eta)t_k + \eta t_{k-1}) \\ \eta &= \frac{d(t_k)}{|\mathbf{r}_C(t_{k-1}) - \mathbf{r}_C(t_k)|}, \quad 0 \leq \eta \leq 1\end{aligned}\tag{42}$$

Given the cavity axis at the tail location, one can obtain the unit vectors defining the directions of planing moments and forces. The unit vector \mathbf{n}_2 can be obtained as:

$$\mathbf{n}_2 = \frac{\mathbf{b}_1 \times \underline{\mathbf{t}}}{|\mathbf{b}_1 \times \underline{\mathbf{t}}|}\tag{43}$$

By setting $\mathbf{n}_1 = \mathbf{b}_1$, unit vector \mathbf{n}_3 completes a right handed triad: $\mathbf{n}_3 = \mathbf{n}_1 \times \mathbf{n}_2$. The component of the tail velocity along the cavity surface V is given by:

$$\begin{aligned}\mathbf{v}_{\parallel} &= \mathbf{v}_T - (\mathbf{v}_T \cdot \mathbf{n}_2)\mathbf{n}_2 \\ v &= |\mathbf{v}_{\parallel} \cdot \underline{\mathbf{t}}|\end{aligned}\tag{44}$$

where \mathbf{v}_{\parallel} is the projected vector of the tail velocity \mathbf{v}_T on the \mathbf{n}_3 - \mathbf{n}_1 plane, where $\mathbf{v}_T(t) = \mathbf{v}_G(t) + \boldsymbol{\omega} \times \mathbf{r}_{GT}$. The apparent angle of attack of planing can be defined as:

$$\alpha_p = \cos^{-1}(-\underline{\mathbf{t}} \cdot \mathbf{b}_1) - \frac{\dot{r}_c}{v}\tag{45}$$

This apparent angle accounts for the effect of radial expansion rate \dot{r}_c . Finally, the planing immersion depth h_p can be expressed as:

$$\begin{aligned}b &= \sqrt{|\mathbf{r}_T(t) - \mathbf{r}_C(t_k)|^2 - d(t_k)^2} \\ h_p &= r - \frac{r_c - b}{\cos(\alpha_p)}\end{aligned}\tag{46}$$

where b is the distance between the center of afterbody cross section and the cavity center-line.

2.7.2 Fins' immersion depth

A similar procedure can be applied to calculate the fin immersion depth. A schematic of the fin-cavity system during maneuvering is described in fig. 14. The past time t_k and t_{k-1}

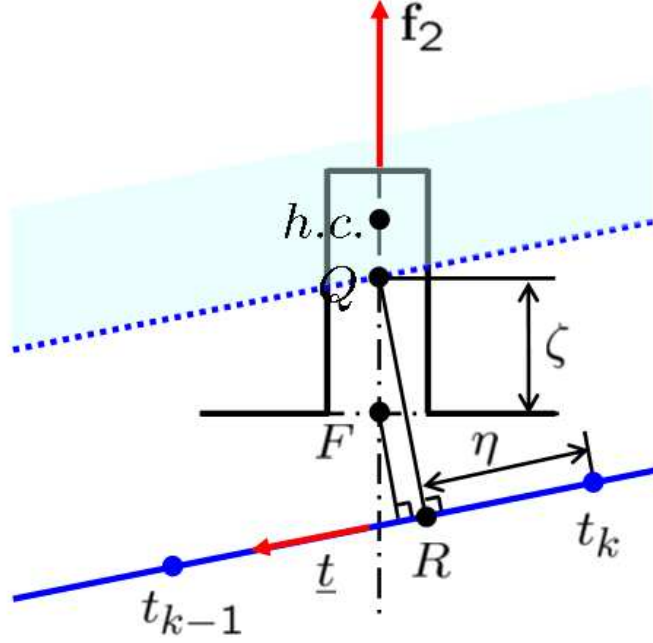


Figure 14: A schematic of fin-cavity system over the evolving time.

now define the cavity orientation at the fins' location. The projected distance along the cavity axis can now be expressed as:

$$d(t_k) = (\mathbf{r}_F(t) - \mathbf{r}_C(t_k)) \cdot \underline{\mathbf{t}} \quad (47)$$

where \mathbf{r}_F defines the position of the root of the fin. We denote as Q the point where the fin intersects the cavity boundary. Its position is given by:

$$\mathbf{r}_Q(t) = \mathbf{r}_F(t) + \zeta \mathbf{f}_2 \quad (48)$$

where ζ defines the non-submerged length of the fin and is a parameter that needs to be determined, while \mathbf{f}_2 is the spanwise unit vector in the local fin frame \mathcal{F} . The cavity centerline corresponding to point Q is defined by the following position vector:

$$\mathbf{r}_R(t) = \mathbf{r}_C(t_k) + \eta \underline{\mathbf{t}} \quad (49)$$

where the non-dimensional parameter η can be obtained by letting $\mathbf{r}_{RQ}(t) \cdot \underline{\mathbf{t}} = 0$ where:

$$\mathbf{r}_{RQ}(t) = \mathbf{r}_F(t) - \mathbf{r}_C(t_k) + \zeta \mathbf{f}_2 - \eta \underline{\mathbf{t}} \quad (50)$$

which gives:

$$\eta = \zeta \mathbf{f}_2 \cdot \underline{\mathbf{t}} + (\mathbf{r}_F(t) - \mathbf{r}_C(t_k)) \cdot \underline{\mathbf{t}} \quad (51)$$

Substituting η into eq. (50) and imposing that $\mathbf{r}_{RQ}(t) \cdot \mathbf{r}_{RQ}(t) = r_c^2$, where r_c is the cavity radius, one obtains a quadratic scalar equation which can be solved for ζ . The fin immersion can be then calculated as $d_{F_i} = S_{F_i} - \zeta$ where S_{F_i} is the fin's span. The angle of attack of the fin is related to the fin's velocity at the hydrodynamic center H , which is assumed to lie at the middle point of the immersed span as:

$$\begin{aligned} \mathbf{v}_{F_i} &= \mathbf{v}_G(t) + \boldsymbol{\omega} \times \mathbf{r}_{GH} \\ \mathbf{r}_{GH} &= \mathbf{r}_{GF}(t) + \frac{1}{2}(S_{F_i} + \zeta) \mathbf{f}_2 \end{aligned} \quad (52)$$

2.8 Conclusions

This chapter describes the formulation of the dynamic equations for a supercavitating vehicle. The model includes simplified hydrodynamic models which describe the cavity configuration, and the interaction of the vehicle with the fluid through fins and nose. These models are generally well accepted in the literature, but they are widely recognized as simplified and highly approximated. However, they can be conveniently used as part of the development of a dynamic flight simulator, as they are computationally inexpensive.

The developed model will be utilized in the next chapter for the analysis of trim configurations. In addition, the trim problem will be used as part of an optimization process which seeks for the optimal vehicle configuration to improve a selected performance index during specified trim operating conditions. The formulation of the optimization problem and the obtained results will be also discussed in the following chapter.

Chapter III

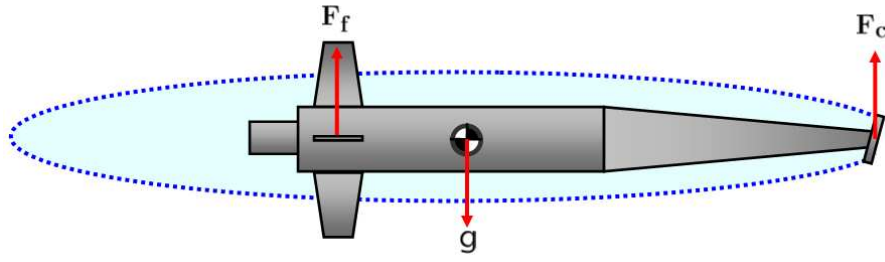
ANALYSIS OF TRIM CONDITIONS

3.1 *Overview*

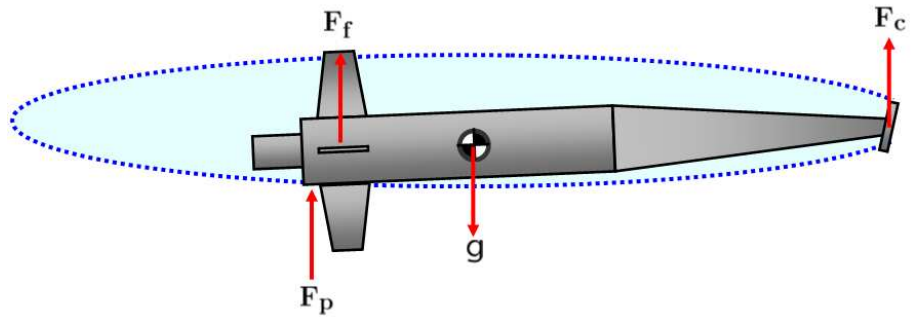
This chapter presents investigations of trim conditions and dynamic characteristics of a notional supercavitating vehicle. The analysis is focused on level flight and level turning flight. In level flight, two trimmed configurations are in particular considered: fins-supported, and fins and planing-supported (fig. 15). In the first case, trim conditions are achieved when propulsion counterbalances the combined drag of nose and fins, and when the lift generated by the fins and the nose balances gravity. In the second case, the planing force and moment alleviate the lift requirements on fins and nose, and they induce additional drag. In level turning flight, trim conditions are achieved by rolling the vehicle such that the vertical component of the combined lift of nose and fins balances gravity, while the horizontal component provides the centripetal force required for turning. Two cavity models, Logvinovich's and Munzer-Reichardt's are considered in level flight and their effects on trim are analyzed in detail. In addition, memory effects related to the cavity's dynamic behavior are also investigated.

3.2 *Nominal Vehicle Configuration*

The considered vehicle configuration reflects projected designs for supercavitating torpedoes. A schematic of the vehicle is presented in fig. 16, while the vehicle nominal dimensions are listed in Table 1. The cavitator is a circular disc, which can rotate about the body axis \mathbf{b}_2 as shown in fig. 9. The cruciform fin arrangement shown in fig. 3 is considered, where the fins oriented parallel to the axis of rotation of the cavitator are denoted as 2 and 4 and are used as elevators, while fins 1 and 3 act as rudders and deflect the same amount.



(a) Fins-supported configuration



(b) Fins and planing-supported configuration

Figure 15: Considered flight configurations.

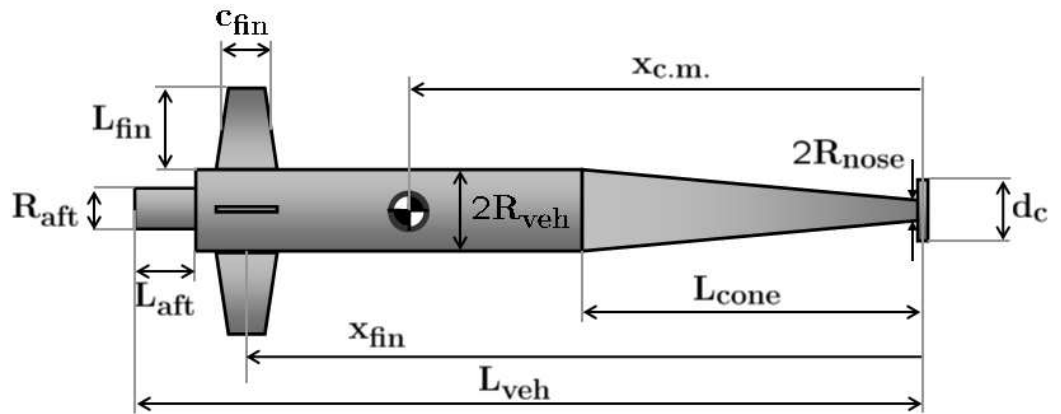


Figure 16: Vehicle configuration.

Table 1: Nominal vehicle dimensions.

Description	notation	value	unit
Vehicle mass	m	150	kg
Cavitator diameter	d_c	0.08	m
Vehicle length	L_{veh}	4	m
Cone length	L_{cone}	1.2	m
Aftertube length	L_{aft}	0.08	m
Vehicle radius	R_{veh}	0.1	m
Nose radius	R_{nose}	0.02	m
Aftertube radius	R_{aft}	0.05	m
Fin span length	L_{fin}	0.2	m
Fin width	c_{fin}	0.1	m
Fin's root location	x_{fin}	3.87	m
Vehicle mass center location	$x_{c.m.}$	2.31	m

3.3 General Formulation of The Trim Problem

The evaluation of the trim configuration for assigned vehicle motion can be formulated as a non-linear algebraic problem, which can be expressed as:

$$\phi(\mathbf{y}, \mathbf{u}) = 0, \quad (53)$$

where $\mathbf{y} = \{\mathbf{w}^B \mathbf{q}_4\}^T$ is a vector containing a subset of the vehicle states, while the control vector $\mathbf{u} = \{\delta_T, \delta_N, \delta_{F_1}, \delta_{F_2}, \delta_{F_3}, \delta_{F_4}\}^T$, includes the propulsion force δ_T , the cavitator angle δ_N , and the fins deflections δ_{F_i} ($i = 1, \dots, 4$).

The considered trim equations are explicitly expressed as:

$$\phi(\mathbf{y}, \mathbf{u}) = \begin{pmatrix} \mathbf{w}^B \times \mathbf{M}^B \mathbf{w}^B - \mathbf{f}^B(\mathbf{y}, \mathbf{u}) \\ \mathbf{v}^B - \mathbf{R}_{B \rightarrow \mathcal{I}}^B \mathbf{v}^{\mathcal{I}} \\ \boldsymbol{\omega}^B - \mathbf{R}_{B \rightarrow \mathcal{I}}^B \boldsymbol{\omega}^{\mathcal{I}} \\ \mathbf{v}^B \cdot \mathbf{b}_2 \end{pmatrix} \quad (54)$$

where the first set of equations corresponds to 6 Euler's equations at trim, $\mathbf{v}^{\mathcal{I}}$ and $\boldsymbol{\omega}^{\mathcal{I}}$ in the second and third equation impose the desired velocity and angular velocity in the inertial frame, and the last expression enforces the condition of the absence of "sideslip". The desired velocity and angular velocity define the assigned trim conditions. For example, the

velocities are assigned as $\mathbf{v}^T = [V \ 0 \ 0]^T$ and $\boldsymbol{\omega}^T = [0 \ 0 \ 0]^T$ for level trim flight, while $\mathbf{v}^T = [V \ 0 \ 0]^T$ and $\boldsymbol{\omega}^T = [0 \ 0 \ \Omega]^T$ define level turning flight conditions.

3.4 Constraints on Trim Conditions

For trim solutions to be found, the vehicle must operate within its flight envelope. The flight envelope of a conventional aircraft is generally determined by various limitations such as control surface stall, available thrust, and structural integrity, which all depend on operating conditions and on vehicle configuration. A supercavitating vehicle is subject to additional constraints related to the dimensions of the cavity in relations to the vehicle dimensions. This section is devoted to the description and the formulation of constraints related to cavity dimensions, while a complete discussion on the flight envelope will be presented from a design perspective in the next chapter.

For assigned geometry and dimensions of the vehicle, the cavity constraints strongly depend on cavitation number (σ), operating conditions (\mathbf{w}), and vehicle attitude (Φ). The constraints for level flight can be expressed as:

$$\mathbf{g} = \mathbf{g}(\sigma(V, h), \mathbf{w}(V), \Phi(\theta)) \quad (55)$$

while for turning flight they are:

$$\mathbf{g} = \mathbf{g}(\sigma(V, \Omega, h), \mathbf{w}(V, \Omega), \Phi(\phi, \theta, \psi)) \quad (56)$$

The cavitation number determines the cavity dimensions, which are directly related to the speed of the vehicle and to the underwater depth h (eq. (15)). Particularly in turning flight, the speed of the nose is determined by a specified velocity of forward motion V , defined by the angular velocity Ω about the vertical inertial axis \mathbf{i}_3 . In addition, the angular velocity Ω generates a curved cavity centerline which causes asymmetric fin immersions due to the discrepancy between the center of the cavity cross section and of the vehicle cross section at the fins' location. This discrepancy can be enlarged or reduced by the vehicle attitude, which defines the location of the vehicle cross section inside the cavity.

During fins-supported flight, the cavity should be small enough to allow the fins to be immersed into the cavity and therefore to provide some lift. On the contrary, the cavity

should be large enough to envelop the entire vehicle and avoid partial cavitation conditions, whereby the behavior of the cavity becomes exceedingly complex and cannot be modeled by the current formulation. Similarly for the fins and planing-supported configuration, the vehicle needs a sufficient pitch angle in level flight and a suitable attitude in level turning flight so that planing forces can supplement the lift provided by the fins. In this case the requirement on the fin immersion can be relaxed.

3.4.1 Level flight

For fins-supported level flight, the constraints can be expressed as a set of inequalities $\mathbf{g} \leq \mathbf{0}$, where:

$$\begin{aligned} g_1 &= R_{veh} - r_c|_{\xi_1} \\ g_2 &= -d_{F_i} \\ g_3 &= -h_p|_{\xi_1} \end{aligned} \tag{57}$$

where ξ_1 is a non-dimensional coordinate defining the location of the afterbody with respect to the nose. The first constraint indicates that the cavity radius must exceed the vehicle radius at the afterbody to avoid partial cavitation. The second constraint enforces the requirement that fins penetrate the cavity boundary, which for level flight with zero pitch angle also restricts the maximum radius of the cavity at the fins' root. The third condition imposes a constraint on the immersion depth which is positive in the case of planing (i.e. when the afterbody is in contact with the cavity) and negative otherwise. In the case of fins and planing-supported flight an additional condition imposes that the immersion depth is small enough for the planing forces to be approximated by eq. (37). This additional constraint can be approximated as:

$$g_4 = h_p|_{\xi_1} - 0.3R_{veh} \tag{58}$$

3.4.2 Turning flight

In turning flight the constraints are defined as:

$$\begin{aligned}
g_1 &= R_{veh} - r_c|_{\xi_1} \\
g_2 &= -d_{F_i} \\
g_3 &= -h_p|_{\xi_1} \\
g_4 &= n - n_{cav} \\
g_5 &= n - n_{fin} \\
g_6 &= h_p|_{\xi_1} - 0.3R_{veh}, \quad \text{if planing is allowed}
\end{aligned} \tag{59}$$

where the last two constraints, which are related to the stall of control surfaces, will be described in detail in the next chapter.

3.5 Practical Implementation of Trim

The general trim formulation allows the evaluation of various operating conditions, which include turns at an imposed angular velocity, and as a particular case, straight level flight. As opposed to an aircraft, the condition of climb and dive cannot be found here as a viable trim solution due to the variation of the cavitation number and related quantities (drag coefficients) with the underwater depth. The direct application of the general formulation for trim however poses some difficulties related to the large number of equations and unknowns and to the discontinuous nature of planing. Therefore, in the following sections, the trim problem is reformulated in light of specific conditions to be investigated with the objective of making its solution more robust.

The equations of motion (eq. (1)) are expressed with respect to the vehicle's center of mass C , and the vehicle kinematic equations (eq. (6)) are expressed in terms of the Euler angles to read:

$$\dot{\mathbf{d}} = \begin{bmatrix} \mathbf{R}^T & \mathbf{0} \\ \mathbf{0} & \mathbf{H}(\Phi) \end{bmatrix} \mathbf{w}^B, \tag{60}$$

where

$$\mathbf{d} = (\mathbf{u}_C^T, \Phi^T)^T \quad (61)$$

$$\Phi = [\phi, \theta, \psi]^T \quad (62)$$

$$\mathbf{H}(\Phi) = \begin{bmatrix} 1 & \sin \phi \tan \theta & \cos \phi \tan \theta \\ 0 & \cos \phi & -\sin \phi \\ 0 & \sin \phi / \cos \theta & \cos \phi / \cos \theta \end{bmatrix} \quad (63)$$

with $\mathbf{H}(\Phi)$ being based on the body rotation 3(ψ)-2(θ)-1(ϕ). Also, the velocity components in body fixed frame are denoted as $\mathbf{v}^B = [u, v, w]^T$, $\boldsymbol{\omega}^B = [p, q, r]^T$. The vehicle is considered axisymmetric so that the inertia tensor of the vehicle reduces to $\mathbf{J}_C = [I_x, 0, 0; 0, I_y, 0; 0, 0, I_z]$.

The trim solution is sought through the solution of the following optimization problem:

$$\begin{aligned} \min_{\Phi^*, \mathbf{u}^*} \quad & \|\mathbf{f}(\Phi^*, \mathbf{u}^*)\|^2, \\ \text{s.t.:} \quad & \mathbf{h}(\Phi, \mathbf{u}) = 0 \\ & \mathbf{g}(\Phi, \mathbf{u}) < 0, \end{aligned} \quad (64)$$

where Φ^* and \mathbf{u}^* are subsets of the Euler angles and of the control vectors. This notation indicates that depending on the trim configuration to be evaluated, some of the Euler angles and of the controls are set to specified values and therefore not considered as variables in the optimization problem. Examples of particular choices for Φ^* and \mathbf{u}^* based on specific trim conditions are provided below. Also in eq. (64), \mathbf{g} expresses the inequality constraints defined in eq. (57), while \mathbf{f} and \mathbf{h} are respectively defined as:

$$\begin{aligned} \mathbf{f}(\Phi, \mathbf{u}) &= \mathbf{w}^B \times \mathbf{M}^B \mathbf{w}^B - \mathbf{f}^B(\Phi, \mathbf{u}) \\ \mathbf{h}(\Phi, \mathbf{u}) &= \begin{bmatrix} \mathbf{v}^B - \mathbf{R}_{B \rightarrow I}^B V \mathbf{i}_1 \\ \boldsymbol{\omega}^B - \mathbf{R}_{B \rightarrow I}^B \Omega \mathbf{i}_3 \\ \mathbf{v}^B \cdot \mathbf{b}_2 \end{bmatrix} \end{aligned} \quad (65)$$

Accordingly, the squared norm $\|\mathbf{f}\|^2$ of the residuals of Euler's equations is the objective function to be minimized under the set of flight path equality constraints which impose a

specified velocity of forward motion V , an angular velocity Ω about the vertical inertial axis, and zero sideslip. Subsets of state (Φ^*) and controls (\mathbf{u}^*) produce complete state and control vectors through flight-path constraints (\mathbf{h}) as well as the specification of trimmed flight classes. These complete sets are used to evaluate cost function ($\|\mathbf{f}\|^2$) and cavity-dimension constraints (\mathbf{g}). Based on the considered trim conditions under investigation, the following set of unknowns and parameters are considered:

3.5.1 Level flight

All of the Euler angles are assigned and some of the controls are set to zero or constrained as follows:

$$\begin{aligned}\Phi &= [0, \theta_0, 0]^T \\ \delta_{F_1} &= \delta_{F_3} = 0 \\ \delta_{F_2} &= -\delta_{F_4}\end{aligned}$$

where the vehicle pitch θ_0 defines whether the vehicle is in contact with the cavity and therefore whether planing forces are active on the body. Accordingly, the variables can be expressed as:

$$\begin{aligned}\Phi^* &= [\]^T \\ \mathbf{u}^* &= [\delta_T, \delta_N, \delta_{F_2}]^T\end{aligned}$$

When the solution of a trim problem is sought, the number of independent equations and variables must be evaluated in order to avoid multiple solutions or infeasible solutions. The conditions of steady state flight ($\dot{\mathbf{w}}^B = 0$ in eq. (2)) enforce that the components of the linear and angular velocity u, v, w, p, q, r are constants or zero. For level flight, eq. (60) and eq. (65) yield zero angular velocity ($p = q = r = 0$). Further, the components of the velocity in the body-fixed frame (u, v, w) are determined from the flight path constraints $\mathbf{h}(\Phi, \mathbf{u})$ in eq. (65). As a result, the two Euler angles θ, ψ and the control vector \mathbf{u} are the variables of the optimization-based trim problem. If all fins are symmetrically attached to the vehicle and the cavitator angle is confined to rotate with respect to the body axis \mathbf{b}_2 ,

then three components of forces and moments ($\mathbf{s}^B \cdot \mathbf{b}_2$, $\mathbf{m}_C^B \cdot \mathbf{b}_1$, $\mathbf{m}_C^B \cdot \mathbf{b}_3$) in eq. (65) are identically zero. Hence there are three independent equations in $\mathbf{f}(\Phi^*, \mathbf{u}^*)$ along with the variables θ , ψ and \mathbf{u} . In order to reduce the number of variables, we can further specify $\theta = \theta_o$, $\psi = 0$, $\delta_{F_2} = -\delta_{F_4}$, $\delta_{F_1} = \delta_{F_3} = 0$. For fins-supported flight, the Euler angle θ_o must be small enough for the vehicle afterbody not to contact the cavity interface. On the contrary, for fins and planing-supported flight, θ_o must be large enough for planing to occur. As a result of this process, there remain three variables (δ_T , δ_N , δ_{F_2}) and three independent equations which define a well-defined trim problem.

3.5.2 Turning flight

When the vehicle performs a turn, the cavity centerline has a curvature which causes the center of the cavity cross section at the fin's location and at the afterbody to deviate from the center of the vehicle cross section. This discrepancy produces asymmetric hydrodynamic forces and moments on the fins. Consequently, six equations in eq. (1) contribute independently to trim, plus the zero sideslip condition expressed in eq. (65). The design variables include the following subset of the states:

$$\Phi^* = [\phi, \theta, \psi]^T$$

and a subset of the controls \mathbf{u} . A square problem is obtained by specifying δ_{F_2} as any arbitrary value δ_e and by letting $\delta_{F_2} = -\delta_{F_4}$. In here, δ_e is chosen as the trimmed control value in level flight. Accordingly, the variables include the following subset of the controls:

$$\mathbf{u}^* = [\delta_T, \delta_N, \delta_{F_1}, \delta_{F_3}]^T$$

This results in seven variables and seven independent equations. Alternatively, level turning flight can be also performed allowing a small sideslip: the absence of sideslip $\mathbf{v}^B \cdot \mathbf{b}_2$ can be replaced by imposing the condition $\psi = \psi_0$. In this case, the following parameters are specified:

$$\psi = \psi_0$$

$$\delta_{F_1} = -\delta_{F_3}$$

$$\delta_{F_2} = -\delta_{F_4}$$

and the variables are:

$$\begin{aligned}\mathbf{\Phi}^* &= [\phi, \theta]^T \\ \mathbf{u}^* &= [\delta_T, \delta_N, \delta_{F_1}, \delta_{F_2}]\end{aligned}$$

3.5.3 Cavity memory effects

For trim solutions, one must specify the history of the vehicle motion according to the considered trim configurations to determine the cavity shape at the current time. In general, the vehicle motion in the past time can be determined by backward-integrating the vehicle kinematic equations (eq. (60)). In level flight, the generalized velocity \mathbf{w} and the Euler angles $\mathbf{\Phi}$ remain constant, while the position of the vehicle changes according to kinematic equations (eq. (60)), which reduce to $\dot{\mathbf{u}}_C = \mathbf{v}^{\mathcal{I}}$ for a straight trajectory. As a result, the memory effects do not affect the cavity shape in level trim conditions. However, in level turning flight, the cavity is generated along the cavitator trajectory and hence memory effects are significant. For example, in steady (constant speed) turning flight, the history of the vehicle motion is computed by backward-integrating the vehicle kinematic equations (eq. (60)) and $\mathbf{v}^{\mathcal{B}} = \mathbf{R}_{\mathcal{B} \rightarrow \mathcal{I}}^{\mathcal{B}} \mathbf{v}^{\mathcal{I}}$ and $\boldsymbol{\omega}^{\mathcal{B}} = \mathbf{R}_{\mathcal{B} \rightarrow \mathcal{I}}^{\mathcal{B}} \boldsymbol{\omega}^{\mathcal{I}}$. The angular velocity in the inertial frame $\boldsymbol{\omega}^{\mathcal{I}}$ remains constant, while the rotation tensor $\mathbf{R}_{\mathcal{B} \rightarrow \mathcal{I}}^{\mathcal{B}}$ changes according to the Euler angles $\mathbf{\Phi}$ and the linear velocity in the inertial frame $\mathbf{v}^{\mathcal{I}}$ is calculated by $\mathbf{v}^{\mathcal{I}} = \boldsymbol{\omega}^{\mathcal{I}} \times \mathbf{u}_{TC}$. At a generic time t (the past time), the vector \mathbf{u}_{TC} denotes the position vector of the vehicle's center of mass from the center of turn ($\mathbf{u}_{TC}(t) = \mathbf{u}_C(t) - \mathbf{u}_T(0)$). At the initial time $t = 0$, the position of the center of turn can be determined from the following relation:

$$\begin{aligned}\mathbf{u}_T(0) &= \mathbf{u}_C(0) - \mathbf{u}_{TC}(0) \\ \mathbf{v}^{\mathcal{I}}(0) &= \boldsymbol{\omega}^{\mathcal{I}} \times \mathbf{u}_{TC}(0)\end{aligned}\tag{66}$$

where the position vector of the center of turn \mathbf{u}_T is fixed in the inertial frame independent of time. For example, if the vehicle has $\mathbf{v}^{\mathcal{I}} = [v_1, 0, 0]^T$ and $\boldsymbol{\omega}^{\mathcal{I}} = [0, 0, \omega_3]^T$ at the initial time, the center of turn is:

$$\mathbf{u}_T(0) = \mathbf{u}_C(0) - [0, -\frac{v_1}{\omega_3}, 0]^T\tag{67}$$

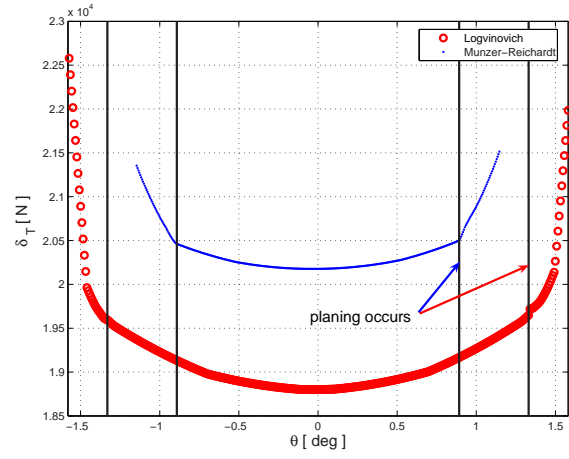
3.6 Results for Level Flight

This section presents parametric studies and sample dynamic simulations for level flight. Calculations consider the two cavity models described in the previous chapter and the trim configurations shown in fig. 15. Sensitivity to different cavity formulations and influence of pitch angle θ_0 and velocity of forward motion V are investigated.

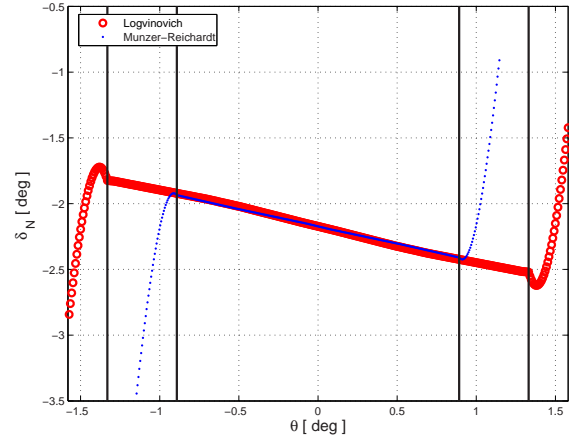
3.6.1 Influence of pitch angle and velocity of forward motion

Figure 17 shows the variation of the trim controls with respect to the specified pitch angle θ_0 . The plots directly compare the results obtained using the two cavity models, and show a clear transition between fins-supported and fins and planing-supported flight. For convenience, the pitch angles corresponding to the onset of planing are indicated by vertical lines in figs. 17.(a)-(c). The results show how Logvinovich model predicts a larger cavity, which corresponds to a larger value of the pitch angle required for planing ($\theta_0 = 1.331^\circ$ for Logvinovich, $\theta_0 = 0.892^\circ$ according to Munzer-Reichardt). It is interesting to observe that all controls appear symmetric with respect to an angle $\theta_0 < 0$, which is due to the fact that the trim angles for cavitator and fins are non-zeros for $\theta_0 = 0$. As the pitch angle increases, the thrust force varies parabolically in the fins-supported region and increases rapidly in the fins and planing-supported region. Also noteworthy is the fact that the thrust obtained with Logvinovich's cavity model is lower than the one found using Munzer-Reichardt's. A larger cavity in fact reduces the fins' immersion depth, and the corresponding drag. The reduction in immersion depth is compensated by a higher fins angle of attack as shown in fig. 18.

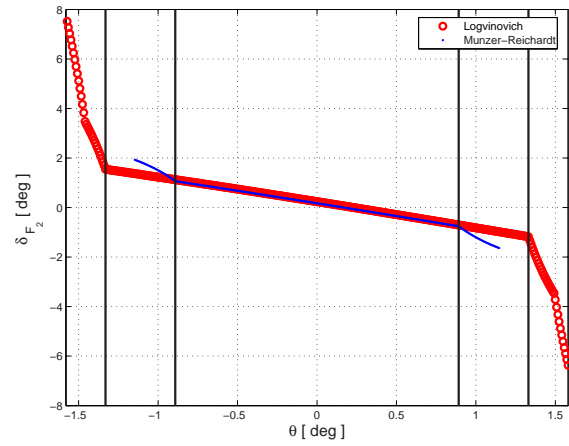
Fig. 19 shows the variation of the trim controls with respect to the vehicle forward velocity V . A main feature in the variation of the controls is that the elevator angle increases with the velocity V as a result of the decreased immersion depth, while the cavitator angle decreases in order to sustain the same lift which otherwise increases with the velocity. Consequently higher thrust is required to counterbalance more drag induced by the decreased cavitator angle as well as increased velocity. The discontinuous slope in the elevator angle



(a) Thrust



(b) Cavitator angle



(c) Elevator fin angle

Figure 17: Variation of controls in terms of pitch angle (cavitation number $\sigma = 0.0294$).

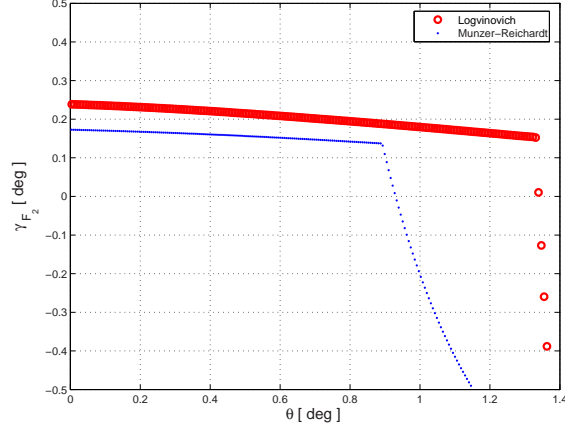
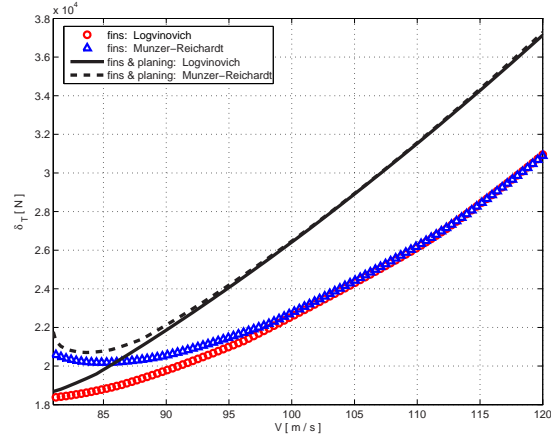


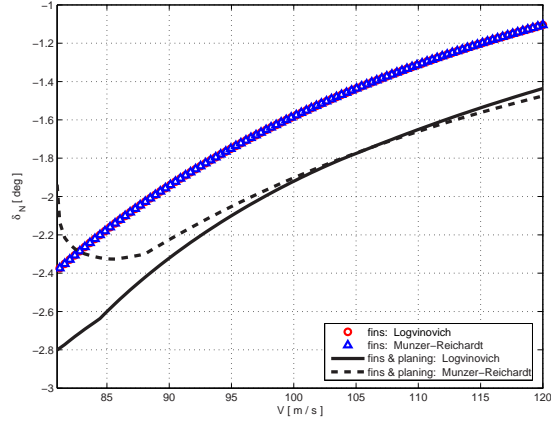
Figure 18: Variation of elevator angle of attack with respect to pitch angle (cavitation number $\sigma = 0.0294$).

variation is due to the bilinear behavior of the hydrodynamic fin coefficients. At low velocity, small control angles are required for trim and two separate cavities are formed on the fin's surface. In contrast, at high velocity, the large control angles required to compensate for the reduced immersion depth cause the two cavities to merge into a single supercavity (see fig. 11 (c)). This behavior is confirmed by the different velocity associated with the discontinuity-onset predicted by Logvinovich's and Munzer-Reichardt's models. A larger cavity in fact reaches earlier the conditions where the fin control angles are large enough to generate the supercavity.

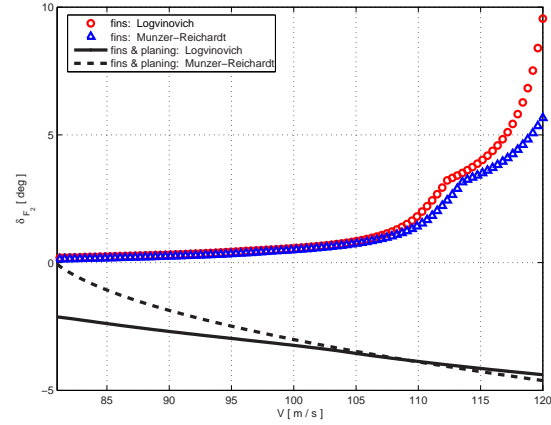
Planing leads to a higher increasing rate for the thrust for both cavity models and requires higher cavitator angles as demonstrated in fig. 19 (b). For the vehicle to be planing, a sufficient positive pitch angle must in fact be provided, which reduces the angle of attack of the cavitator. As a result, the cavitator requires more deflection in order to maintain the same lift. In this case we consider a small planing angle corresponding to a planing depth $h_p|_{\xi_1} = 0.01R_{veh}$. Fig. 19 (c) shows that the fin control angles are negative for both cavity models: this confirms that planing alleviates the fin's lift requirements. The discrepancy between the two cavity models decreases as velocity increases, as a result of the reduction of the cavitation number (see fig.s 6 and 7). Accordingly, the fin immersion depth (fig. 20) and the cavitator angle approach the same values at high velocity. It is important that



(a) Thrust



(b) Cavitator Angle



(c) Elevator fin angle

Figure 19: Variation of controls in terms of forward velocity V (the planing depth is fixed $h_p|_{\xi_1} = 0.01R_{veh}$ when the vehicle is planing).

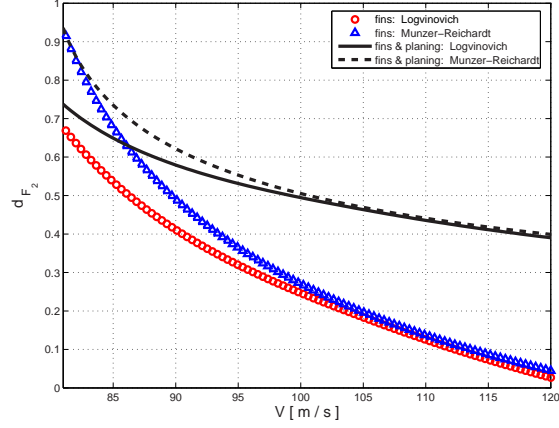


Figure 20: Fin immersion depth versus speed of forward motion.

the patterns of variation in thrust and fin immersion depth ratio show a great similarity. This implies that the difference of fin immersion depth is an essential reason for the trim conditions to vary with the trim configurations as well as the cavity models.

3.6.2 Dynamic simulations

Sample simulation results are provided for the two trim configurations considered. The vehicle's equations of motion are integrated in time to predict the dynamic behavior of the vehicle for assigned controls' time histories. Specifying constant controls at the trim values allows evaluating the validity of the estimated trim configurations, and their stability with respect to numerical perturbations associated with the numerical integration process. Perturbations of the trim configurations are also considered to highlight potential vehicle instabilities. All the simulations consider Logvinovich model, and in the case of perturbation on the trim controls a direct comparison is presented for results obtained with and without the estimation of cavity memory effects described in Chapter 2.

3.6.2.1 Fins-supported level flight

The operating condition and trim controls for fins-supported level flight are presented in Table 2. When the controls are maintained constant at the calculated trim values, the simulations show that the vehicle maintains the required straight leveled trajectory (see fig. 21), which indicates both the validity of the solution and the stability of the considered

Table 2: Fins-supported straight level trimmed flight.

<i>variable</i>	<i>value</i>	<i>unit</i>
ϕ	0	degree
θ	0	degree
ψ	0	degree
V	78	m/s
Ω	0	rad/s
δ_T	18.3176e+3	N
δ_N	-2.5673	degree
δ_{F_2}	0.1576	degree
δ_{F_4}	-0.1576	degree
δ_{F_1}	0	degree

operating condition with respect to numerical inaccuracies.

Dynamic simulations are also conducted in the presence of perturbations on the elevator's control, whose considered variation is depicted in fig. 22. The angle is increased starting at time 0.1 sec to reach a peak value of $\delta_{F_2} = 3.3^\circ$ at 0.15 sec. It finally returns to the trim value after 0.2 sec. The perturbation is quite large and sufficient to induce planing motion and to test the vehicle's stability in severe conditions. Results are obtained for cavity models with and without memory effects so that their influence can be directly observed. Figure 23 presents selected vehicle states in response to the considered perturbation and shows the strong influence of memory effects on the behavior of the vehicle. Both simulations show that the perturbations have a de-stabilizing effect on the motion of the vehicle. However, the effect is most dramatic if memory effects are neglected. The corresponding forces on fins and afterbody are shown in fig.s 24 and 25: the oscillatory behavior of the vertical force components suggests the presence of interactions with the cavity and planing. Neglecting memory effects in the formulation causes more severe interactions and oscillations.

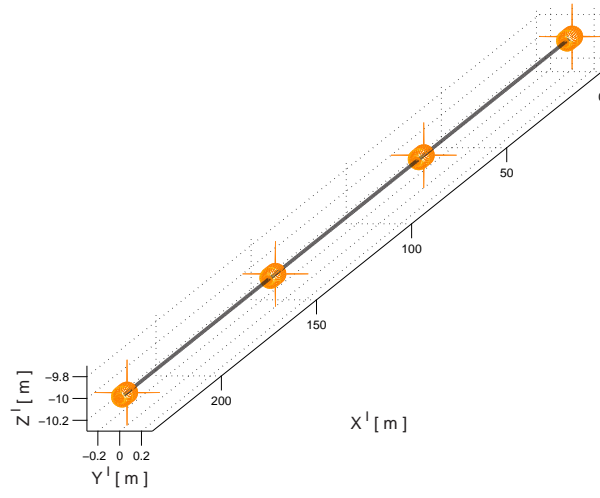


Figure 21: Trajectory of vehicle during fins-supported trimmed flight.

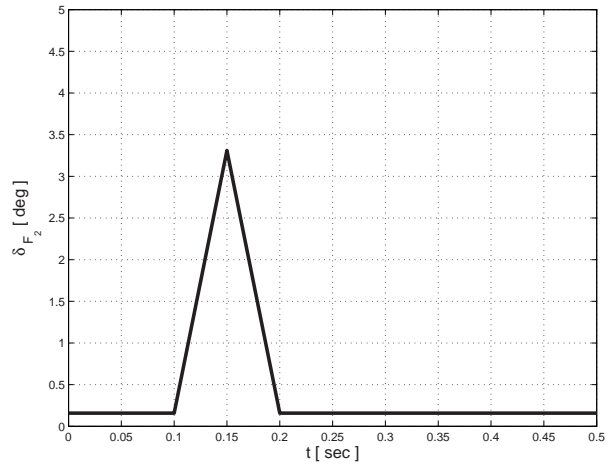
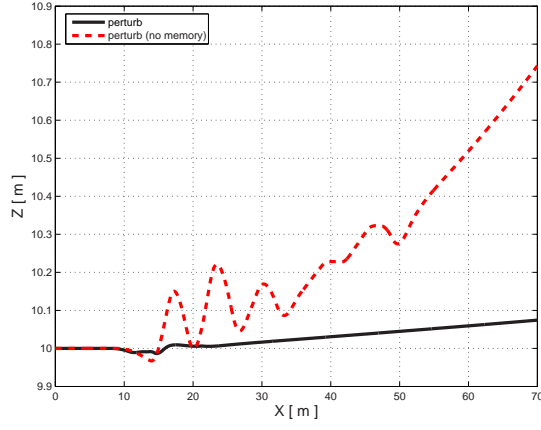
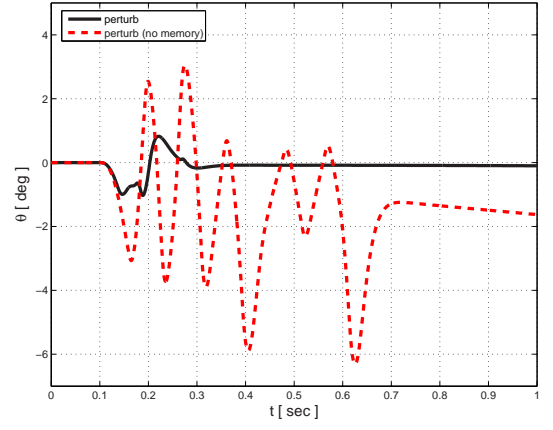


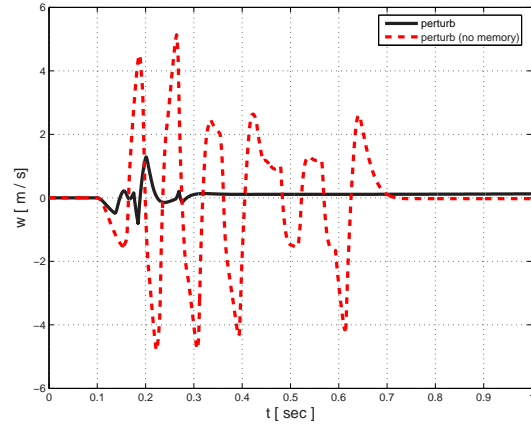
Figure 22: Time history of perturbed control angle.



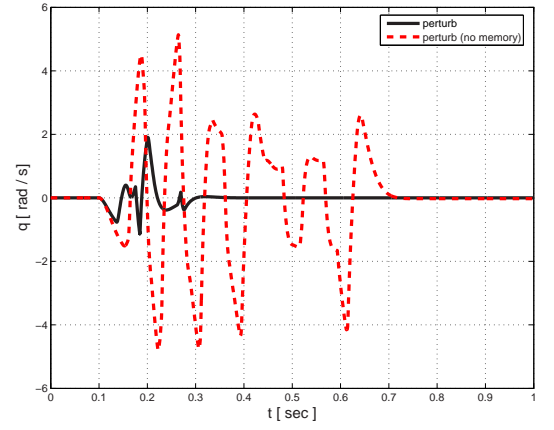
(a) Altitude



(b) Pitch angle

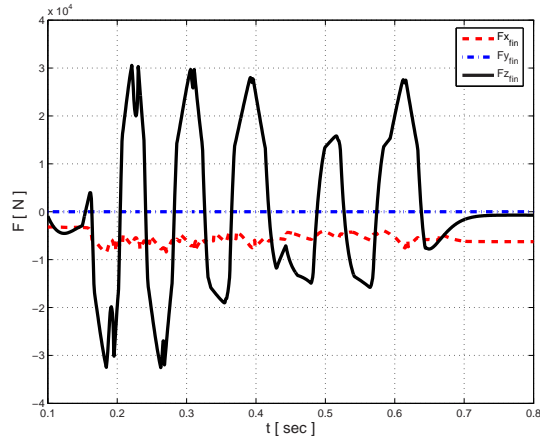


(c) Linear velocity

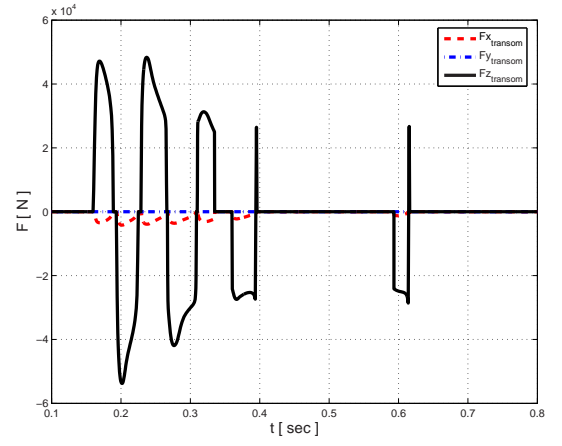


(d) Angular velocity

Figure 23: Simulation results during perturbed fins-supported trimmed flight considering cavity with and without memory effects.

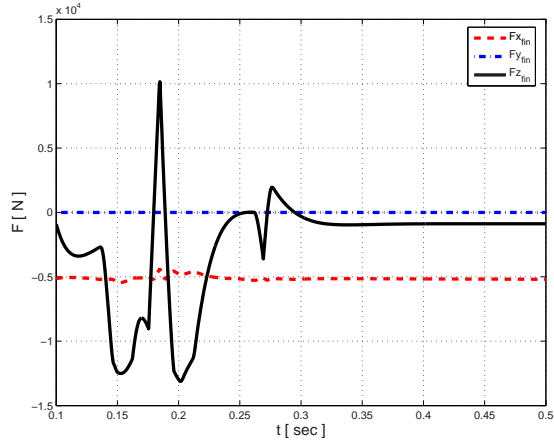


(a) Forces on the fins

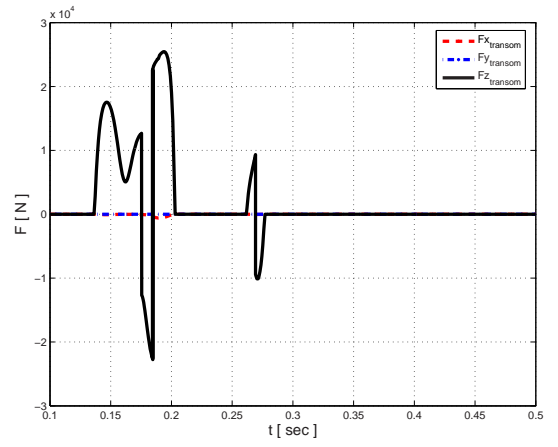


(b) Forces on the afterbody

Figure 24: Forces without memory effects.



(a) Forces on the fins



(b) Forces on the afterbody

Figure 25: Forces with memory effects.

3.6.2.2 Fins and planing-supported level flight

Results for fins and planing-supported straight level flight are presented in Table 3. The simulations consider a small planing depth $h_p|_{\xi_1}/R_{veh} = 0.05$, a total simulation time of 3 sec, and include memory effects.

Table 3: Fins and planing-supported straight level trim flight.

<i>variable</i>	<i>value</i>	<i>unit</i>
ϕ	0	degree
θ	0.4963	degree
ψ	0	degree
V	78	m/s
Ω	0	rad/s
δ_T	18.2920e+3	N
δ_N	-3.0267	degree
δ_{F_2}	-2.2046	degree
δ_{F_4}	2.2046	degree
δ_{F_1}	0	degree

During the simulation time, initial deviations from the desired level flight trajectory can be observed as shown in fig. 26. Small oscillations can also be noticed in the angular and linear velocity components shown in fig. 27.

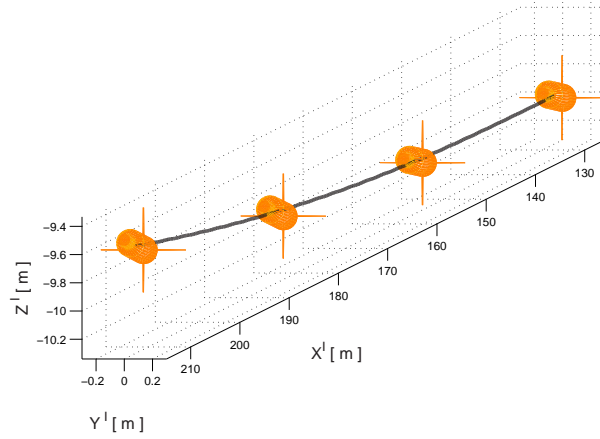


Figure 26: Trajectory in fins and planing-supported flight: vehicle configuration at 1.5, 1.8, 2.2, 2.5 sec.

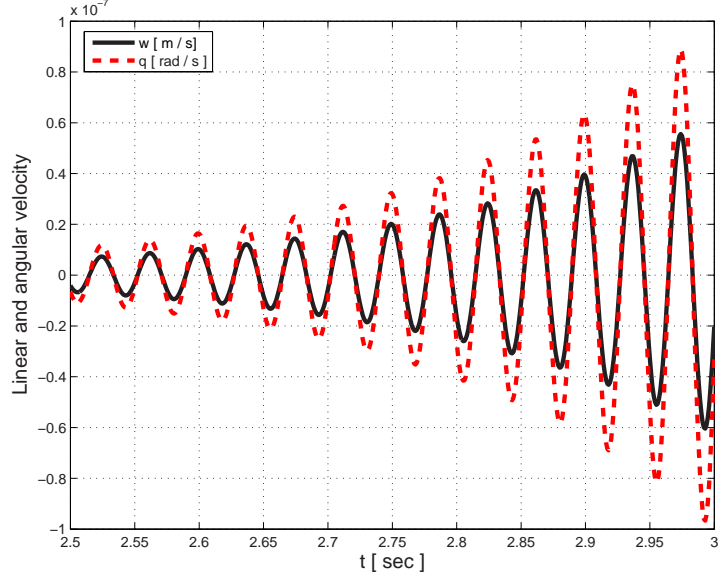
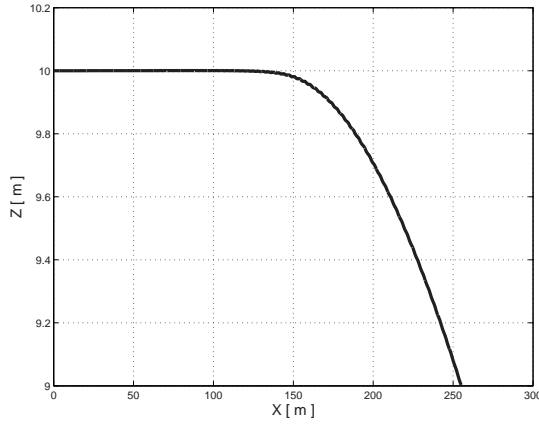


Figure 27: Linear and angular velocities of the vehicle during fins and planing-supported trimmed flight.

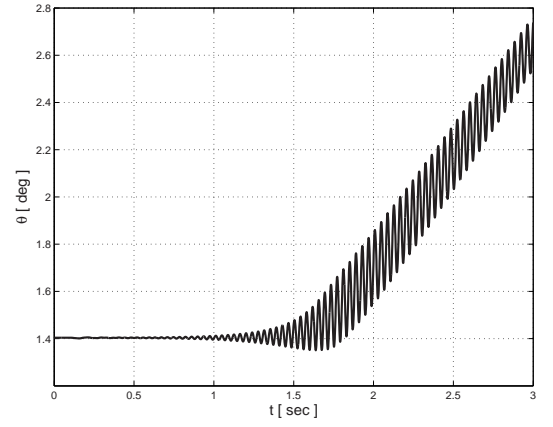
Planing requires a positive pitching angle for the afterbody to be immersed into the cavity boundary. In spite of the small pitch angle (planing depth), the planing force on the transom is relatively large and can be responsible for the diverging oscillatory motion of the vehicle particularly in the longitudinal mode as shown in fig. 27. Although the values are extremely small within the simulation time, this shows the potential for instability of this operating condition.

The behavior of the vehicle is again investigated in the presence of perturbations of the controls. The same time history shown in fig. 22 is considered for the elevator angle. In this case, however, the perturbation amplitude is much lower, equal to 1% of the trimmed value. Representative simulation results for some of the states are presented in fig. 28, while fig. 29 shows the corresponding time histories of the forces on fins and afterbody.

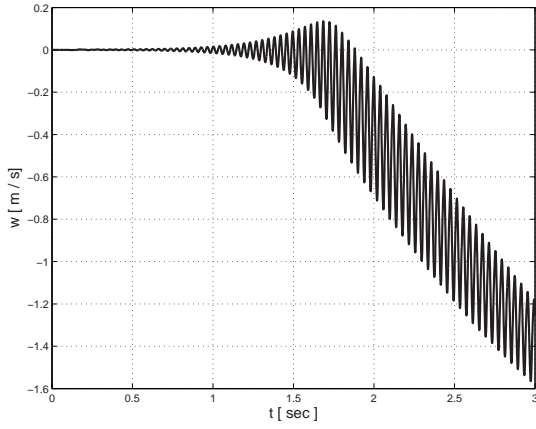
In spite of the small perturbation on the elevator angle, the planing force on the transom causes the oscillatory motion of the vehicle particularly in the longitudinal mode. The trajectory as represented by the z inertial coordinate (fig. 28 (a)) shows that the vehicle deviates from the straight flight path and climbs while undergoing an oscillatory motion. It is interesting that the period (about 0.0400 sec) of the oscillations is slightly lower than



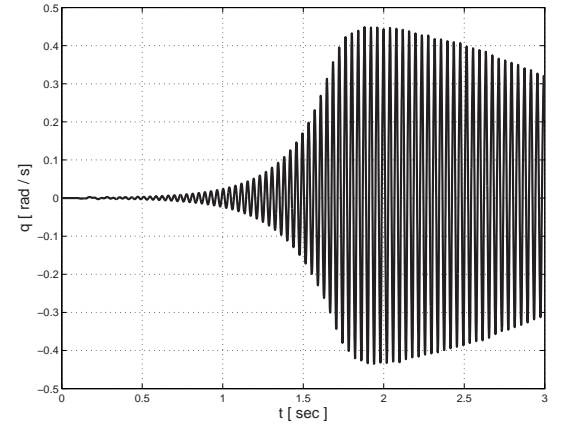
(a) Altitude



(b) Pitch angle

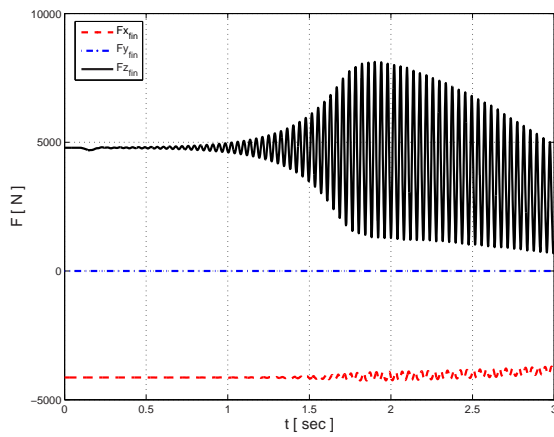


(c) Linear velocity

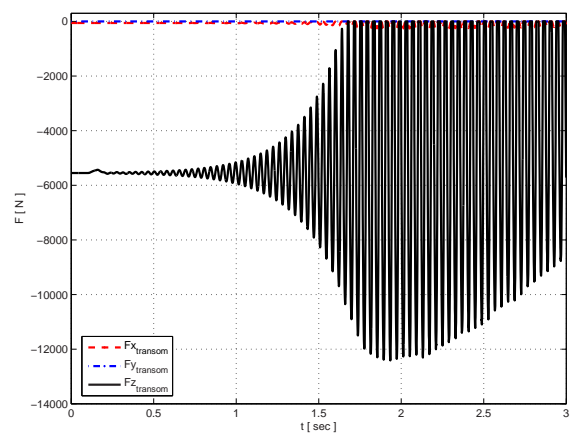


(d) Angular velocity

Figure 28: Simulation results during perturbed fins and planing-supported trimmed flight.



(a) Forces on the fins



(b) Forces on the afterbody

Figure 29: Forces on fins and afterbody resulting from control perturbation.

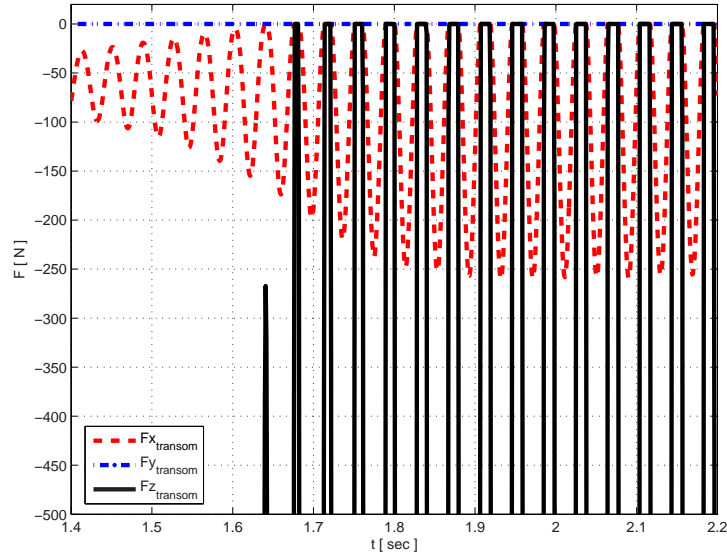


Figure 30: Detail of forces on the afterbody during perturbed fins and planing-supported trimmed flight.

the characteristic time related to cavity memory effects ($L_{veh}/V = 0.0470$ sec). The hydrodynamic forces' oscillatory variations reflect the oscillatory motion of the vehicle. The transom periodically impacts the lower internal surface of the cavity which correspond to force components along the z direction always below zero as shown in fig. 29 (b). This can be clearly noticed from the detail of the force variation shown in fig. 30. This oscillation exists and shows the same patterns even if larger perturbations were considered. The observed oscillatory motion can be interpreted as similar to the porpoising motion of a high-speed marine craft, which consists in self-excited oscillations caused by the coupling of the restoring coefficients between pitch and heave [61]. These oscillations can cause severe structural damage of the control surfaces and can degrade their control effectiveness (see fig. 29 (a)).

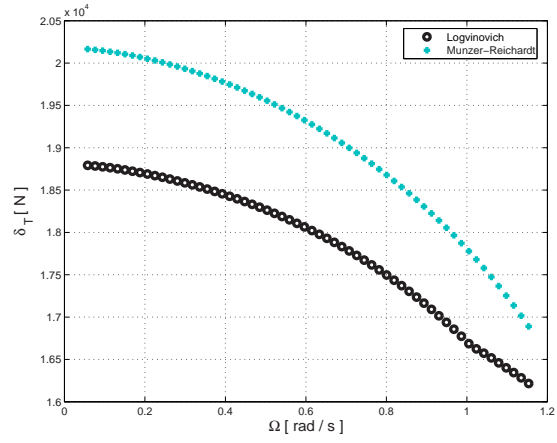
3.7 Results for Level Turning Flight

Trim in level turning flight is investigated in terms of the angular velocity Ω about the vertical inertial axis i_3 . Solutions are obtained using the two cavity models. Investigation of the influence of memory effects is then carried out using Logvinovich's model only, so

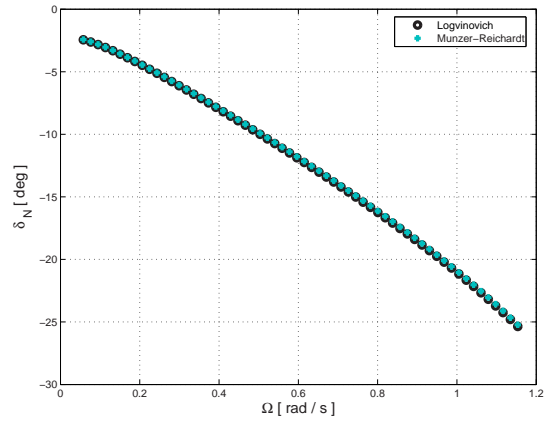
that the influence of cavity size and radial expansion rate are removed from the comparison.

3.7.1 Influence of angular velocity

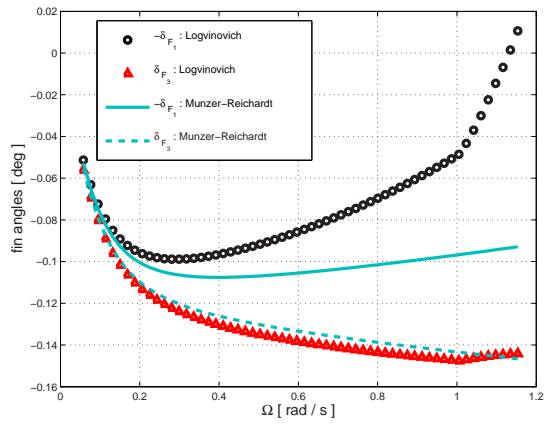
Fig. 31 shows the variation of the trimmed controls with respect to the angular velocity Ω for the two cavity models. The results are obtained for $\delta_{F_2} = -\delta_{F_4} = 0.180^\circ$. An interesting and counterintuitive behavior can be observed for the required thrusts which gradually decreases as the angular velocity increases. This surprising tendency is related to the drag coefficient of the cavitator. When a conventional vehicle performs a turn, it requires larger lift than in straight level flight to produce sufficient centripetal force. As a result, the vehicle experiences a larger drag force. In contrast, the hydrodynamic drag force of the cavitator decreases as its angle of attack increases (see eq. (25)). The cavitator angle (magnitude) hence increases in order to produce sufficient lift. Particularly, in this case, the d.o.f. of the cavitator is one and the lift by the cavitator plays an essential role. As observed in level flight, the thrust force predicted by Logvinovich's cavity model is smaller than the one corresponding to Munzer-Reichardt's, while the cavitator angles are approximately the same. Significant variations can be observed between the control angles of two rudders (δ_{F_1} , δ_{F_3}) which are shown in fig. 31 (c). The Euler angles corresponding to trim at increasing Ω are shown in fig. 32, where the angles are normalized by their maximum value predicted by Logvinovich's cavity model with memory effects, i.e. $\phi = 84.2736^\circ$, $\theta = 0.1112^\circ$, and $\psi = 1.1091^\circ$. The roll angle increases in order to convert the lift of the cavitator into centripetal force. Pitch and yaw angles are relatively small and the yaw-to-pitch ratio is of the order of 10 at high angular velocity. These angles vary with the roll angle and interact with each other in order to maintain zero sideslip during level turning flight. Such small angular values allow the roll angle in a bank-turn to be approximated as $\phi \approx \tan^{-1}(\frac{V\Omega}{g})$, with g denoting gravity. It is interesting that when the angular velocity Ω is about 1 rad/s, the discontinuous slopes for both attitude angles induce the slope discontinuity on two rudder fin angles and on the thrust force in Logvinovich's model. In contrast, all trimmed controls and attitude in Munzer-Reichardt's model have continuous slopes. This may be related to the fact that the discontinuity-onset angular velocity in Logvinovich's model



(a) Thrust



(b) Cavitator angle



(c) Rudder fin's angles

Figure 31: Variation of controls in terms of angular velocity of turning flight Ω .

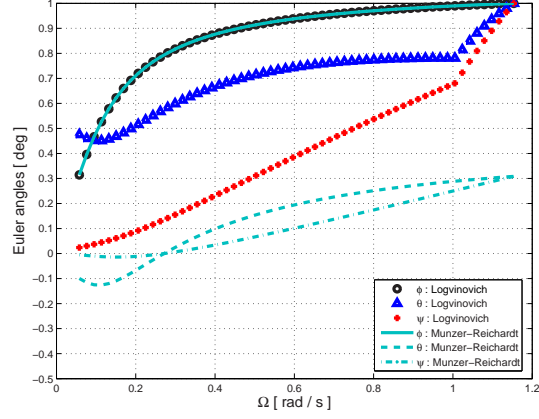


Figure 32: Variation of normalized Euler angles in terms of angular velocity of turning flight Ω .

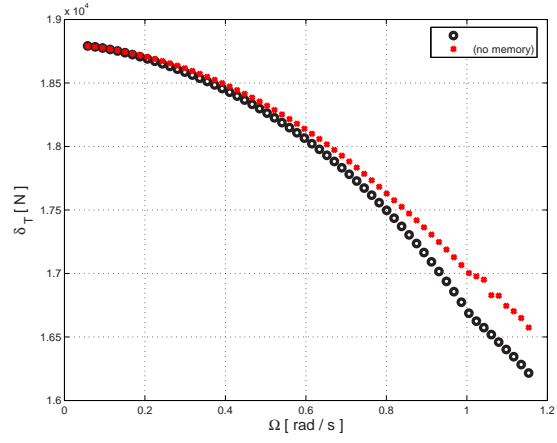
is lower than Munzer-Reichardt's model because the latter requires smaller fin angles of attack.

3.7.2 Cavity memory effects

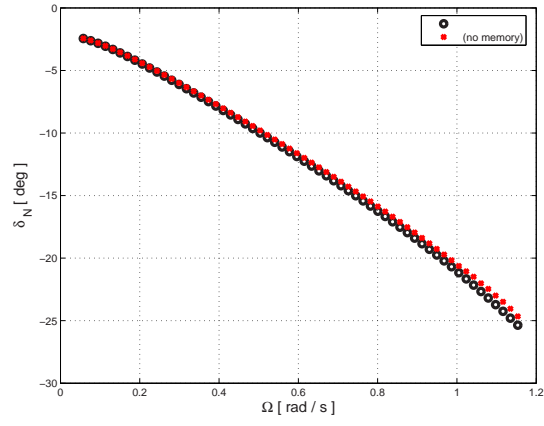
The influence of memory effects on the trim solutions is illustrated in fig.s 33 and 34. Figure 33 compares the variation of thrust and cavitator control angle versus the velocity Ω , and indicates that these two control values are not strongly affected by the addition of memory effects. Strong influence can instead be observed on the fins' angles and on the Euler angles at high roll angles, as demonstrated by fig. 34. Memory effects induce larger deflection of the rudder fins over the intermediate range of the roll angle. It is interesting in particular that the deflection of the down rudder fin (δ_{F_3}) without memory effects becomes very large at high roll angle. Memory effects considerably affect attitude and fin immersion at high angular velocity (i.e. at high roll angle). Figure 35 summarizes the variation of the fin immersion depth ratio in terms of the roll angle as predicted by models with and without memory effects. The schematic plot confirms that strong differences occur at high roll angles, while for small values of roll differences appear negligible.

3.7.3 Simulations in level turning flight

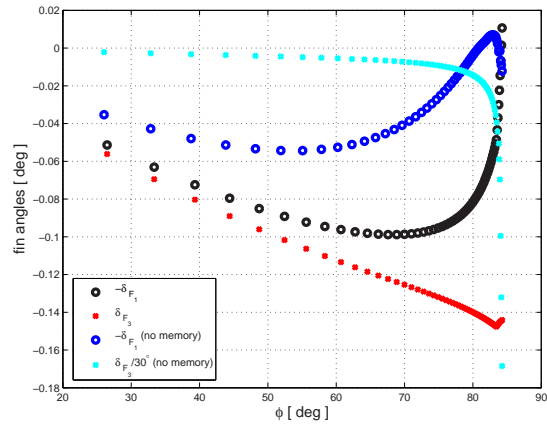
A sample trim condition for fins-supported level turning flight is presented in Table 4, which corresponds to a turn characterized by a large roll angle. Fig. 36 shows the trajectory



(a) Thrust



(b) Cavitator angle



(c) Rudder fin's angles

Figure 33: Variation of controls with and without memory effects.

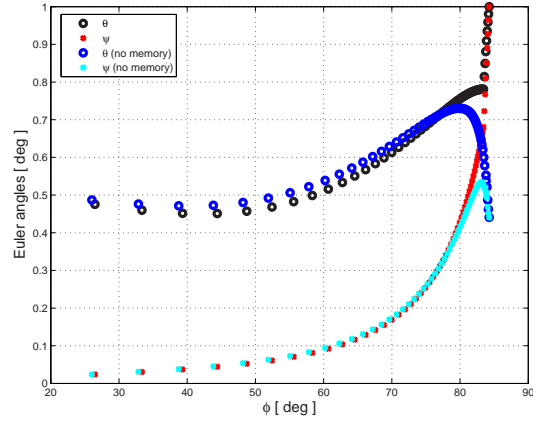


Figure 34: Pitch and yaw versus roll angle with and without memory effects.

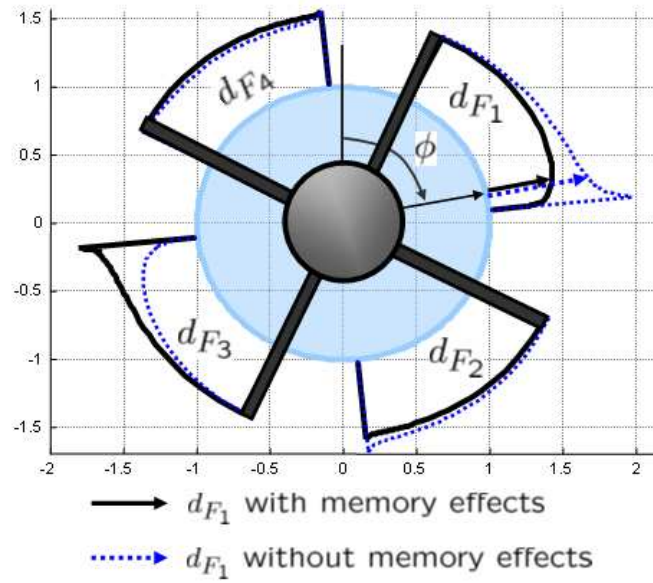


Figure 35: Schematic of variation of fin immersion depth versus roll with (solid lines) and without (dotted lines) memory effects.

Table 4: Fins-supported level turning flight.

<i>variable</i>	<i>value</i>	<i>unit</i>
ϕ	71.5055	degree
θ	0.0705	degree
ψ	0.2107	degree
V	85	m/s
Ω	0.3461 (n = 3)	rad/s
δ_T	18.5240e+3	N
δ_N	-6.9785	degree
δ_{F_1}	0.09819	degree
δ_{F_2}	0.1789	degree
δ_{F_3}	-0.1274	degree
δ_{F_4}	-0.1789	degree

resulting from the forward simulation with the considered trim controls. The behavior of the vehicle in the presence of a perturbation of the controls is again analyzed by imposing the same variation previously discussed on the elevator fins. Figure 37 compares trajectories and Euler angles variation obtained with and without perturbations, and by considering or neglecting memory effects. Again, the presence of the memory effects introduces a favorable stabilizing effect, which mitigates the onset of unstable behavior and reduces the tendency of the vehicle to deviate from the desired trajectory. For completeness, the hydrodynamic forces and moments on fins and afterbody obtained during perturbed simulations with memory effects are shown in fig. 38. The perturbation, which can be clearly observed from the time histories of forces and moments on the fins, causes a single impact of the vehicle with the cavity at about 0.19 sec.

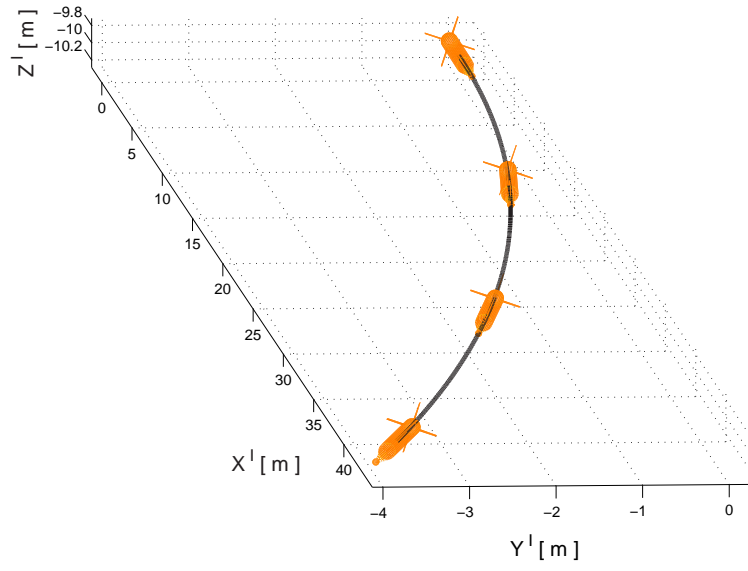
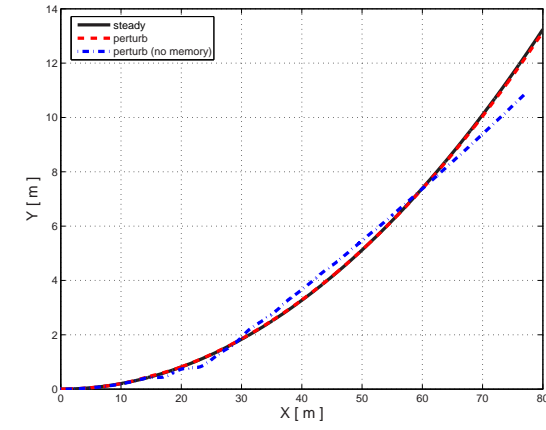
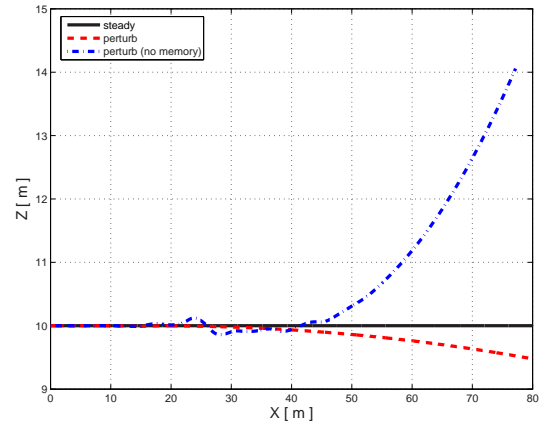


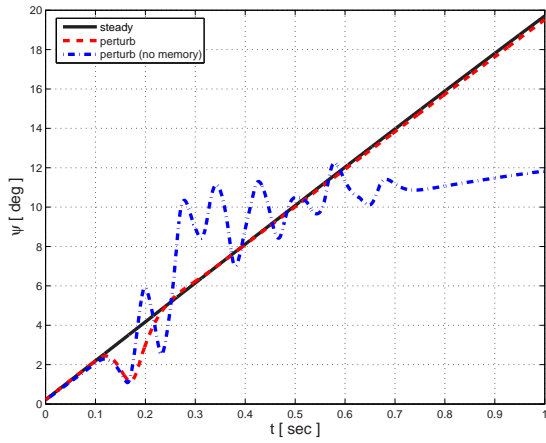
Figure 36: Trajectory of vehicle during fins-supported level turning flight.



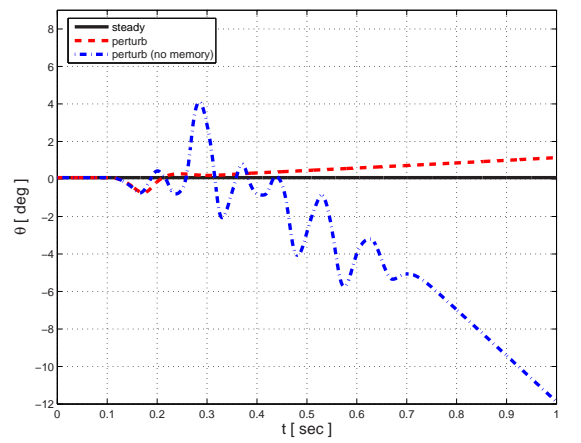
(a) Lateral displacement



(b) Vertical displacement

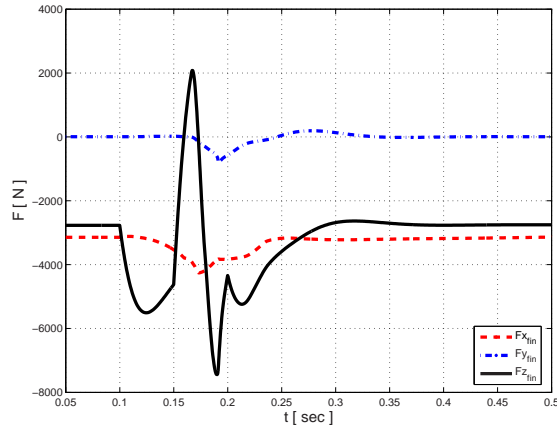


(c) Yaw angle

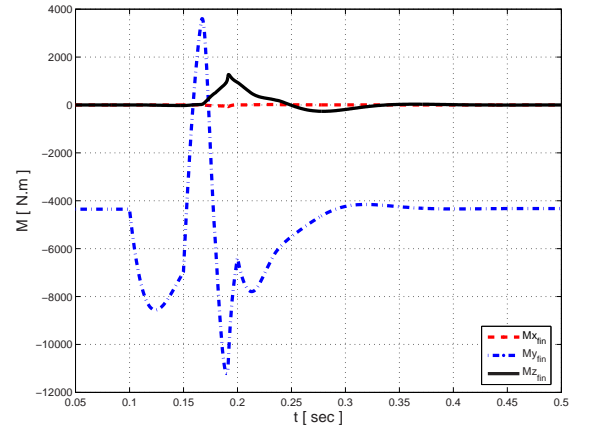


(d) Pitch angle

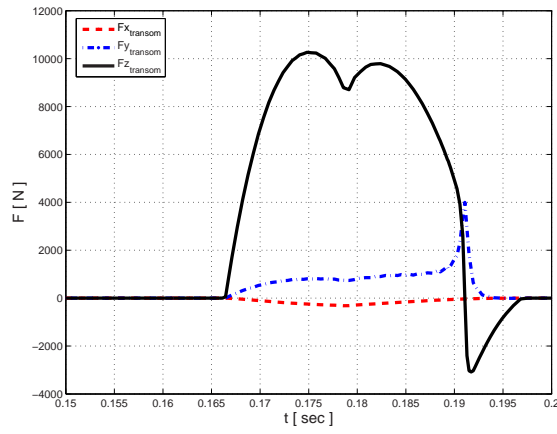
Figure 37: The comparison of trajectory of vehicle during fins-supported steady and perturbed level turning flight.



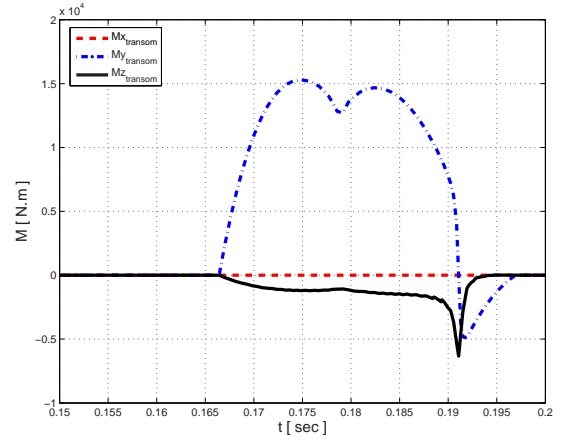
(a) Forces on the fins



(b) Moments on the fins



(c) Forces on the afterbody



(d) Moments on the afterbody

Figure 38: The hydrodynamic forces and moments applied to the fins and afterbody of the vehicle during perturbed fins-supported trimmed turning flight.

3.8 Conclusions

The flight mechanics model developed in the previous chapter is here applied to investigate trim conditions and dynamic characteristics for supercavitating vehicles. A general formulation for the trim problem is first introduced, followed by a discussion of the practical implementation used to achieve a robust trim solution. Influence of operating conditions on trim are presented for level flight and level turning flight. In addition, the influence of two cavity models as well as memory effects are also investigated to complete the discussion.

In level flight, trim controls vary with the vehicle forward velocity as a result of the decreasing fin immersion depth, while pitch angle affects the trim controls by changing the angles of attack of the control surfaces. Particularly, a sufficient pitch angle causes a dramatic variation of trim controls by causing the transition between fins-supported and fins and planing-supported flight. Dynamic simulations show that fins-supported flight appears mostly stable, while fins and planing-supported flight is characterized by an inherent instability, i.e. diverging oscillatory motion. In level turning flight, the variation of trim controls are presented for varying angular velocity, with and without memory effects. The results show the counterintuitive fact that a higher angular velocity requires a lower thrust for turning flight. In both trimmed flights, the cavity itself also influences trim conditions due to different cavity size and radial expansion rate according to the cavity models. Furthermore, the cavity memory effects significantly affect dynamic characteristics of the vehicle and introduce a favorable stabilizing effect.

In the next chapter, the trim configurations will be considered as part of an optimization problem which seeks for the optimal vehicle configuration which maximizes the trimmed performance.

Chapter IV

VEHICLE CONFIGURATIONAL OPTIMIZATION FOR PERFORMANCE IN TRIM FLIGHT

4.1 *Overview*

This chapter presents preliminary optimization studies aimed at maximizing the performance of the vehicle during trim flight. Optimal vehicle configurations are sought to maximize range in level trim flight, both in fins-supported and in fins and planing-supported configurations, and to maximize turn rate in level turning flight. The performance index considered for level flight is the traveling range of the vehicle, which defines a compromise between velocity of forward motion, payload mass and thrust. In contrast, the performance index for turning flight is the maximum turn rate, which is determined as a compromise between velocity of forward motion and load factor over the entire flight envelope. The formulation of a proper performance index in turning flight is justified through the analysis of the flight envelope for a supercavitating vehicle. The design conflicts between vehicle configurations maximizing the two performance indexes are identified and a final optimization is conducted by combining the two performance indexes.

4.2 *Formulation of The Optimization Problem*

The evaluation of the optimal vehicle configuration during flight can be formulated as an optimization problem which maximizes a relevant objective function by finding optimal values of configurational design variables. Mathematically, this optimization problem can be formulated as:

$$\begin{aligned} \max_{\mathbf{d}} \quad & C(\mathbf{d}, \mathbf{y}, \mathbf{u}), \\ \text{s.t.:} \quad & \mathbf{c}(\mathbf{d}, \mathbf{y}, \mathbf{u}) \leq 0. \end{aligned} \tag{68}$$

where $C(\mathbf{d}, \mathbf{y}, \mathbf{u})$ is the design-relevant objective function, which is subjected to a set of constraints $\mathbf{c}(\mathbf{d}, \mathbf{y}, \mathbf{u}) \leq 0$, and is a function of the configurational design variables \mathbf{d} as

well as of states and controls \mathbf{y} and \mathbf{u} . The nominal configuration described in Chapter 3 (see fig. 16 and Table 1) is used as a starting point for the design, and the vector of the considered configuration design variable is defined as:

$$\mathbf{d} = \{ d_c \quad L_{fin} \quad x_{fin} \quad R_{veh} \quad L_{veh} \quad L_{cone} \quad L_{aft} \}^T \quad (69)$$

4.3 Optimization for Straight Level Flight

4.3.1 Range as a performance index

The traveling range during trimmed flight is the objective function to be maximized. The range can be found in several ways according to the considered flight conditions. In this study, the Breguet range equation, which is based on flight at constant velocity and lift-to-drag ratio, is applied [2, 62]. If the vehicle is operating in steady level flight, then the lift-to-drag ratio is $F_L/F_D = W/\delta_T$ from force balance considerations. Assuming constant velocity, the range can be simply expressed as:

$$D = \int_{t_i}^{t_f} V dt = V(t_f - t_i) \quad (70)$$

where subscripts i and f respectively denote the initial and final time, and V is the trimmed velocity of the vehicle. The total flight time $(t_f - t_i)$ can be expressed in terms of vehicle weights at the initial and final stage W_i and W_f , specific impulse I_{sp} , and lift-to-drag ratio F_L/F_D as:

$$t_f - t_i = I_{sp} \frac{F_L}{F_D} \ln \left(\frac{W_i}{W_f} \right) \quad (71)$$

Eq. (71) is readily obtained by integrating the following relation:

$$\dot{W} = - \frac{W}{(F_L/F_D)I_{sp}} \quad (72)$$

which is found through the rate of change of the vehicle weight $\dot{W} = -\dot{m}_p g$, the momentum equation of the thrust force $\delta_T = \dot{m}_p V_{eq}$, and the expression for the specific impulse $I_{sp} = \frac{V_{eq}}{g}$, where it is assumed that the equivalent exhaust velocity V_{eq} remains constant over time. The equivalent exhaust velocity V_{eq} accounts for the pressure difference in the engine as well as the exit velocity of the jet [63, 64]. The specific impulse I_{sp} is an important

parameter measuring the efficiency of a propulsion system, which is defined as the total impulse exerted by the propellant divided by the total weight of expelled propellant during engine operation [63, 64]. Equations (70) and (71) lead to the following range equation:

$$D = V \frac{F_L}{F_D} I_{sp} \ln \left(\frac{W_i}{W_f} \right) \quad (73)$$

For simplicity, it is assumed that the mass of propellants and the weight of warhead (payload) are proportional to the total vehicle mass. Accordingly, the range in eq. (73) is an objective function which combines a number of configuration and performance related parameters through the following expression:

$$D = a_0 \frac{Vm}{\delta_T}, \quad (74)$$

where

$$a_0 = I_{sp} g \ln \left(\frac{1}{1 - r_{mp}} \right)$$

and where thrust δ_T , vehicle mass m , and propellant-to-vehicle weight ratio r_{mp} indicate the values at the initial time. The constant a_0 is an engine-specific, structure and material-related value, which is not considered to vary in terms of the set of design variables. Also, the range does not include the distances traveled before attaining trimmed velocity and after burnout. In summary, maximizing the range corresponds to minimizing the thrust force while maximizing speed and warhead weight. In the optimization problem described by eq. (68), the objective function is therefore $C = D(\mathbf{d}, \mathbf{y}, \mathbf{u})$ as defined by eq. (74).

4.3.2 Constraints

The constraints in eq. (68) are a combination of equality and inequality constraints, and are based on geometric considerations and on limitations imposed by the dimensions of the vehicle in relation to the dimensions of the cavity. The equality constraints are defined by the considered trim condition, so that the optimization constraints can be expressed as:

$$\mathbf{c}(\mathbf{d}, \mathbf{y}, \mathbf{u}) = \begin{bmatrix} \phi(\mathbf{d}, \mathbf{y}, \mathbf{u}) \\ \mathbf{g}_t(\mathbf{d}, \mathbf{y}, \mathbf{u}) \\ \mathbf{g}_d(\mathbf{d}) \end{bmatrix} \quad (75)$$

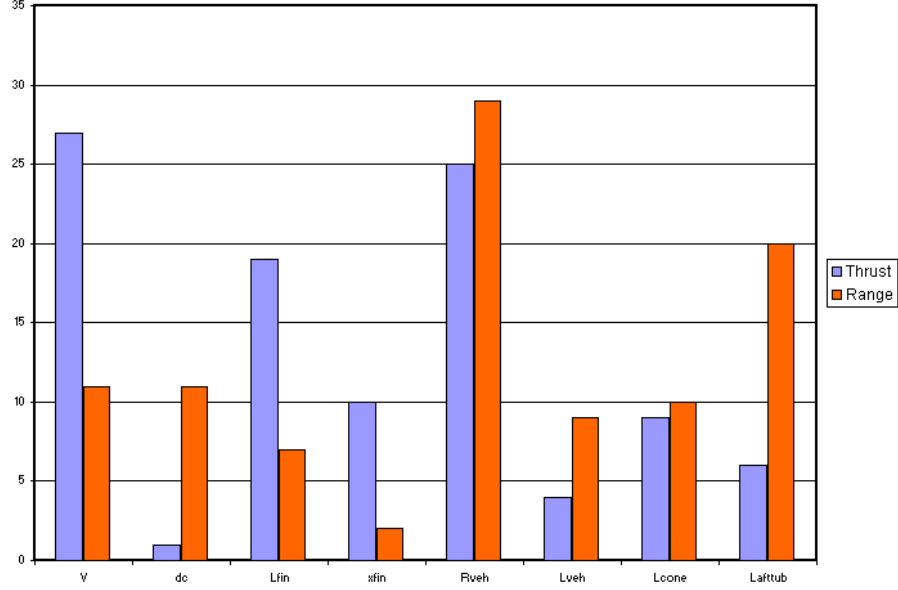


Figure 39: Effect of individual design variables on thrust and range for fins-supported level flight.

where $\phi(\mathbf{d}, \mathbf{y}, \mathbf{u})$ defines the condition for trim as expressed by eq. (53) such that

$$\phi(\mathbf{d}, \mathbf{y}, \mathbf{u}) = 0$$

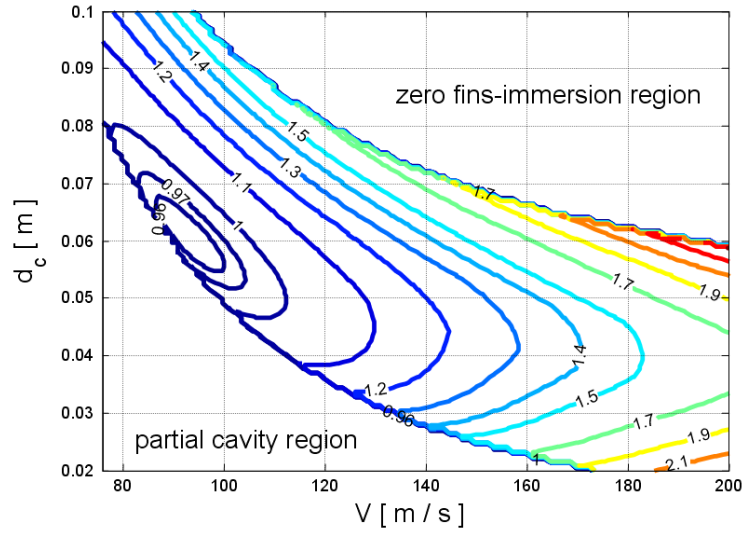
\mathbf{g}_t are cavity constraints defined in Chapter 3 (see eq.s (55), (56)), and \mathbf{g}_d are design-related constraints defining upper and lower bounds imposed to vehicle dimensions and mass:

$$\mathbf{g}_t(\mathbf{d}, \mathbf{y}, \mathbf{u}) \leq 0$$

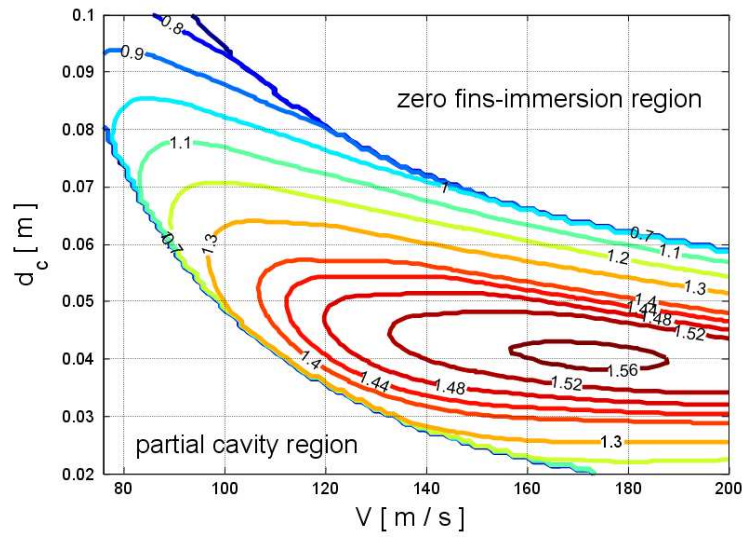
$$\mathbf{g}_d(\mathbf{d}) \leq 0$$

4.3.3 Analysis of parameters sensitivity

The interaction between cavity dimensions, control surfaces geometry, and vehicle operating conditions is complex and highly nonlinear. Figure 39 shows the effects of individual design variables and operating condition (vehicle's speed V) on range and thrust for fins-supported level flight. The plot shows how the objective function changes in terms of the variation of each design variables from its lower to upper bound. The results indicate that fin length, vehicle radius and speed exert a dominant effect on the thrust force, while design variables directly related to the vehicle weight have a more important effect on the range together with



(a) Thrust force



(b) Range

Figure 40: Variation of thrust force and range with respect to the vehicle design variables for fins-supported level flight.

vehicle's speed and cavitator diameter, which define the cavity dimension. Figures 40 (a) and (b) show for example the variation of the normalized thrust force and the normalized range in terms of cavitator diameter and vehicle velocity for fins-supported flight (both are respectively normalized by nominal values in Tables 6). In the figure, maximum and minimum values for range and thrust can be clearly identified for the proper combination of the diameter d_c and speed V .

4.3.4 Results

4.3.4.1 Preliminary optimization with reduced set of design variables

Based on the results presented in the previous section, a preliminary optimization with a reduced number of design variables (V and d_c) is carried out for the case of fins-supported flight. Results are presented in Tables 5 and 6, which respectively list optimal design variables, corresponding trim controls, and performance of the optimal configuration in comparison with that of the nominal vehicle design. The corresponding optimal values coincide with the maximum range shown in fig. 40 (b).

Table 5: Reduced optimal design configuration for fins-supported level flight.

Dimension	value	lower bound	upper bound	unit
d_c	0.0404	0.02	0.10	m
V	172.0734	76	200	m/s
	controls	value	unit	
	δ_T	25.8036e+3	N	
	δ_N	-2.1179	degree	
	δ_{F_2}	0.0765	degree	
	δ_{F_4}	-0.0765	degree	
	δ_{F_1}	0	degree	

Table 6: Performance of reduced optimal vehicle in fins-supported level flight.

	Nominal	Optimal	unit	[%]
D	638.7	999.9	m	+56.5 %
V	78	172.0734	m/s	+120.6 %
δ_T	18.3176e+3	25.8036e+3	N	+40.9 %
m	150	149.9452	kg	-0.04 %

4.3.4.2 Optimization with full set of design variables

The optimization is then performed by considering the full set of design variables. The results obtained for fins-supported, straight level flight are presented in Tables 7 and 8. The computations are based on the application of Logvinovich’s cavity model, although calculations have also been performed with Munzer-Reichardt model, whose results are omitted for the sake of brevity. Only the optimal design configurations obtained using the two models are presented to show the strong effect of cavity model on the final solution. Table 7 shows the optimal values for the design variables in comparison with lower and upper bounds considered in the optimization. It is remarkable that the results of the optimization not only include configurational design parameters, but also indications regarding the operating conditions of the vehicle, in this case identified by the velocity of forward motion V . In addition, it can be observed how the mass coincides with the imposed upper bound, which may indicate the need for additional investigations, where such bound is relaxed. Table 8 summarizes the performance of the optimized vehicle with respect to the nominal vehicle described in section 3.2. The optimization produces a remarkable improvement in performance, which translates into a 44.1% increase in velocity, a 37.5% reduction in thrust and a combined 145.9% increase in range. The comparison between optimal and nominal vehicle is shown in fig. 41 (a).

The results obtained for the case of fins and planing-supported level flight are presented in Tables 9 and 10, while the optimized vehicle configuration is presented in Fig. 41 (b). Similar improvements in performance are achieved in this configuration. Finally, fig. 42 shows the optimized configurations based on Munzer-Reichardt cavity model, which confirms the strong effect of the cavity model on the design process, and underlines the importance of correctly capturing the vehicle/cavity behavior through sufficiently accurate models.

Table 7: Optimal design configuration for fins-supported level flight.

Dimension	value	lower bound	upper bound	unit
d_c	0.0400	0.04	0.11	m
L_{fin}	0.1500	0.15	0.25	m
x_{fin}	2.2975	L_{cone}	$L_{cone} + L_{fuse}$	m
R_{veh}	0.0957	0.05	0.15	m
L_{veh}	4.0823	3.5	4.5	m
L_{cone}	0.4082	0.1 L_{veh}	0.9 L_{veh}	m
L_{aft}	0.0798	0.01 L_{veh}	0.1 L_{veh}	m
m	160.0000	140	160	kg
V	112.4102	76	120	m/s
controls		value	unit	
	δ_T	11.4524e+3	N	
	δ_N	-4.5000	degree	
	δ_{F_2}	0.2473	degree	
	δ_{F_4}	-0.2473	degree	
	δ_{F_1}	0	degree	

Table 8: Performance of optimal vehicle in fins-supported level flight.

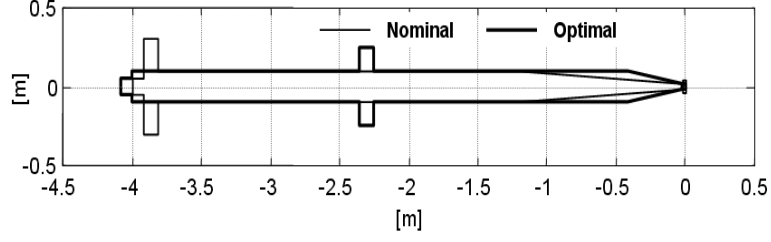
	Nominal	Optimal	unit	[%]
D	638.7	1570.5	m	+145.9 %
V	78	112.4102	m/s	+44.1 %
δ_T	18.3176e+3	11.4524e+3	N	-37.5 %
m	150	160.0	kg	+6.7 %

Table 9: Optimal design configuration for fins and planing-supported level flight.

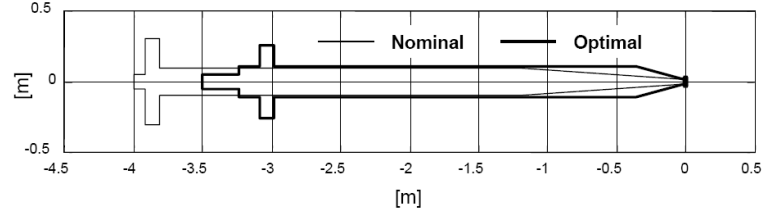
Dimension	value	lower bound	upper bound	unit
d_c	0.0684	0.04	0.11	m
L_{fin}	0.1500	0.15	0.25	m
x_{fin}	3.0857	L_{cone}	$L_{cone} + L_{fuse}$	m
R_{veh}	0.1053	0.05	0.15	m
L_{veh}	3.5156	3.5	4.5	m
L_{cone}	0.4258	0.1 L_{veh}	0.9 L_{veh}	m
L_{aft}	0.1930	0.01 L_{veh}	0.1 L_{veh}	m
m	160.0	140	160	kg
V	78.7096	76	120	m/s
controls		value	unit	
	δ_T	1.240e+4	N	
	δ_N	-4.5000	degree	
	δ_{F_2}	0.2473	degree	
	δ_{F_4}	-0.2473	degree	
	δ_{F_1}	0	degree	

Table 10: Performance of optimal vehicle in fins and planing-supported level flight.

	Nominal	Optimal	unit	[%]
D	625	1021	m	+63 %
V	78	79	m/s	+1.2 %
δ_T	1.871e+4	1.240e+4	N	-34 %
m	150	160	kg	+6.7 %

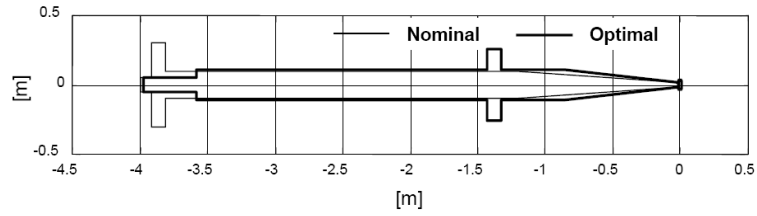


(a) Fins-supported flight

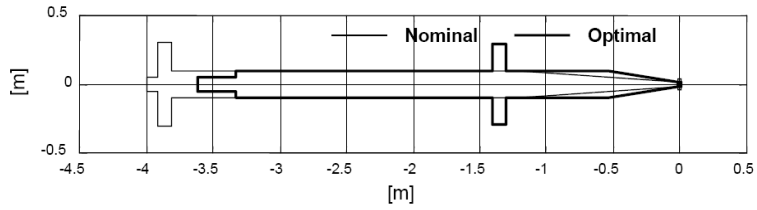


(b) Fins and planing-supported flight

Figure 41: Optimal configurations of supercavitating vehicles based on the Logvinovich's cavity model.



(a) Fins-supported flight



(b) Fins and planing-supported flight

Figure 42: Optimal configurations of supercavitating vehicles based on the Munzer-Reichardt's cavity model.

4.4 Optimization for Level Turning Flight

4.4.1 Turn rate and load factor

In supercavitating vehicles, the cavitator provides a significant contribution to the total lift. For a vehicle with a one d.o.f. cavitator, as assumed here, the centripetal force required for turning can only be achieved through a proper roll angle. The turning maneuvers achievable by the considered vehicle configuration therefore belong to the family of banked and coordinated turns. In a coordinated turn, the turning performance can be quantified in terms of vehicle velocity V and load factor n , which are related by the linear and angular momentum balance equation (eq. (1)). The load factor n is defined as the total lift, provided by cavitator and fins, divided by the vehicle weight. For level coordinated turning flight with non-zero Euler angles, the turn rate Ω (angular velocity about the vertical inertial axis i_3) and turn radius R can be expressed with respect to velocity and load factor as follows:

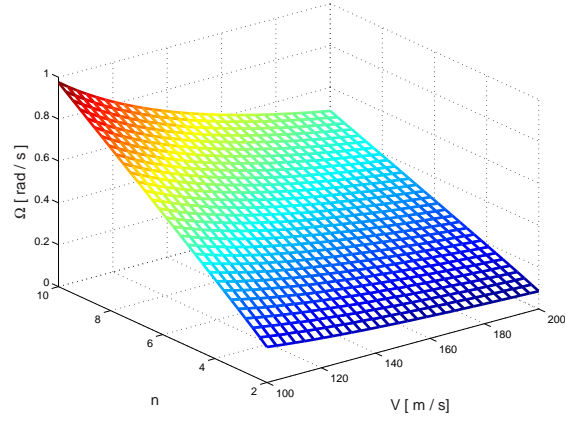
$$\begin{aligned}\Omega &= \frac{g}{V} \left(\frac{\cos \theta \sin \theta \sin \psi + \sqrt{(n^2 - 1)(1 - \cos^2 \theta \sin^2 \psi) + \sin^2 \theta}}{\sin^2 \theta + \cos^2 \theta \cos^2 \psi} \right) \\ R &= \frac{V^2}{g} \left(\frac{\sin^2 \theta + \cos^2 \theta \cos^2 \psi}{\cos \theta \sin \theta \sin \psi + \sqrt{(n^2 - 1)(1 - \cos^2 \theta \sin^2 \psi) + \sin^2 \theta}} \right)\end{aligned}\quad (76)$$

which yields the following relationship between load factor n and roll angle ϕ :

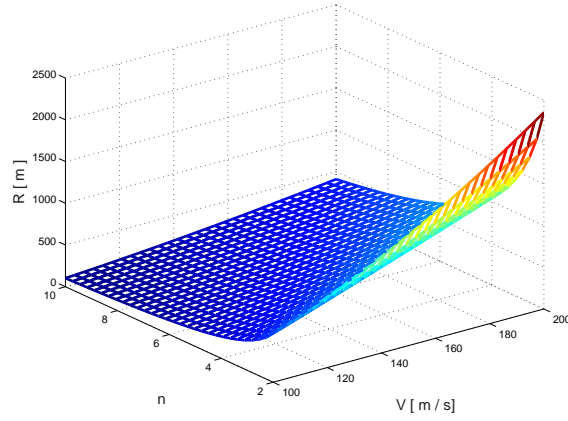
$$\begin{aligned}n &= \frac{1}{\cos \phi} \left(\frac{\cos \theta}{1 + \tan \phi \sin \theta \tan \psi} \right) \\ \phi &= \sin^{-1} \left(\frac{\cos \psi \left(\cos \theta \sin \theta \sin \psi + \sqrt{(n^2 - 1)(1 - \cos^2 \theta \sin^2 \psi) + \sin^2 \theta} \right)}{n(\sin^2 \theta + \cos^2 \theta \cos^2 \psi)} \right) \\ &= \tan^{-1} \left(\frac{V\Omega}{g} \cos \psi / \left(\cos \theta - \frac{V\Omega}{g} \sin \theta \sin \psi \right) \right)\end{aligned}\quad (77)$$

If one considers $\theta = \psi = 0$, then, eq. (76) and (77) are reduced to familiar forms for a simple bank turn:

$$\begin{aligned}\Omega &= \frac{g\sqrt{n^2 - 1}}{V} \\ R &= \frac{V^2}{g\sqrt{n^2 - 1}} \\ \phi &= \cos^{-1} \left(\frac{1}{n} \right)\end{aligned}\quad (78)$$



(a) Turn rate



(b) Turn radius

Figure 43: Variation of turn rate and radius in terms of speed and load factor.

A finite amount of pitch and yaw are however required for the coordinated turn of a supercavitating vehicle because the asymmetric fin immersion produces asymmetric fin forces and moments. Fig. 43 (a)-(b) show how the turn rate and turn radius vary with vehicle velocity and load factor. Also, fig. 44 illustrates the discrepancy between roll angles evaluated according to eq. (78) for a simple bank turn, and eq. (77) for a coordinated turn with pitch and yaw. The small difference between the two values shows that in the considered configuration, the turns can be approximated as simple bank turns, and therefore that, based on eq. (78), maximizing the turn rate Ω corresponds to maximizing the load factor while minimizing the vehicle velocity.

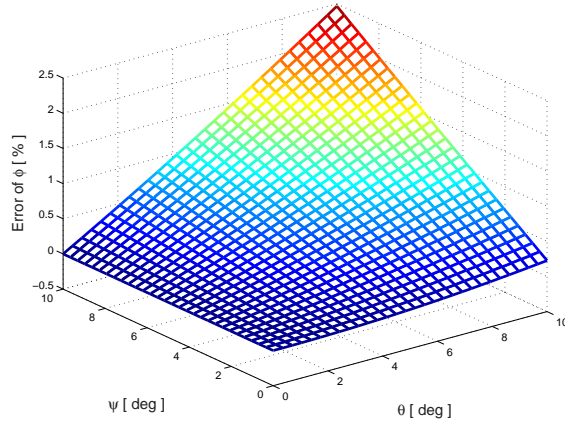


Figure 44: Difference between roll angles predicted from eq. (77) and eq. (78) at $V = 85$ m/s, $n = 5$).

4.4.2 Flight envelope limitations

In conventional aircraft, the load factor is restricted by available engine thrust and structural design limitations, while the minimum velocity is generally limited by aerodynamic stall. Figure 45 shows for reference purposes the flight envelope of a conventional missile (a rocket-propelled medium-range missile based on the AIM-7 Sparrow [2]).

In supercavitating vehicles, the turn performance is dominated by constraints on hydrodynamic forces and moments as well as on supercavity dimensions, which cause their flight envelope to be significantly different from that of conventional vehicles. The main contributors to the flight envelope of a supercavitating vehicle are discussed in what follows.

4.4.2.1 Thrust

When a conventional vehicle operates in turning flight, it requires larger lift than in level flight in order to produce sufficient centripetal force. As a result, the vehicle is also subject to a larger drag. Therefore maximum available thrust is a limiting factor for turning flight. For a supercavitating vehicle, maximum available thrust imposes limits on the velocity in straight level flight as a result of the increase of the required thrust with the vehicle velocity. In contrast, in level turning flight, thrust decreases with the load factor as shown in fig. 46, which is due to reduction in cavitator drag as its angle of attack increases (see eq. (25)). This behavior is clearly demonstrated in fig. 47, which compares the hydrodynamic coefficients

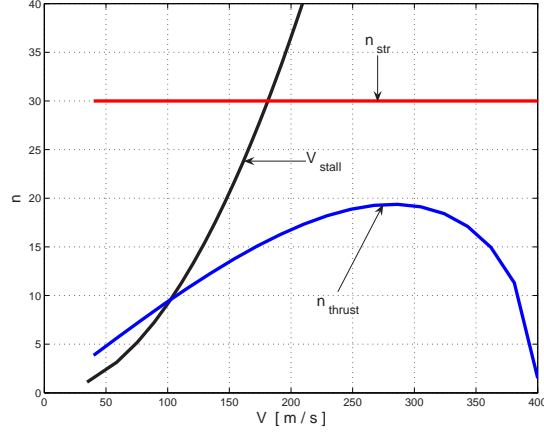


Figure 45: V-n diagram for a rocket-propelled medium-range missile based on the AIM-7 Sparrow [2].

of the nose-cavity interactions with conventional aerodynamic coefficients.

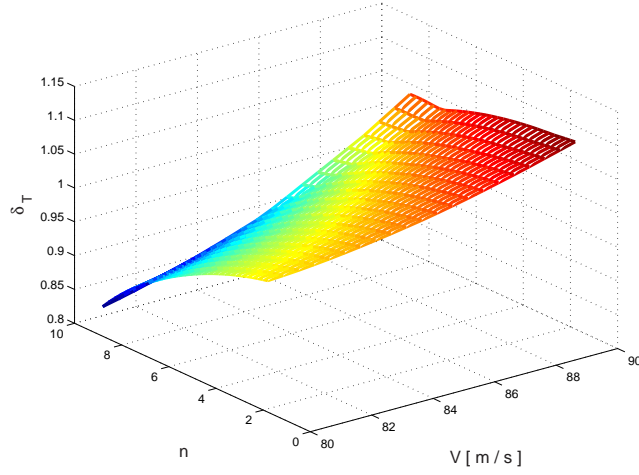
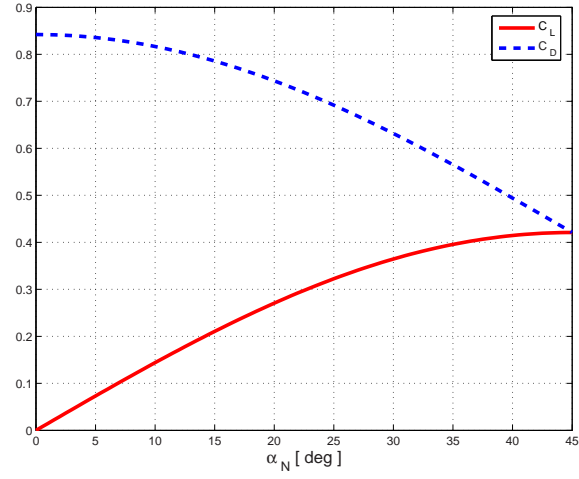


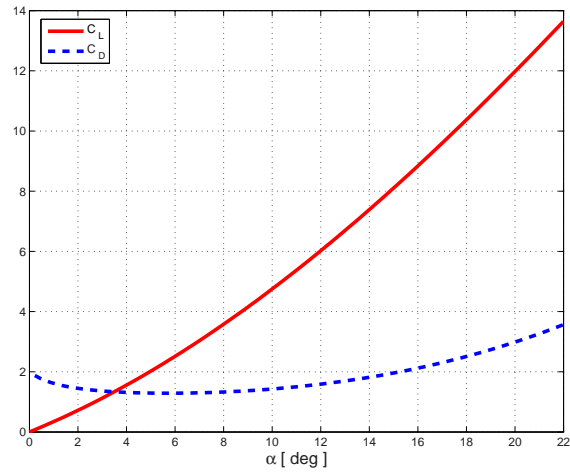
Figure 46: The variation of thrust with respect to the velocity and load factor for level turning flight of the nominal supercavitating vehicle (thrust normalized by nominal value 18.3176 kN).

4.4.2.2 Structural integrity

Structural considerations also impose limitations on the load factor. The maximum bending moment on the vehicle body is limited by considering the same maximum load factor used in missiles $n_{str} = 30$. In addition, the bending moment at the fins' roots varies in terms of immersion depth, vehicle velocity and turn rate. Its variation in terms of load factor and



(a) Hydrodynamic coefficients of the cavitator



(b) Aerodynamic coefficient of a missile

Figure 47: Lift and drag coefficients for the cavitator of a supercavitating vehicle and for a conventional missile (a rocket-propelled medium-range missile based on the AIM-7 Sparrow).

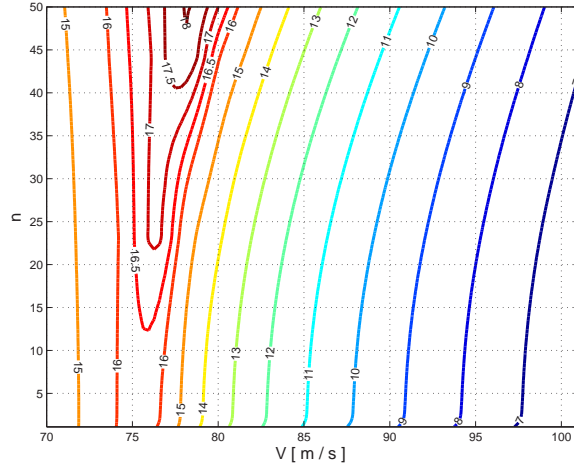


Figure 48: The variation of bending moment on the fin's root with respect to the velocity and load factor (moment is normalized by the vehicle weight).

vehicle velocity is shown in fig. 48. The contours show that the bending moment reaches its maximum values for a narrow velocity range, approximately centered at 77 m/s.

4.4.2.3 Hydrodynamics

Finally, the turn performance of a supercavitating vehicle is limited by supercavity-related constraints. First, minimum and maximum velocities are defined by the hydrodynamic stall of the cavitator and fins respectively. In addition, the minimum velocity of the vehicle is limited by the transition between partial and fully-developed supercavity. Next, the vehicle must have sufficiently immersed fins to sustain trim flight and maneuvering flight. Finally, it is desirable for the vehicle to avoid planing during turning flight. Without a suitable control scheme, planing forces cause oscillatory motion of the vehicle during steady level turning flight as described in Chapter 3. Furthermore, if the vehicle performs turning flight from fins-supported level flight, a suitable control scheme is required to manage the onset of planing and discontinuous slope of fin angles. Also turning from a fins and planing-supported level flight causes the planing region to vary with roll angle, which must be accounted for during the transition. These supercavity-related constraints affect turn performance as well as flight envelope.

At assigned load factor for turning flight, the minimum velocity is defined by the maximum lift coefficient (C_L) associated with the stall of the cavitator, while the maximum velocity is limited by the stall of the fins. Minimum and maximum velocities can be derived from forces and moment equilibrium as:

$$\begin{aligned} L^{\mathcal{B}} &= - \left(\mathbf{s}_N^{\mathcal{B}} + \sum \mathbf{s}_{F_i}^{\mathcal{B}} \right) \cdot \mathbf{b}_3 = nW \\ x_{cm} \mathbf{s}_N^{\mathcal{B}} \cdot \mathbf{b}_3 &= (x_{fin} - x_{cm}) \sum \mathbf{s}_{F_i}^{\mathcal{B}} \cdot \mathbf{b}_3 + \sum \mathbf{m}_{F_i}^{\mathcal{B}} \cdot \mathbf{b}_2 \end{aligned} \quad (79)$$

where $L^{\mathcal{B}}$ is the magnitude of the total lift by cavitator and fins, and $\mathbf{m}_{F_i}^{\mathcal{B}} \cdot \mathbf{b}_2$ is the pitch moment of the i -th fin about the vehicle cross-sectional center at the fin's root. Also, x_{cm} and x_{fin} respectively denote distances of the vehicle center of mass and the fin's root from the nose. Minimum and maximum velocities imposed by stall are obtained when lift coefficients reach maximum values, i.e. $\mathbf{s}_N^{\mathcal{B}} \cdot \mathbf{b}_3 = (\mathbf{s}_N^{\mathcal{B}} \cdot \mathbf{b}_3)_{max}$ and $\mathbf{s}_{F_i}^{\mathcal{B}} \cdot \mathbf{b}_3 = (\mathbf{s}_{F_i}^{\mathcal{B}} \cdot \mathbf{b}_3)_{max}$. The corresponding load factor limits are:

$$\begin{aligned} n_{cav} &= \frac{1}{W(x_{fin} - x_{cm})} \left(x_{fin} \mathbf{s}_N^{\mathcal{B}} \cdot \mathbf{b}_3 - \sum \mathbf{m}_{F_i}^{\mathcal{B}} \cdot \mathbf{b}_2 \right) \\ n_{fin} &= \frac{1}{Wx_{cm}} \left(x_{fin} \sum \mathbf{s}_{F_i}^{\mathcal{B}} \cdot \mathbf{b}_3 + \sum \mathbf{m}_{F_i}^{\mathcal{B}} \cdot \mathbf{b}_2 \right) \end{aligned} \quad (80)$$

At low velocity, the stall velocity of the cavitator determines the maximum load factor because the fin's lift is much larger than that of the cavitator due to the correspondingly large fin immersion depth. On the contrary, at high velocity, the situation is reversed.

Equation (80) contains general forms which can be applied to all flight conditions. The simplified expression presented below are instead useful to better understand how design variables of the vehicle affect turn performance. For the case of zero pitch and yaw angle in eq. (76), and assuming that $\mathbf{m}_{F_i}^{\mathcal{B}} \cdot \mathbf{b}_2$ is relatively small compared to $\mathbf{s}_{F_i}^{\mathcal{B}} \cdot \mathbf{b}_3$ and that the maximum lift of the cavitator and fins are respectively limited by the maximum cavitator angle α_{Nmax} and maximum fin's angle $\gamma_{F_i max}$, yields the following expressions for the load

factors:

$$\begin{aligned}
n_{cav} &= \frac{\rho_w v_N^2 A_N C_d(\sigma, 0) \sin(2\alpha_N)}{4W(x_{fin} - x_{cm})/x_{fin}} \\
n_{fin} &= S_{fin}^2 \left(\sin(\phi) \left[\frac{1}{2} \rho_w v_{F_2}^2 C_z(\gamma_{F_2}, d_{F_2}) + \frac{1}{2} \rho_w v_{F_4}^2 C_z(\gamma_{F_4}, d_{F_4}) \right] \right. \\
&\quad \left. - \cos(\phi) \left[\frac{1}{2} \rho_w v_{F_1}^2 C_z(\gamma_{F_1}, d_{F_1}) + \frac{1}{2} \rho_w v_{F_3}^2 C_z(\gamma_{F_3}, d_{F_3}) \right] \right) / (W x_{cm} / x_{fin}) \quad (81)
\end{aligned}$$

Partial cavity conditions may be considered as an inherent flight mode of supercavitating vehicles particularly at launch and/or water entry. For simplicity, this study focuses on operation with a fully-developed supercavity. This imposes another limiting constraint on the vehicle velocity, which largely depends on the cavitation number and the cavitator's dimension. For both straight level flight and level turning flight, sufficient fin's hydrodynamic forces are required for lift when the vehicle does not exploit planing. As a result, the sufficient fin immersion depth imposes limitation on velocity. Finally, the fins-supported flight scheme without planing imposes a limit on the load factor particular at low speed. When the vehicle performs a turn, the cavity centerline has a curvature which causes the center of the cavity cross section at the afterbody to deviate from the center of the vehicle cross section. This discrepancy can produce planing flight as well as asymmetric fin immersion depth particularly when the vehicle performs a rapid turn.

4.4.3 V-n diagram

All the constraints discussed above are summarized in the V-n diagram of fig. 49, which represents the flight envelope of the nominal supercavitating vehicle described in Table 1. The diagram is clearly more complex than the one for a conventional missile (see fig. 45). In the figure, area 1 and 2 respectively correspond to the partial cavity and the planing regions in which the vehicle is assumed not to operate. Areas 4, 5, 6 and 7 define regions where at least one fin is not immersed into the cavity boundary and hence has zero control effectiveness (4 - one fin, 5 - two fins, 6 - three fins, and 7 - four fins). Consequently, area 3 represents the possible fins-supported flight zone, which is limited by the geometry and dimensions of the vehicle in relation to the dimensions of the cavity. Boundaries a and b are respectively the minimum velocity imposed by the stall of the cavitator and

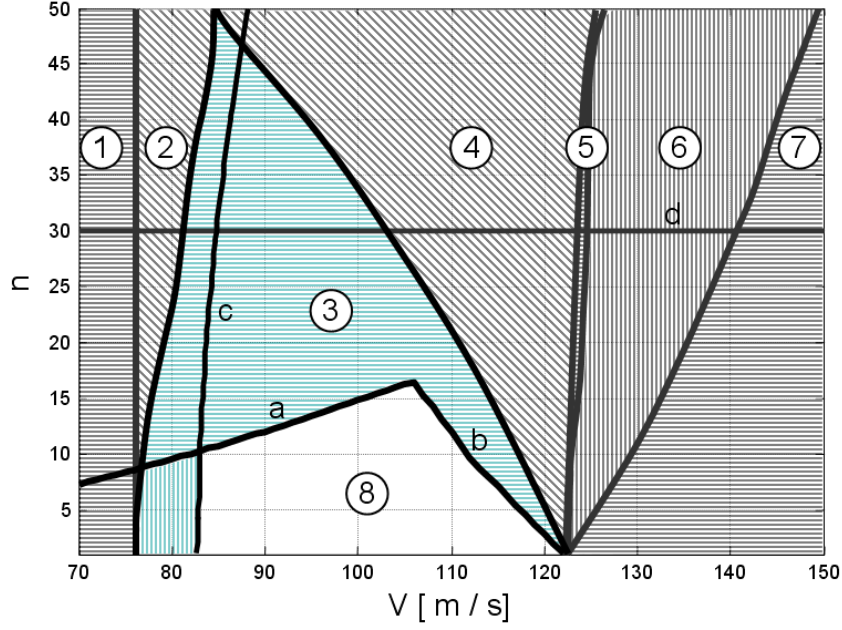


Figure 49: V-n diagram of the nominal supercavitating vehicle based on hydrodynamics but neglecting aerodynamics inside a cavity.

the maximum velocity defined by the stall of the fins. It should be noted that the latter imposes a maximum velocity limit, instead of minimum velocity due to the decrease of the fin immersion depth for increasing velocity and load factor. Experimental data show that the lift coefficient for the cavitator increases until about $\alpha_{N \max} = 60^\circ$ and it decreases after that peak angle [53] (see fig. 47). However, in this study, $\alpha_{N \max} = 30^\circ$ is considered as a maximum angle for the cavitator in eq. (25). Also, the maximum angle of the fins is assumed to be $\gamma_{F_i \max} = 30^\circ$. Furthermore, the boundary d is the maximum load factor selected as representative of the structural integrity of the vehicle body, and the boundary c represents the minimum velocity imposed by the structural integrity of elevator fins, which is identified by a normalized moment (with respect to the vehicle weight) at the fin's root (allowable normalized bending moment of $c = 12$). The remaining area 8 indicates the possible flight region for the supercavitating vehicle during level turning flight.

In the V-n diagram, the point at the intersection between boundaries a and b is denoted as “maneuver point”, and the corresponding velocity is the “corner velocity”. At this point,

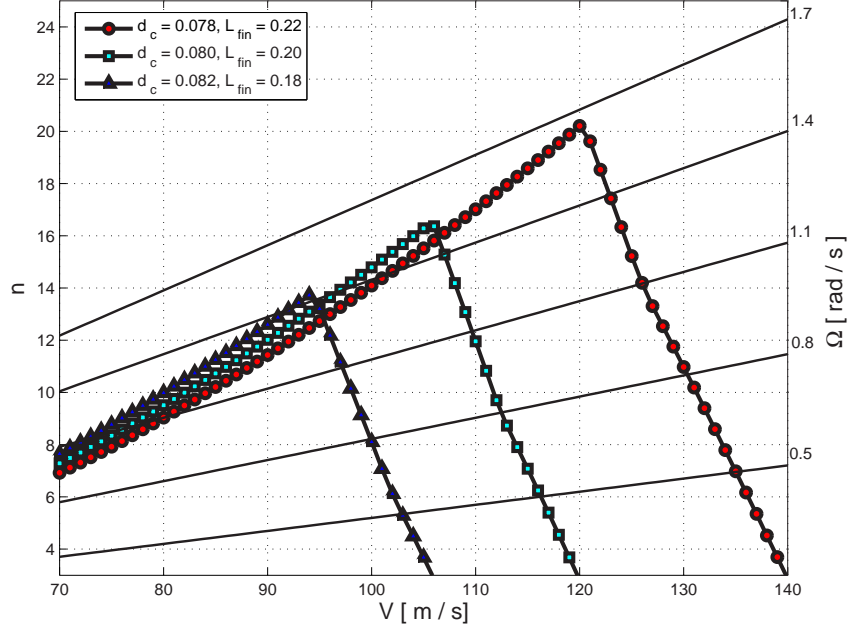


Figure 50: The variation of V-n diagram with respect to the cavitator diameter and fin span length when $\alpha_{N \max} = 30^\circ$ and $\gamma_{F_i \max} = 30^\circ$ (the contour lines denote constant turn rates).

the supercavitating vehicle can simultaneously achieve maximum turn rate and minimum turn radius. Maximum turn rate or minimum turn radius can be achieved by increasing the load factor imposed by the cavitator's stall and fin's stall. The load factor for the stall of the cavitator (n_{cav}) can be extended by increasing the cavitator diameter and/or by reducing the restrictions on the maximum stall angle by placing the vehicle center of mass backward. Also, it can be extended by decreasing the vehicle weight (see eq. (81)). The limit defined by the stall of the fins (n_{fin}) can be extended by increasing the fin span length, by placing the vehicle center of mass forward, and by decreasing the vehicle weight (see eq. (81)). Fig 50 shows how the stall velocities of the cavitator and the fins vary with the cavitator diameter and the fin span length. It should be noted that the limitation on the allowable maximum moment at the fin's root introduces trade-offs with the fin's stall velocity due to the strong dependency on the fin span.

4.4.4 Considered performance index

The maximum turn rate Ω for steady turning flight is considered as the objective function to be maximized. In this operating condition, maximum turn rate and minimum turn radius (eq. (76)) are important performance characteristics. As mentioned earlier, the maximum turn rate and minimum turn radius can be simultaneously obtained at the maneuver point (at the corner speed) in the V-n diagram. The maximum turn rate Ω at the corner speed is considered as the objective of the optimization to follow. Its expression is obtained by letting $V = V_{corner}$ in eq. (76) to obtain:

$$\Omega = \frac{g}{V_{corner}} \left(\frac{\cos \theta \sin \theta \sin \psi + \sqrt{(n^2 - 1) (1 - \cos^2 \theta \sin^2 \psi) + \sin^2 \theta}}{\sin^2 \theta + \cos^2 \theta \cos^2 \psi} \right) \quad (82)$$

4.4.5 Constraints

For the fins-supported level turning flight problem, \mathbf{g}_t in eq. (75) is defined as in eq. (59). In eq. (59), the first inequality constraint defines the region 1 related to partial cavitation in the V-n diagram of fig. 49, the second constraint corresponds to regions 4, 5, 6, and 7, and the third condition is related to planing (region 2). The last two conditions correspond to boundaries a and b related to the stall of the control surfaces, while the design-related constraints \mathbf{g}_d include the constraints associated with structural integrity which can be expressed as:

$$\begin{aligned} g_{d\ 1} &= n - n_{str} \\ g_{d\ 2} &= (V_{min})_c - V \end{aligned} \quad (83)$$

which respectively express the limitation on the bending moment on the vehicle body (boundary d), and the boundary c in the V-n diagram.

4.4.6 Implementation of optimization procedure

In general, the optimization procedure of eq. (68) is a straightforward approach producing efficient solutions for well-defined problems such as those with quadratic objective and linear constraints. However, if the constraints are affected by numerical noise and they

are active during the optimization iterations, the problem may produce non-optimal results or be infeasible. In practice, the constraints behave as uncertain parameters, and may require proper handling such as the reduction of the feasible region and/or probabilistic analyses [65].

In this case, the trim process developed in Chapter 3 provides a primary constraint. Although the trim solver is accurate and numerically well-behaved inside the feasible design space, finding a solution on the boundary between the feasible and infeasible design space can be time-consuming and sensitive to the initial guess for trim states. Unfortunately, in the optimization problem which seeks for the maximum turn rate over the entire flight envelope, the maximum value of the objective function will be achieved at such constraint boundary, i.e. at the corner speed. Therefore the direct application of the optimization procedure of eq. (68) to the maximum turn rate case is affected by noisy constraints. In contrast, in the maximum range case, the trim solver searches for solutions well inside the feasible design space (as shown in fig. 40 (b)). Consequently, the procedure of eq. (68) with the design variables V, \mathbf{d} produces solutions in a stable and efficient way.

As a practical alternative, a multi-level optimization procedure using hydrodynamic forces and moment balance equation described in the previous section is employed. The hydrodynamic forces and moment balance equation replaces the trim solver in a lower-level optimization, which is nested inside the system-level optimization. The lower-level optimization finds the best operating conditions (V and n at maneuver point) for each assigned design variables \mathbf{d} from the system-level optimization. This methodology is highly dependent on the approximate formula based on hydrodynamic forces and moment balance equation, which has shown to produce very stable and reliable solutions.

4.4.7 Parameters sensitivity

Figure 51 shows the effects of the individual design variables on the maximum turn rate, and compares them with their effects on thrust and range in steady level flight. These results differ from the ones presented in fig. 39 as they are obtained for velocity V assigned as the optimal value in level flight (see Table 7). For turning flight, velocity V and load factor n

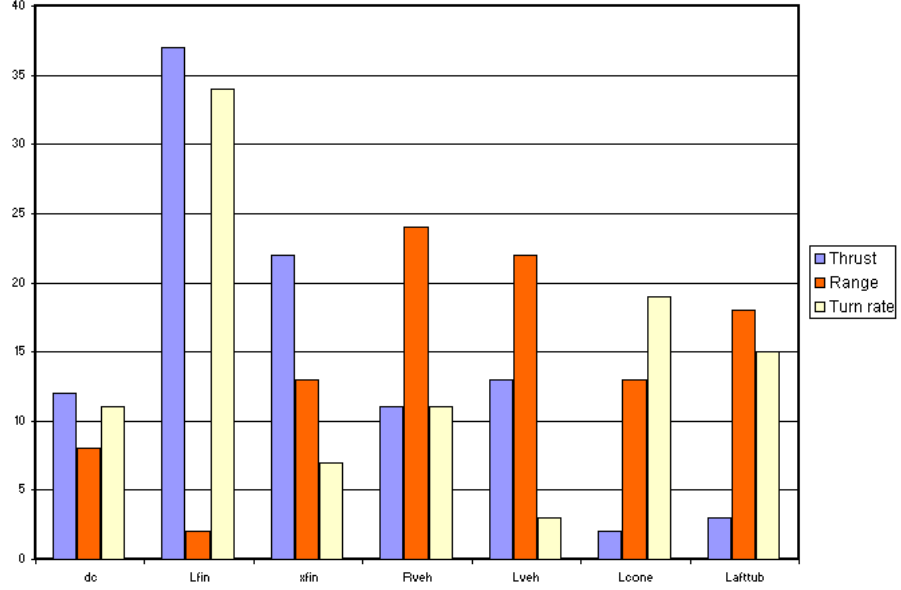


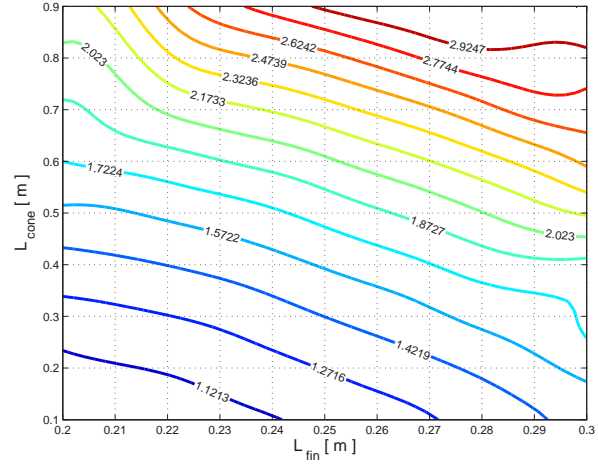
Figure 51: Effect of individual design variables on thrust, range, and maximum turn rate for fins-supported level flight.

correspond to the maneuver point defined by the corner speed. The two most dominant design variables are the fin span, which is closely related to the control authority of the fins, and, surprisingly, the vehicle cone length. The variation of maximum turn rate in terms of fin span and cone length presented in fig. 52 (a) shows an approximately linear relation: the maximum turn rate increases almost monotonically with the two design variables. This suggests that a cone-shaped vehicle with long fin span may be capable of more aggressive turns. Figure 52 (b) shows the variation of turn rate with respect to cavitator diameter and fin length when all other design variables are fixed at the nominal values. As one might expect, the maximum turn rate increases with the dimensions of both control surfaces. It is also interesting to observe that for relatively long fin span ($L_{fin} > 0.25$), and small cavitator diameter, the maximum turn rate depends only on the cavitator diameter.

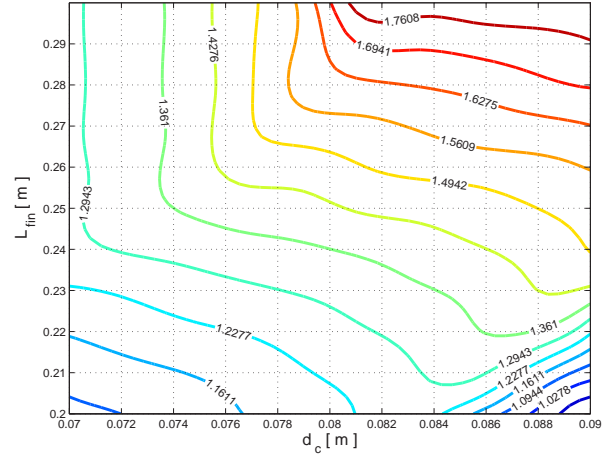
4.4.8 Results

4.4.8.1 Preliminary optimization with reduced set of design variables

A preliminary optimization is carried out by considering only d_c and L_{fin} as design variables. The results presented in Tables 11 and 12, identify the maximum value for the turn rate



(a) Fin span length and cone length



(b) Cavitator diameter and fin span length

Figure 52: Variation of maximum turn rate in terms of selected design variables.

Table 11: Reduced optimal design configuration for fins-supported level turning flight.

Dimension	value	lower bound	upper bound	unit
d_c	0.09	0.07	0.09	m
L_{fin}	0.30	0.20	0.30	m
m	150.6048	140	160	kg
V	101.8298	80	120	m/s
n	19.2256	1	30	

Table 12: Performance of reduced optimal vehicle in fins-supported level turning flight.

	Nominal	Optimal	unit	[%]
Ω	1.2106	1.8512	rad/s	52.9%
V	83.2364	101.8298	m/s	22.3%
n	10.3257	19.2256		86.2%
δ_T	15.2520e+3	28.1745e+3	N	84.7%

in fig. 52 (b). The vehicle with these optimal dimensions of control surfaces produces a considerable improvement (52.9%) in maximum turn rate, which is achieved by increasing vehicle velocity and thrust and a correspondingly higher load factor.

4.4.8.2 Optimization with full set of design variables

The results obtained with the full set of design variables are presented in Tables 13 and 14. The optimization increases the fin's span as in the reduced optimization case, but reduces the cavitator's diameter. In addition, the mass coincides with the imposed lower bound, which shows the opposite tendency to the case of maximum range. Table 14 summarizes the performance of the optimized vehicle with respect to the nominal vehicle. The remarkable improvement in turn rate performance is obtained at the expense of higher thrust and load factor which translates into a 148.9% increase in maximum turn rate and a 160.9% increase in load factor. The comparison between optimal and nominal vehicle is shown in fig. 53, in which the thick outline depicts the optimal configuration of the vehicle. This optimized configuration shows little similarity with the optimized configurations based on maximum range (see fig. 41), and it is interesting to note a vague resemblance to existing cone-shape designs for supercavitating vehicles and the Soviet torpedo Shkval shown in fig. 54

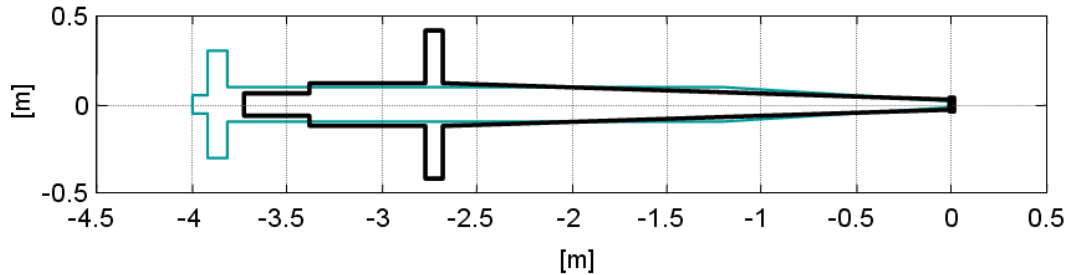


Figure 53: Optimal configurations of supercavitating vehicles based on maximum turn rate during fins-supported level turning flight.

Table 13: Optimal design configuration for fins-supported level turning flight.

Dimension	value	lower bound	upper bound	unit
d_c	0.0769	0.07	0.09	m
L_{fin}	0.3000	0.20	0.30	m
x_{fin}	2.7327	L_{cone}	$L_{cone} + L_{fuse}$	m
R_{veh}	0.1256	0.05	0.15	m
L_{veh}	3.7348	3.5	4.5	m
L_{cone}	2.6695	0.1 L_{veh}	0.9 L_{veh}	m
L_{aft}	0.3523	0.01 L_{veh}	0.1 L_{veh}	m
m	140.0	140	160	kg
V	87.6658	76	120	m/s
n	26.9428	1	30	
controls		value	unit	
	V	87.6658	m/s	
	Ω	3.0134	rad/s	
	ϕ	87.7838	degree	
	θ	0.1046	degree	
	ψ	2.7020	degree	
	δ_T	26.5419e+3	N	
	δ_N	-20.6597	degree	
	δ_{F_2}	0.1789	degree	
	δ_{F_4}	-0.1789	degree	
	δ_{F_1}	0.0133	degree	
	δ_{F_3}	-0.0453	degree	

Table 14: Performance of optimal vehicle in fins-supported level turning flight.

	Nominal	Optimal	unit	[%]
Ω	1.2106	3.0134	rad/s	148.9%
V	83.2364	87.6658	m/s	5.3%
n	10.3257	26.9428		160.9%
δ_T	15.2520e+3	26.5419e+3	N	74.0%



Figure 54: Configuration of the existing supercavitating vehicle Shkval [3].

4.5 Optimization Based on A Combined Performance Index

4.5.1 Objective function

In this section, a combined performance index including maximum range and turn rate is considered as an objective for fins-supported flight. The corresponding objective function is defined as:

$$C(\mathbf{d}, \mathbf{y}, \mathbf{u}) = w_1 \bar{D} + w_2 \bar{\Omega} \quad (84)$$

where $\bar{D}, \bar{\Omega}$ are values for range and turn rate, normalized with respect to the ones corresponding to the nominal vehicle, while w_i ($i = 1, 2$) are the optimization weights. The weights are arbitrarily selected as $w_1 = w_2 = 0.5$.

4.5.2 Implementation of optimization procedure

The optimization procedure is formulated to include the two considered trim conditions, i.e. level and turning flight, and the objective function defined above. Mathematically, the optimization procedure is formulated as follows:

$$\max_{\mathbf{d}} \quad C(\mathbf{d}, \hat{\mathbf{y}}, \hat{\mathbf{u}}), \quad (85)$$

$$\text{s.t.:} \quad \mathbf{c}(\mathbf{d}, \hat{\mathbf{y}}, \hat{\mathbf{u}}) \leq 0. \quad (86)$$

where $\hat{\mathbf{y}}, \hat{\mathbf{u}}$ are vectors containing states and controls corresponding to the considered trim configurations, while $\mathbf{c}(\mathbf{d}, \hat{\mathbf{y}}, \hat{\mathbf{u}})$ defines an array of equality and inequality constraints which

define design and operational constraints:

$$\mathbf{c}(\mathbf{d}, \hat{\mathbf{y}}, \hat{\mathbf{u}}) = \begin{bmatrix} \phi(\mathbf{d}, \hat{\mathbf{y}}, \hat{\mathbf{u}}) \\ \mathbf{g}_t(\mathbf{d}, \hat{\mathbf{y}}, \hat{\mathbf{u}}) \\ \mathbf{g}_d(\mathbf{d}) \end{bmatrix} \quad (87)$$

The operational constraints ϕ include the two trim conditions and can be expressed as follows:

$$\phi(\mathbf{d}, \hat{\mathbf{y}}, \hat{\mathbf{u}}) = \begin{bmatrix} \phi_S(\mathbf{d}, \mathbf{y}_S, \mathbf{u}_S) = 0 \\ \phi_T(\mathbf{d}, \mathbf{y}_T, \mathbf{u}_T) = 0 \end{bmatrix} \quad (88)$$

where $\phi_S(\mathbf{d}, \mathbf{y}_S, \mathbf{u}_S) = 0$, $\phi_T(\mathbf{d}, \mathbf{y}_T, \mathbf{u}_T) = 0$ respectively define the level flight and turning trim problems, while $\mathbf{y}_S, \mathbf{u}_S$ and $\mathbf{y}_T, \mathbf{u}_T$ are the corresponding state and control vectors.

Accordingly, in eq. (86):

$$\hat{\mathbf{y}} = \begin{bmatrix} \mathbf{y}_S^T & \mathbf{y}_T^T \end{bmatrix}^T$$

and

$$\hat{\mathbf{u}} = \begin{bmatrix} \mathbf{u}_S^T & \mathbf{u}_T^T \end{bmatrix}^T$$

Also:

$$\mathbf{g}_t(\mathbf{d}, \hat{\mathbf{y}}, \hat{\mathbf{u}}) < 0$$

$$\mathbf{g}_d(\mathbf{d}) < 0$$

The optimization is implemented in ModelCenterTM, which is interfaced with the Matlab[®] routines defining the various constraints and the objective function. A schematic of the Model Center implementation of the combined optimization process is shown in fig. 55.

4.5.3 Results

4.5.3.1 Optimization with reduced set of design variables

As in previous cases, design variables related to control surface dimension d_c and L_{fin} are first considered. The results of the reduced optimization presented in Tables 15 and 16 are based on the application of Logvinovich's cavity model with memory effects. This optimal vehicle has an enhanced turning performance but reduced level flight performance as a result of the compromise to be found between the two requirements in the objective function.

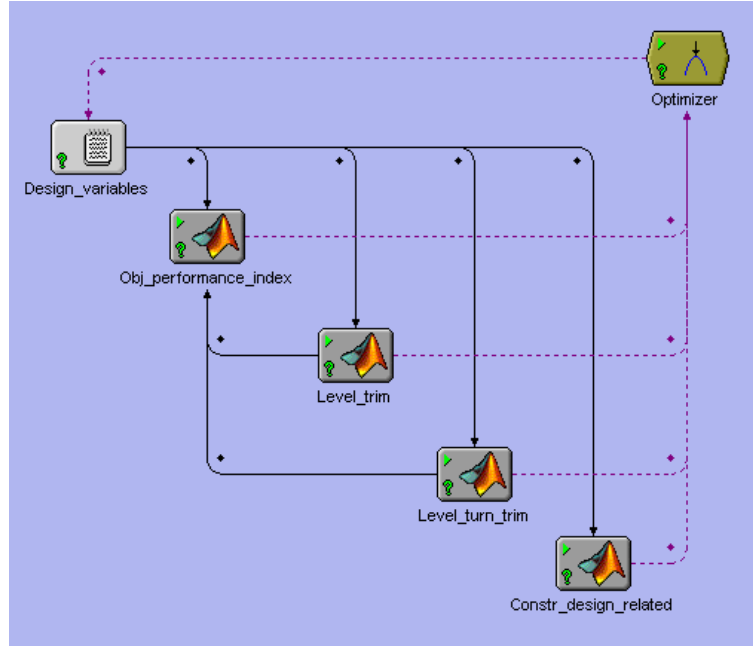


Figure 55: Flowchart of optimization using ModelCenter™.

Table 15: Reduced optimal design configuration for a combined performance of fins-supported flight.

Dimension	value	lower bound	upper bound	unit
d_c	0.0775	0.07	0.09	m
L_{fin}	0.2565	0.20	0.30	m

Table 16: Performances of reduced optimal vehicle in fins-supported flight.

Range				
	Nominal	Optimal	[%]	unit
D	0.6828	0.5908	-13.5%	m
V	89.2686	95.2409	+6.7%	m/s
δ_T	19.6097e+3	24.2355e+3	+23.6%	N
m	150	150.3262	+0.2%	kg
Turn rate				
	Nominal	Optimal	[%]	unit
Ω	1.2106	1.4552	+20.2%	rad/s
V	83.2364	106.5493	+28.0%	m/s
n	10.3257	15.8455	+53.5%	
δ_T	15.2520e+3	23.0818e+3	+51.3%	N

4.5.3.2 Optimization with full set of design variables

The results obtained for the full set of configurational design variables, and based on fins-supported flight conditions, are presented in Tables 17, 18 and 19, which summarize the performance of the optimized vehicle with respect to range and turn radius. As in the reduced case, the optimization produces a great improvement in turning performance but a reduction in level flight performance. The comparison between optimal and nominal vehicle is shown in fig. 56.

Table 17: Optimal design configuration for a combined performance of fins-supported flight.

Dimension	value	lower bound	upper bound	unit
d_c	0.0700	0.07	0.09	m
L_{fin}	0.3000	0.20	0.30	m
x_{fin}	2.9560	L_{cone}	$L_{cone} + L_{fuse}$	m
R_{veh}	0.1112	0.05	0.15	m
L_{veh}	4.0472	3.5	4.5	m
L_{cone}	2.4168	$0.1 L_{veh}$	$0.9 L_{veh}$	m
L_{aft}	0.1238	$0.01 L_{veh}$	$0.1 L_{veh}$	m

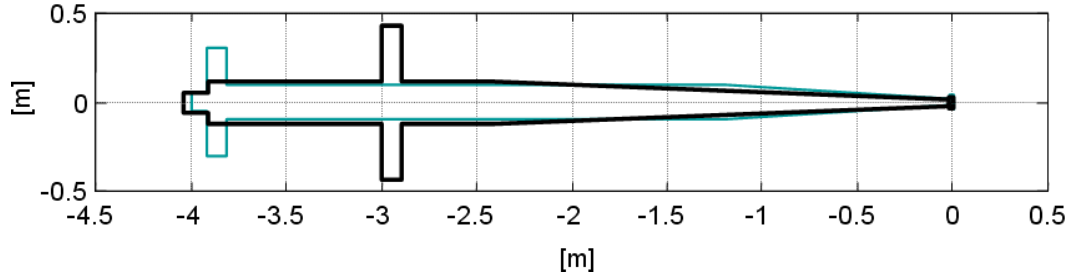


Figure 56: Optimal configurations of supercavitating vehicles based on a combined performance of maximum range and maximum turn rate during fins-supported flight.

Table 18: Controls and states of optimal configuration.

Level flight		
controls/states	value	unit
V	82.7920	m/s
δ_T	23.6273e+3	N
δ_N	-0.8823	degree
δ_{F_2}	0.0942	degree
δ_{F_4}	-0.0942	degree
δ_{F_1}	0	degree
Turning flight		
controls/states	value	unit
V	96.0004	m/s
Ω	2.6817	rad/s
ϕ	87.6871	degree
θ	0.0935	degree
ψ	2.3139	degree
δ_T	27.0604e+3	N
δ_N	-19.4478	degree
δ_{F_2}	0.0942	degree
δ_{F_4}	-0.0942	degree
δ_{F_1}	-0.0338	degree
δ_{F_3}	-0.0514	degree

Table 19: Performances of optimal vehicle in fins-supported flight.

Range				
	Nominal	Optimal	[%]	unit
D	0.6828	0.5115	-25.1%	m
V	89.2686	82.7920	-7.3%	m/s
δ_T	19.6097e+3	23.6273e+3	+20.5%	N
m	150	145.9699	-2.7%	kg
Turn rate				
	Nominal	Optimal	[%]	unit
Ω	1.2106	2.6817	+121.5%	rad/s
V	83.2364	96.0004	+15.3%	m/s
n	10.3257	26.2750	+154.5%	
δ_T	15.2520e+3	27.0604e+3	+77.4%	N

4.6 *Conclusions*

The trim analysis developed in the previous chapter is here applied to investigate configurational optimization for supercavitating vehicles. A description of performance in level flight and level turning flight is first provided, followed by a detailed discussion on the constraints limiting the flight envelope. The flight envelope of a supercavitating vehicle is significantly different from that of a conventional vehicle due to different hydrodynamic coefficients as well as a unique operational conditions, which strongly affect turning performance. A general formulation for the optimization problem is first introduced and a discussion of the practical implementation used to achieve a robust optimization solution is presented. The trim evaluation process is used as part of an optimization problem which seeks for the optimal vehicle configuration. The considered objective functions are the vehicle range, maximum turn rate, and their combination. The range is formulated as a compromise between vehicle velocity, mass and available thrust. The maximum turn rate is obtained at the corner speed, in which minimum turn radius is simultaneously obtained.

The optimization process yields design configurations which significantly improve the vehicle range or maximum turn rate in fins-supported flight. Also, the solutions of the optimization problem not only provide vehicle configuration, but also the corresponding optimal operating conditions, in terms of velocity and load factor. However optimal configurations indicate that a trade-off between two performances is required due to their conflicting requirements.

The developed optimization process will be expanded to account for maneuverability as an objective in the next chapter.

Chapter V

OPTIMIZATION OF MANEUVERING SUPERCAVITATING VEHICLES

5.1 Overview

This chapter expands the previous analysis by including maneuvering conditions as part of the optimization process. A trajectory optimization code, named TOP, for supercavitating vehicles developed at the Politecnico di Milano (Milan, Italy) is used to define optimal configurations for vehicles performing specific maneuvers [66]. Given a vehicle configuration at a sampling design point, the trajectory planner computes the trajectory maximizing an assigned performance index. The objective of the configuration optimization attempted in this chapter is to define the configuration of the vehicle providing the best performance as defined by the trajectory planner.

The chapter first provides an overview of the trajectory optimization technique implemented in the TOP code, and presents some examples of typical maneuvers. Preliminary optimization results are then presented where the trajectory code is part of system level optimization problem, whose objective is to maximize a performance index related to the considered maneuver.

5.2 Overview of the Trajectory Optimization Technique

The trajectory optimization code computes maneuvers for supercavitating vehicles based on a set of requirements. Computing a maneuver means determining the time histories of the vehicle controls and the associated time histories of the states. Any computed maneuver must always satisfy a certain number of requirements. Maneuvers must be first compatible with the vehicle dynamics, i.e. they must satisfy the equations of motion within the admissible limits imposed by the vehicle flight envelope and the necessarily limited control authority of the vehicle actuators. Moreover, maneuvers should minimize some cost function, such as the time necessary to accomplish a given goal, or maximize the final vehicle

velocity, or yet again the control effort necessary to steer the vehicle. In fact, optimality provides a way to select one meaningful solution among the typically infinite possible different ways of achieving a same goal. Finally, maneuvers must satisfy operational constraints imposed by the vehicle user.

5.2.1 The Maneuver Optimal Control Problem

All the above mentioned requirements can be met by expressing each maneuver as the solution of an appropriate optimal control problem [40]. The problem time domain is here noted $\Omega = (0, T)$, with boundary $\Gamma = \{0, T\}$, where the final time T is possibly unknown. The dynamic equations of a rigid supercavitating vehicle introduced in Chapter 2 (eq.s (2,6)) are for convenience rewritten in compact form as

$$\dot{\mathbf{y}} - \mathbf{q}(\mathbf{y}, \mathbf{u}) = 0, \quad (89)$$

The optimal vehicle state time histories $\mathbf{y}_{\text{opt}}(t)$ and associated control policy $\mathbf{u}_{\text{opt}}(t)$ define an optimal maneuver and minimize the cost function

$$J = l(\mathbf{y}, \mathbf{u}, t)|_T + \int_{\Omega} L(\mathbf{y}, \mathbf{u}, t) dt, \quad (90)$$

where the first term is the terminal cost, while the second is the integral term of the cost function. As previously stated, the optimal solution must satisfy the vehicle equations of motion (eq. (89)), which can therefore be interpreted as constraints of the optimization problem. Constraints on the states and the controls further characterize and define the maneuver, for example by providing initial and final conditions, or by providing operational and flight envelope limits. For generality, all these conditions can be expressed as inequality constraints in the form $x \in [x_{\min}, x_{\max}]$, i.e. $x_{\min} \leq x \leq x_{\max}$. Equality constraints are enforced by simply selecting $x_{\min} = x_{\max}$. The initial and terminal state conditions can be written as:

$$\boldsymbol{\psi}(\mathbf{y}(0)) \in [\boldsymbol{\psi}_{0_{\min}}, \boldsymbol{\psi}_{0_{\max}}], \quad (91a)$$

$$\boldsymbol{\psi}(\mathbf{y}(T)) \in [\boldsymbol{\psi}_{T_{\min}}, \boldsymbol{\psi}_{T_{\max}}], \quad (91b)$$

while non-linear constraints on states and controls can be expressed in general as:

$$\mathbf{g}(\mathbf{y}, \mathbf{u}, t) \in [\mathbf{g}_{\min}, \mathbf{g}_{\max}]; \quad (92)$$

similarly, constraints at a (possibly unknown) internal event T_i are:

$$\mathbf{g}(\mathbf{y}, \mathbf{u}, T_i) \in [\mathbf{g}_{T_{i\min}}, \mathbf{g}_{T_{i\max}}]; \quad (93)$$

integral conditions on states and controls can be given as:

$$\int_{\Omega} \mathbf{h}(\mathbf{y}, \mathbf{u}, t) dt \in [\mathbf{h}_{\min}, \mathbf{h}_{\max}], \quad (94)$$

and finally upper and lower bounds are:

$$\mathbf{y} \in [\mathbf{y}_{\min}, \mathbf{y}_{\max}], \quad (95a)$$

$$\mathbf{u} \in [\mathbf{u}_{\min}, \mathbf{u}_{\max}]. \quad (95b)$$

According to optimal control theory, an optimal solution to this problem is determined by first defining an augmented performance index, obtained by adjoining the system governing equations (89) and constraints (91a–94) to the performance index (90) through the use of Lagrange multipliers (co-states). Next, the stationarity of the augmented index is imposed, resulting in the definition of a set of differential equations in the states, co-states and controls, together with a set of associated boundary conditions [40].

5.2.2 Numerical Solution

This approach is however not always necessary nor convenient. In fact, one can avoid the derivation of the optimal control equations altogether [67] by discretizing the system equations (89) on a grid \mathcal{T}_h of the computational domain through some numerical discretization method. This defines a set of unknown parameters, which are represented by the discrete values of the states and controls on the computational grid. At this point, the problem cost function (90) and the boundary conditions and constraints (91a–94) are expressed in terms of the discrete parameters \mathbf{x} . This process defines a finite-dimensional Non-Linear Programming (NLP) problem which can be written as

$$\begin{aligned} \min_{\mathbf{x}} K(\mathbf{x}), \\ \text{s.t.: } \mathbf{c}(\mathbf{x}) \in [\mathbf{c}_{\min}, \mathbf{c}_{\max}], \end{aligned} \quad (96)$$

where K is the discrete counterpart of the cost J in eq. 90, while \mathbf{c} are the optimization constraints, which include the discretized system dynamic equations, the discretized constraints and the boundary conditions. Here again, necessary conditions for a constrained optimum are obtained, similarly to the case of optimal control, by combining the objective K with the constraints through the use of Lagrange multipliers, and imposing the stationarity of the augmented cost function. The resulting large but sparse problem can be solved efficiently by sequential quadratic programming (SQP) methods [68] or interior point (IP) methods [69]. The discretized time grid is $0 \equiv t_0 < t_1 < \dots < t_{n-1} < t_n \equiv T$, composed of n intervals $T^i = [t_i, t_{i+1}]$ of size h^i , $i = 0, \dots, n-1$. Since T is in general unknown, time is mapped onto a fixed domain parameter $s = t/T$, $s \in [0, 1]$. This yields the generic time step length as $h^i = T(s_{i+1} - s_i)$, $i = 0, \dots, n-1$, which is now expressed in terms of the step length in the s space and of the unknown maneuver duration. The discretized system dynamics equations can be written on the generic interval T^i as

$$\mathbf{y}_{i+1} - \mathbf{y}_i - h^i \mathbf{q}\left(\frac{\mathbf{y}_i + \mathbf{y}_{i+1}}{2}, \mathbf{u}^i\right) = 0, \quad i = 1, \dots, n-1, \quad (97)$$

where \mathbf{y}_i , \mathbf{y}_{i+1} are the values of the states at times t_i , t_{i+1} , respectively, and \mathbf{u}^i is the constant value of the controls within T^i . Note that, coherently with their algebraic nature, controls are treated as internal unknowns, which reflects the fact that no boundary conditions can be associated with these variables. Given the discretization of the equations expressed by (97), the NLP variables \mathbf{x} are defined as

$$\mathbf{x} = (\mathbf{y}_i^T (i = 0, \dots, n), \mathbf{u}^{iT} (i = 0, \dots, n-1), T)^T, \quad (98)$$

i.e. they include the state values at the grid vertices, the control values on each grid element and, possibly, the final time. The cost function and all problem constraints and bounds, including eq.s (97), are expressed in terms of the NLP variables \mathbf{x} to yield the finite dimensional optimization problem 96.

5.2.3 Implementation issues

The success of direct transcription methods is directly dependent on the efficiency and robustness of the nonlinear programming (NLP) solvers. There are various commercial NLP

packages such as NPSOL, SNOPT and CFSQP [36]. Due to the advanced development of numerical linear algebra, large scale problems can be solved through the exploitation of the sparsity of the matrices [23]. The code TOP uses SNOPT [70], a sequential quadratic programming (SQP)-based NLP solver developed by the Stanford Systems Optimization Laboratory. The solver is particularly efficient as it allows the user to provide the gradient of the objective function, as well as the Jacobian of linear and nonlinear constraints. It is in particular efficient when dealing with sparse problems, as the sparsity pattern can be directly provided by the user, which allows the code to neglect all zero terms, thus significantly reducing the computational cost. As a result, SNOPT requires relatively few evaluations of the problem functions and hence it is especially effective for problems with expensive objective and/or constraint functions [70].

The TOP code version available for this work has limitations regarding the implemented cavity model, which does not account for memory effects. Although this restriction may be critical for highly aggressive maneuvers, the accuracy of the current formulation is considered sufficient for moderate maneuvers involving a smoothly curved flight path. This is one of the reasons motivating the choice, in this work, to consider turn maneuvers corresponding to a maximum heading change of 40° .

Finally, one should mention that the flight path predicted through TOP is to a certain degree sensitive to user-defined parameters such as the number of nodes used for time discretization, and the initial guess. Fig. 57 shows for example the result of a convergence test made using TOP. The performance index (in this case maneuver time) resulting from the trajectory optimization is plotted versus the number of nodes in the time grid to show how convergence of results is achieved upon refinement of the grid and that, for the case at hand, a 40-node grid could be considered sufficient for an accurate prediction of the considered optimal maneuver.

The solution of NLP problems generally exhibits a dependence on the initial guess. Suitable initial guesses can be obtained through the application “bootstrap” and “continuation” techniques [46]. The bootstrap technique consists in the iterative solution of a specified problem on progressively finer grids. At each iteration, the initial guess is chosen

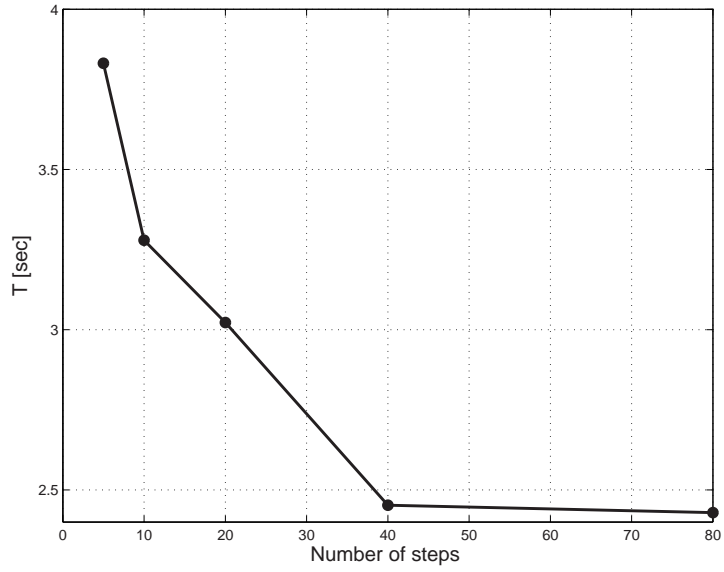


Figure 57: Convergence test regarding to the resolution of discretization for the minimum flight time of heading-changing fins-supported flight.

as the solution from the previous iteration, projected on the refined grid. The application of the bootstrap technique prevents the divergence of the solution and enhances the convergence rate for complicated problems. Good initial guesses can be also found through the continuation or “homotopic” approach [30]. A difficult problem, such as a highly aggressive maneuver, is solved incrementally, by formulating and solving a set of simpler problems, and by considering the solution of one problem as an initial guess for the subsequent one. For example, the optimal path corresponding to a 180° heading change, can be solved as the progressive solution of 10° -heading change problems, with the initial guess derived directly from the solution of the previous problem.

5.2.4 Examples

This section presents a series of examples obtained using the TOP code, which briefly illustrate the capability of the code, and have been used as part of this work to gain familiarity with the code, its sensitivity to user-defined parameters and its input-output structure. Such familiarity is essential to formulate an optimization problem based on TOP, as presented in the next section.

The vehicle configuration used for the simulations reflects the nominal configuration considered in this work (see Table 1). The optimization cost function used in the following studies is

$$J = w_1 T^2 + w_2 \int_0^T \dot{\mathbf{u}} \cdot \dot{\mathbf{u}} dt, \quad (99)$$

where T denotes the total unknown time required to perform a desired maneuver, while the second term of the cost includes the control velocities $\dot{\mathbf{u}}$. This second contribution is here introduced to provide a limit to the control rates, which would reflect limited actuation capabilities of the control actuators. Also, in eq. (99), w_1, w_2 are user defined weight parameters that scale the contribution of the two terms of the cost. The examples below reproduce part of the results presented in [46].

5.2.4.1 Dive Maneuvers

A vehicle initially flying at trim conditions ($V = 85$ m/s) is required to dive to an assigned depth where it continues to operate at the same initial trimmed state. Optimal trajectories for a final depth varying between 5 m and 50 m are shown in fig. 58. The results are obtained through the application of the continuation technique, whereby the results of each optimization are used as a starting guess for the next dive. The maneuvers correspond to minimum time performance requirements as defined by selecting $w_1 = 1, w_2 = 1/100$ in eq. (99). Constraints on the controls and on their rates are imposed: for example the thrust is constrained to vary between 0 and $\delta_{T_{\max}} = 33,000$ N, which is an arbitrary upper limit imposed by the generic propulsion system considered in this study. Figure 59 presents the time histories of the corresponding controls. The plots show how the thrust and the cavitator angle vary in an approximately linear fashion between their minimum and maximum values. Such linear variations are the result of the control rates reaching the corresponding imposed bounds. It is worthwhile noting that all the controls return to their initial value as the maneuver is completed and the vehicle reaches the designated trim state. The rudder controls time histories are omitted in this case as they remain identically equal to zero. Finally, fig. 60 shows the time histories of the horizontal and vertical velocity components in the body-fixed frame, together with the pitch rate.

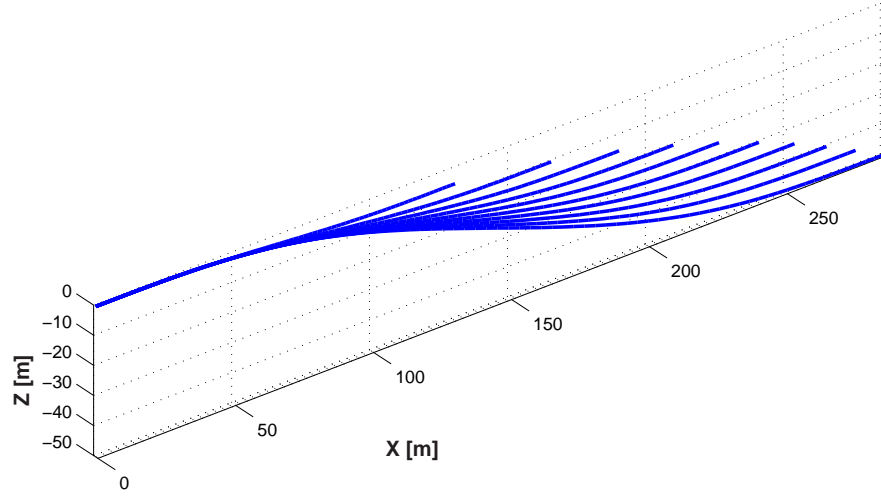
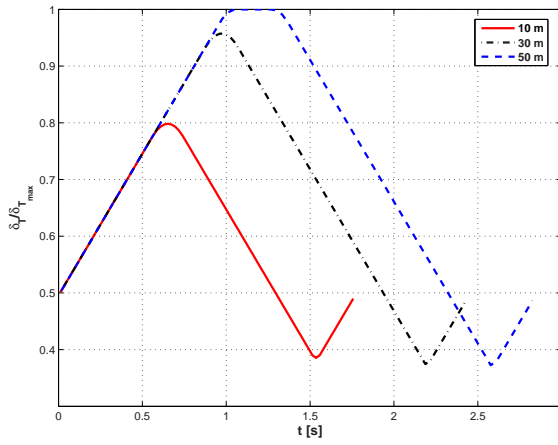
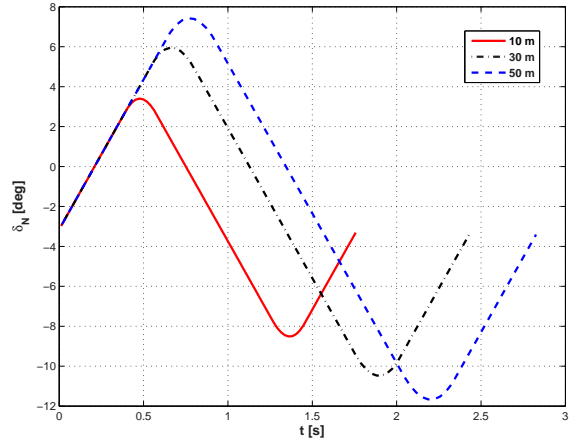


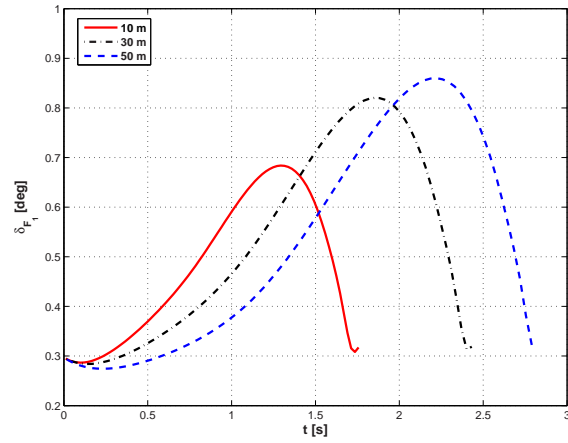
Figure 58: Family of dives for increasing final depth.



(a) Thrust



(b) Cavitation angle



(c) Elevator angle

Figure 59: Control time histories for the diving problem.

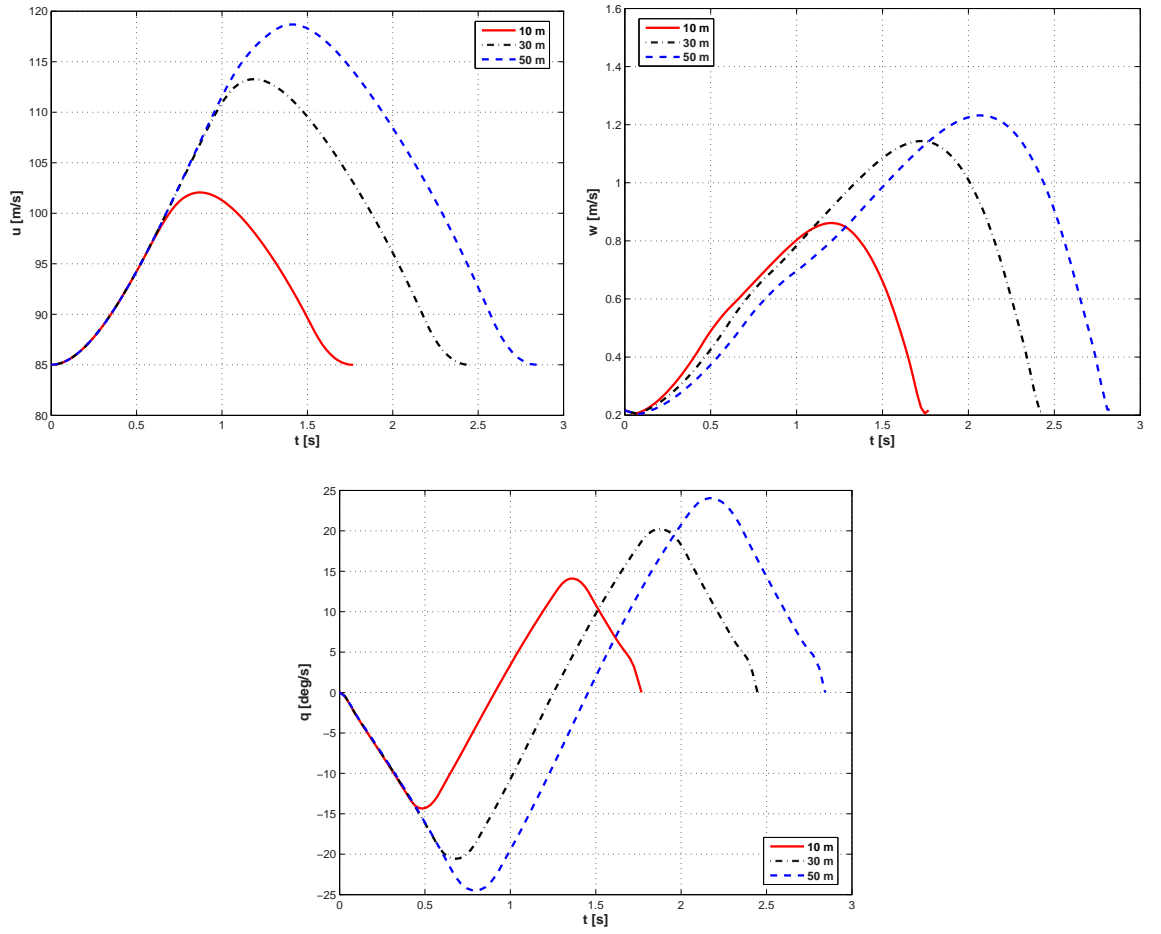


Figure 60: State time histories for the diving problem.

5.2.4.2 Turn Maneuvers

Shown in fig. 61 is a family of turns for heading changes varying from 10° to 180° . The vehicle is initially at trim flying with an horizontal velocity of 85 m/s, and it is required to achieve a trimmed state at the same velocity after the specified change in heading. The maneuvers in fig. 61 are again minimum time turns, obtained through the application of a continuation technique. It is interesting to observe how all of the resulting trajectories are three dimensional, and are somewhat different from the simple level turn in the xy plane which one might expect. The vehicle Euler angles (in the 3-2-1 sequence) shown in fig. 62 for some representative turns confirm that significant roll and pitch occur during these maneuvers.

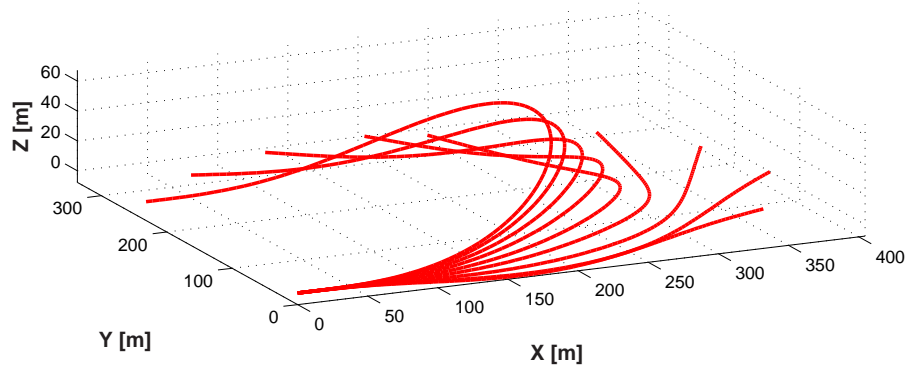
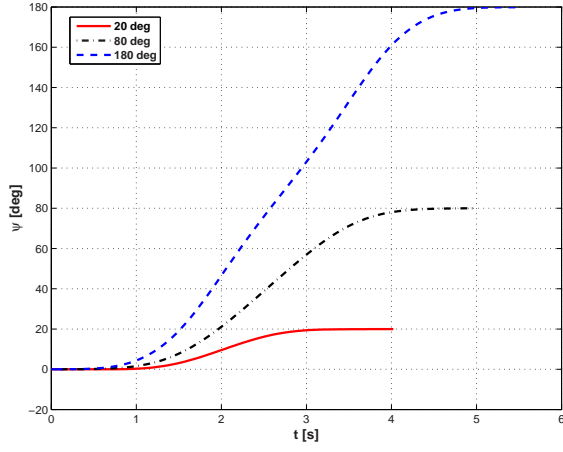
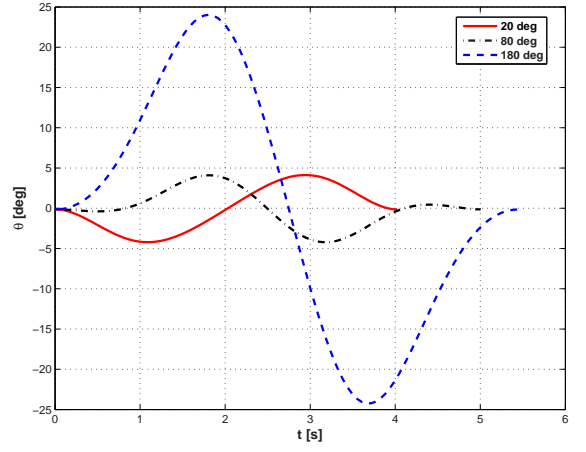


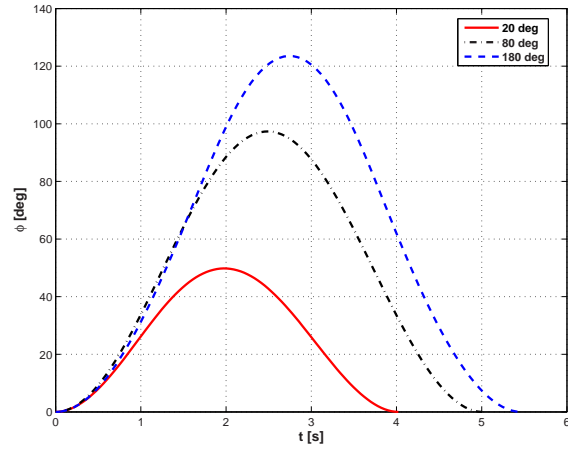
Figure 61: Family of turns for heading change varying between 10 deg and 180 deg.



(a) Yaw



(b) Pitch



(c) Roll

Figure 62: Time histories of Euler angles during representative turns.

5.3 Optimization of Maneuvering Vehicles

5.3.1 Design variables and objective function

A conceptual design for the vehicle is here investigated. The nominal configuration described earlier is used as a starting point for the design. The vector of the configuration design variable is defined as before:

$$\mathbf{d} = \{ d_c \quad L_{fin} \quad x_{fin} \quad R_{veh} \quad L_{veh} \quad L_{cone} \}^T \quad (100)$$

The optimization is performed by considering a turn maneuver where the vehicle has to complete a heading change of a specified angle. A performance index C related to the specified maneuver is considered as the overall objective to be optimized. The optimization problem can therefore be again described as follows:

$$\begin{aligned} \max_{\mathbf{d}} \quad & C(\mathbf{d}, \mathbf{y}, \mathbf{u}), \\ \text{s.t.:} \quad & \mathbf{c}(\mathbf{d}, \mathbf{y}, \mathbf{u}) \leq 0. \end{aligned} \quad (101)$$

In eq. (101), $\mathbf{c}(\mathbf{d}, \mathbf{y}, \mathbf{u})$ denotes the array of equality and inequality constraints which define design and operational constraints:

$$\mathbf{c}(\mathbf{d}, \mathbf{y}, \mathbf{u}) = \begin{bmatrix} J(\mathbf{d}, \mathbf{y}, \mathbf{u}) - J_{\min}(\mathbf{d}, \mathbf{y}, \mathbf{u}) \\ g_t(\mathbf{d}, \mathbf{y}, \mathbf{u}) \\ g_d(\mathbf{d}) \end{bmatrix} \quad (102)$$

with

$$\begin{aligned} J(\mathbf{d}, \mathbf{y}, \mathbf{u}) - J_{\min}(\mathbf{d}, \mathbf{y}, \mathbf{u}) &= 0 \\ g_t(\mathbf{d}, \mathbf{y}, \mathbf{u}) &< 0 \\ g_d(\mathbf{d}) &< 0 \end{aligned}$$

where J is the cost function considered in the TOP code. Equation (101) describes a formulation where the optimization of the trajectory is implemented as a constraint to a system level optimization, which seeks for the optimal configuration of the vehicle. Given, a configuration \mathbf{d} , the TOP code finds the optimal time histories for states and controls

according to the specified performance index J . The system level optimization seeks for the configuration allowing to perform the specified maneuver with optimal performance as defined by the index C .

The cost function in TOP is assigned as:

$$J = w_1 T^2 + w_2 \frac{1}{T - T_o} \int_{T_o}^T \delta_T^2 dt + w_3 \frac{1}{T - T_o} \int_{T_o}^T \dot{\mathbf{u}} \cdot \dot{\mathbf{u}} dt \quad (103)$$

where T , δ_T , and \mathbf{u} denote respectively flight time, thrust, and controls. The weighting factors w_1 , w_2 , and w_3 are selected as 10, 1, and 1 for the flight time, thrust control effort, and control rates. Control rates are important to obtain a physically feasible solution, compatible with actuation limitations, and to ensure smooth controls' time histories.

It should be noted how the selection of performance index J , weights w_i and objective function in the system level optimization is somewhat arbitrary, and a more extensive investigation of relevant flight conditions as well as maneuvers should be performed to obtain a meaningful objective and performance index for TOP. However, this is a first attempt of introducing a maneuvering condition as part of the optimization process, and therefore a simple, somewhat relevant maneuver is considered. Further developments may need to consider strategic considerations or a detailed analysis of the flight envelope and operating conditions for this class of vehicles. It is however expected that such considerations could be implemented in a similar way as part of the system level optimization.

5.3.2 Constraints

Constraints in TOP are selected as part of a proper definition of the heading-change maneuver. The vehicle starts from level trimmed flight with zero pitch angle and zero heading angle to reach the same trimmed flight conditions at a heading angle of 40° after completing the maneuver. At each system level optimization iteration the vehicle geometry and dimensions, as well as hydrodynamic coefficients, such as the cavitation number, are fed to the parameter input file of TOP. Initial guesses in TOP are calculated based on trim conditions updated at each optimization iteration. For example, angular velocities are set to zero at the initial and final time, controls are assigned as the trimmed values, positions in the inertial frame are assigned based on a horizontal circular path approximating the

trajectory, for a guessed time and trimmed velocity, and the attitude at initial and final stages are respectively given by $\Phi_i = [0, 0, 0]^T$ and $\Phi_f = [0, 0, 40^\circ]^T$. Additionally, proper bounds are defined for states and controls throughout the maneuver. In the considered optimization, the maneuvering time is one of the unknowns which is bounded by assigning a suitable lower and upper value.

5.3.3 Implementation of optimization procedure

Given the complexity of the problem and expensive computation of maneuvers, response surfaces methodology will be first attempted to replace the maneuver tool TOP with simple approximate expressions. Response surfaces approximate objective function and constraints according to the following expressions:

$$C_h(\mathbf{d}, \mathbf{y}, \mathbf{u}) = \sum_i N_i C(\mathbf{d}_i, \mathbf{y}, \mathbf{u}) \quad (104)$$

and

$$\mathbf{c}_h(\mathbf{d}, \mathbf{y}, \mathbf{u}) = \sum_i N_i \mathbf{c}(\mathbf{d}_i, \mathbf{y}, \mathbf{u}) \quad (105)$$

where N_i is a set of basis function. The response surfaces are obtained by sampling the solution space at points characterized by the values of the design variables \mathbf{d}_i . Adaptive sampling can be used for refining the response surface approximation in the neighborhood of the solution. For each point \mathbf{d}_i , the trajectory optimization tool TOP is called for evaluating the performance corresponding to the specific vehicle configuration, which in turn contributes to the approximation of cost and constraints. Given the response surfaces approximation, the configurational optimization loop (see eq. (68)) can be expressed as

$$\begin{aligned} \max_{\mathbf{d}} \quad & C_h(\mathbf{d}, \mathbf{y}, \mathbf{u}), \\ \text{s.t.} \quad & \mathbf{c}_h(\mathbf{d}, \mathbf{y}, \mathbf{u}) \leq 0. \end{aligned}$$

which can be solved using a gradient based optimization approach.

In this work, as a first response surface approximating function, the following simple

polynomial regression will be used

$$\begin{aligned}
y = & \beta_0 + \sum_{i=1}^n \beta_i x_i + \sum_{i=1}^n \beta_{ii} x_i^2 + \sum_{i=1}^{n-1} \sum_{j=2, j>i}^n \beta_{ij} x_i x_j \\
& + \sum_{i=1}^n \beta_{iii} x_i^3 + \sum_{i=1}^n \sum_{j=2, j \neq i}^n \beta_{ijj} x_i^2 x_j + \sum_{i=1}^{n-2} \sum_{j=2, j>i}^{n-1} \sum_{k=3, k>j}^n \beta_{ijk} x_i x_j x_k \quad (106)
\end{aligned}$$

where y and x are the approximate response and design variables. The unknown parameter β s are usually determined by least-square linear regression analysis by fitting the response surface to sampling data [71]. When one has little knowledge about the true response, a low order model is first considered. The order of the model is then increased by adding higher order terms if a low order model suffers from lack of fit. Typically, first and second order models are used.

In spite of computational efficiency and simplicity, the response surface methodology (RSM) has inherent disadvantages as the difficulty of avoiding infeasible sampling points during the Designs of Experiments (DoE) and limitations of representing the complex non-linearity of a true model. In this study, the first problem is circumvented by sufficiently reducing the range of the design variables so that most of the sampling data remains in the feasible region and the number of failed cases is small. The second disadvantage can be mitigated through other metamodeling techniques such as Kriging, which shows a better capability of capturing the nonlinearity of the model [72]. Instead of exploring various available metamodeling techniques, here the capability of RSM is taken into consideration by achieving optimization with and without simple RSM based polynomial regression as defined in eq. (106).

5.3.4 Optimization for minimum flight time

A first optimization is performed by considering the maneuver time T as the objective function. Accordingly, the cost function considered in eq. (101) is defined as:

$$C(\mathbf{d}, \mathbf{y}, \mathbf{u}) = T(\mathbf{d}, \mathbf{y}, \mathbf{u}) \quad (107)$$

It is interesting to note that the cost function J of TOP itself includes the flight time. Therefore, the minimum flight time obtained in the system-level optimization corresponds

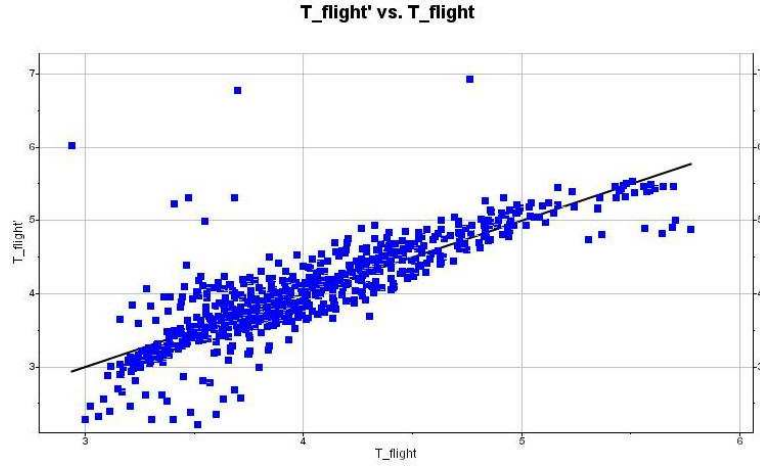


Figure 63: Comparison of minimum flight time estimated through direct solution and response surface approximation.

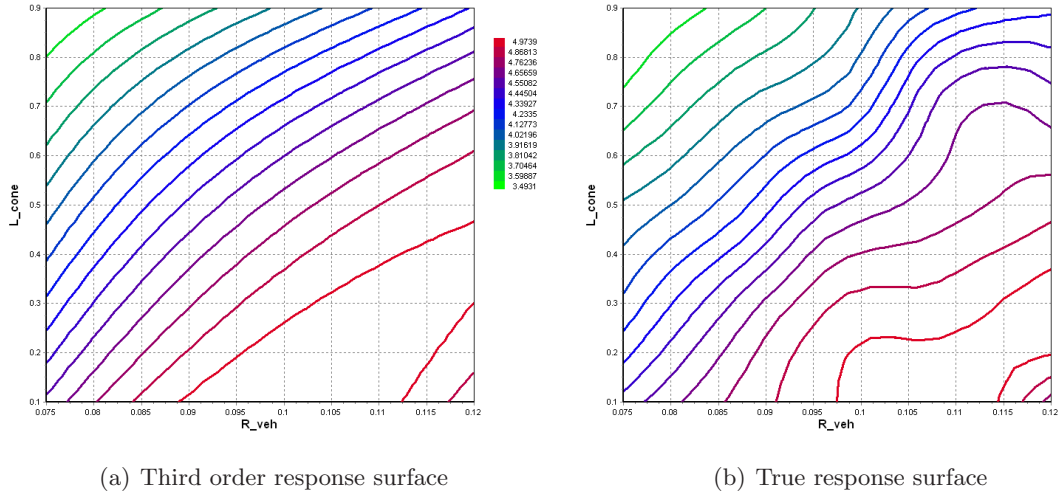


Figure 64: Variation of the minimum flight time versus vehicle radius and cone length.

to the minimum out of the possible trajectories and considered configurations for the vehicle. The minimum flight time can be also considered as a good measure of maneuverability and an important characteristic along with other performance indexes such as range and turn rate in steady flight.

Figure 63 compares the minimum flight time estimations for a number of configurations as estimated through the direct solution of the trajectory optimization problem and through the approximation through response surfaces. Specifically, the flight time along the abscissa denotes the value computed at the sampling points, while the ordinate corresponds to the

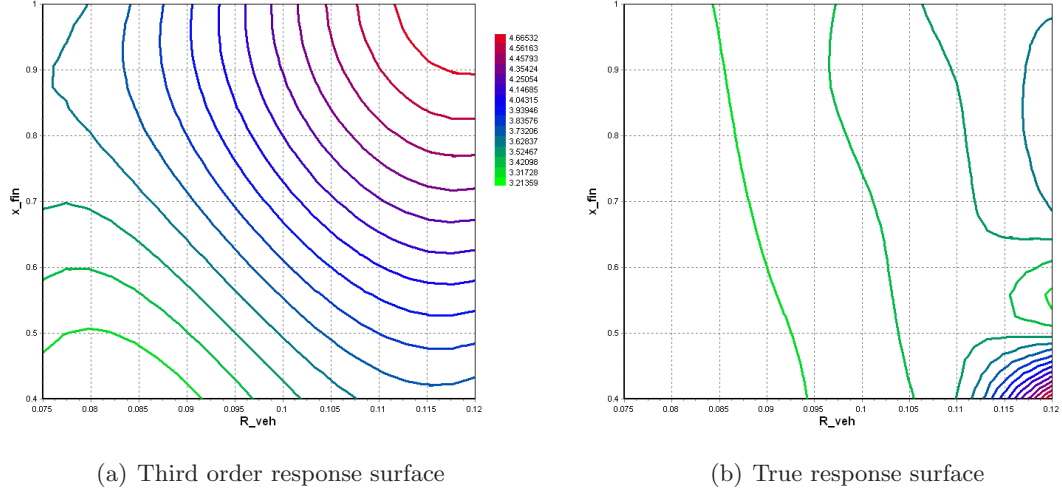


Figure 65: Variation of the minimum flight time versus vehicle radius and fin location.

one predicted by the produced response surface. The results correspond to third order polynomial regression equation (full cubic model), whose DoE is based on 3 levels of full factorial sampling. As shown in the figure, the accuracy of response is quite low. Figures 64 and 65 show the variations of the minimum flight time in terms of selected configuration variables. The flight times are respectively estimated through third order response surfaces and true maneuver tool TOP. Fig. 64 shows the variation of minimum flight time in terms of vehicle radius R_{veh} and cone length L_{cone} . Comparison of the two contours shows sufficient similarity, which suggests that good predictions can be obtained with small sampling levels. In contrast, the variation of minimum time with respect to vehicle radius (R_{veh}) and fin's location (x_{fin}) in fig. 65 shows considerable differences between regression polynomial and true response surfaces. This indicates that a trade-off between the accuracy of response surface and computational cost must be considered.

Figure 66 summarizes the effects of the individual design variable on the minimum flight time, in comparison with the other performance indexes previously considered. The results show the dominant effects of the fins' location x_{fin} , and to a lesser extent of the vehicle radius R_{veh} and cone length L_{cone} . The influence of the various configuration parameters on the minimum maneuvering time is clearly in contrast with that on the other performance indexes. It is particularly interesting that the fins' length, which has the dominant effect on

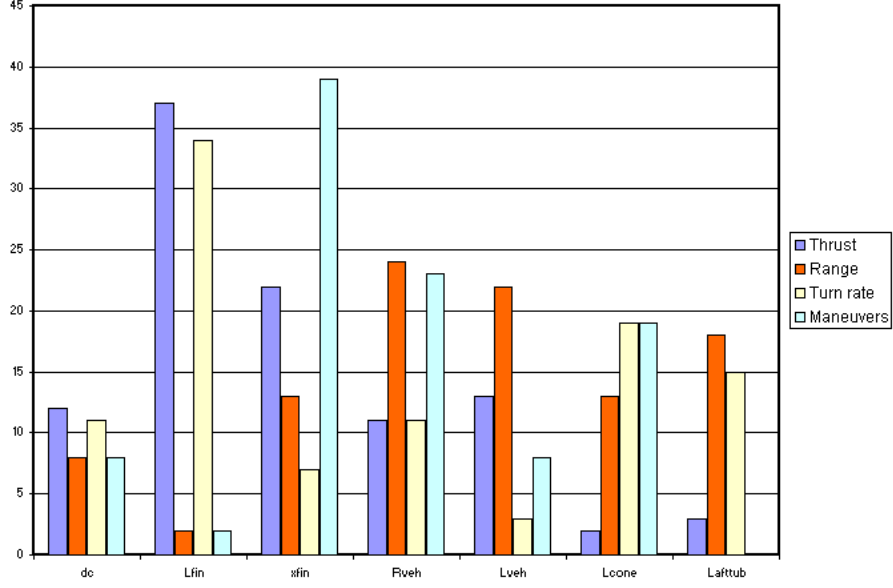


Figure 66: Effects of individual design variables on various performance indexes.

the maximum turn rate in trim conditions, has little influence on the minimum time turn maneuver.

5.3.4.1 Optimization results

As in previous cases, a preliminary optimization is conducted by considering a reduced set of design variables, which includes fins' location (x_{fin}), vehicle radius (R_{veh}), and vehicle cone length (L_{cone}). These parameters are identified as relatively dominant in fig. 66. The results of the reduced optimization are presented in Tables 20 and 21, which are obtained using third order response surfaces constructed based on 3 level full factorial sampling data. As implied in fig. 65, the rich nonlinearity of the design space degrades the accuracy of response surface approximation, particularly of second order model. In spite of deficient accuracy, the vehicle with this optimal configuration produces a considerable improvement (-34.2%) in minimum maneuvering time, which is achieved by increasing the vehicle radius and vehicle cone length. It should be noted that minimum flight times are all reevaluated by the actual analysis tool (TOP) with optimal configurations found through approximate response surface.

The results obtained by considering the full set of design variables are presented in

Table 20: Optimal design configuration for reduced design variable set: minimum time 40° heading-change maneuver.

Dimension	value	lower bound	upper bound	unit
x_{fin}	3.9898	$L_{cone} + 0.4L_{fuse}$	$L_{cone} + L_{fuse}$	m
R_{veh}	0.1039	0.075	0.12	m
L_{cone}	1.9608	$0.1 L_{veh}$	$0.9 L_{veh}$	m

Table 21: Performance of optimal design configuration for reduced design variable set: minimum time 40° heading-change maneuver.

	Nominal	Optimal	unit	[%]
T	4.7038	3.0972	second	-34.2%

Tables 22 and 23. Table 22 lists the optimal value of the design variables as well as lower and upper bounds considered in the optimization process. The comparison between optimal and nominal vehicle is shown in fig. 67. This configuration shows a similarity with the optimized configuration (cone-shape design in fig. 53) based on maximum turn rate except for an opposite trend in the fins' length (this is also implied in fig. 66). The optimal vehicle is able to perform the required maneuver with a considerably reduced (-47.0%) maneuvering time. The comparison of optimized trajectories performed by optimal and nominal vehicles is also shown in fig. 68. The predicted trajectories show that the optimized vehicle performs the required maneuver in a more aggressive fashion, which suggests a higher maneuverability. This statement is partially supported by the evaluation of the flight time of optimized and nominal vehicles for heading-change maneuvers of increasing angles. The results are summarized in fig. 69, which shows that the optimal vehicle performs better, in terms of minimum time, than the nominal one over a broad range of turning maneuvers. Figure 70 shows the corresponding trajectories of the optimal vehicle.

5.3.5 Optimization for minimum average thrust

A second example is conducted by considering the following cost function in eq. (101):

$$C(\mathbf{d}, \mathbf{y}, \mathbf{u}) = \delta_{T_{avg}} = \frac{1}{T - T_o} \int_{T_o}^T \delta_T dt \quad (108)$$

Table 22: optimal design configuration for full design variable set: minimum time 40° heading-change maneuver.

Dimension	value	lower bound	upper bound	unit
d_c	0.085	0.079	0.085	m
L_{fin}	0.200	0.20	0.30	m
x_{fin}	2.4424	$L_{cone} + 0.4L_{fuse}$	$L_{cone} + L_{fuse}$	m
R_{veh}	0.11252	0.075	0.12	m
L_{veh}	3.5	3.5	4.1	m
L_{cone}	1.7374	0.1 L_{veh}	0.9 L_{veh}	m
m	142.74567	140	160	kg

Table 23: Performance of optimal design configuration for full design variable set: minimum time 40° heading-change maneuver.

	Nominal	Optimal	unit	[%]
T	4.7038	2.4907	second	-47.0%

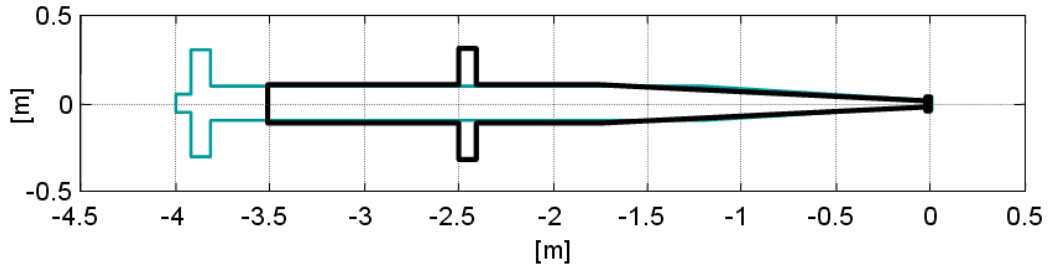


Figure 67: Optimal configurations of supercavitating vehicles based on minimum flight time during fins-supported heading-changing maneuver.

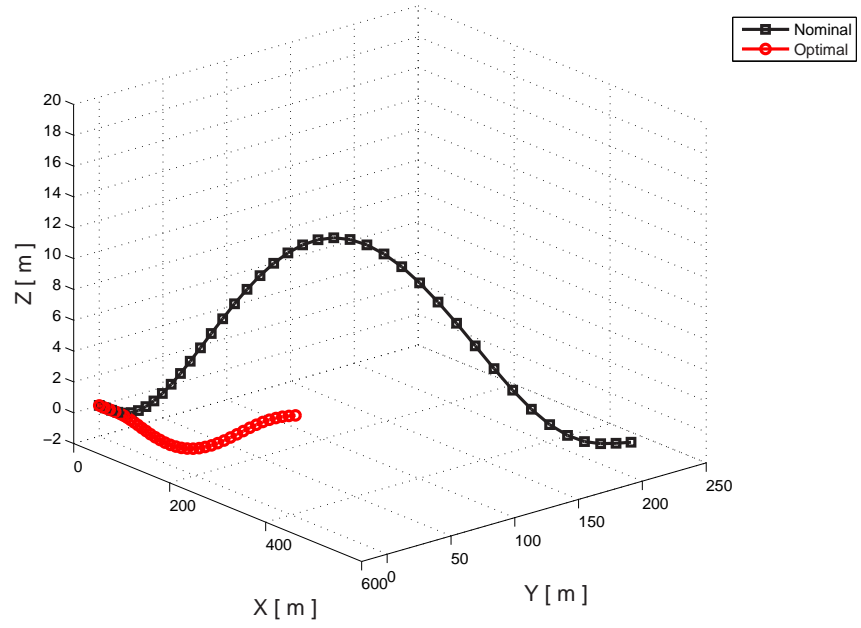


Figure 68: The comparison of trajectory between the optimal and nominal vehicle for minimum flight time for the heading-changing fins-supported maneuver.

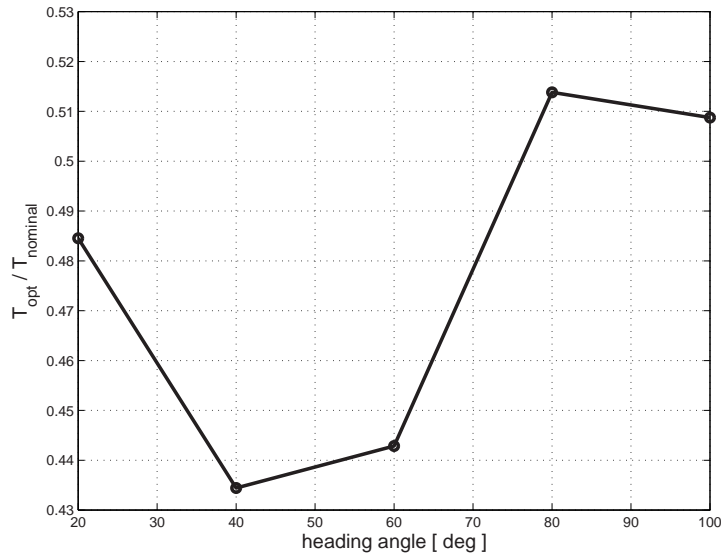


Figure 69: The optimal-to-nominal maneuvering time ratio with respect to heading angle.

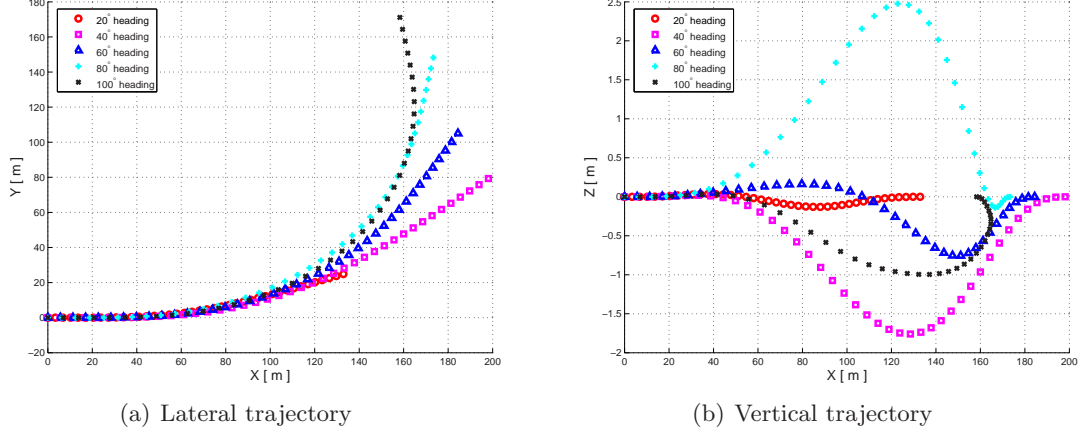


Figure 70: The trajectory of the optimal vehicle according to heading angles.

For the performance index of TOP, the same cost function defined in eq. (103) is used with differently assigned weighting factors, which are selected as 0, 1, and 1. In addition, maneuvering time is fixed at 10 sec instead of being unknown as the previous case. This class of performance and conditions will estimate the effect of vehicle configuration on the control efforts (time-average thrust) during a heading-changing maneuver of the vehicle at given mission time together with minimum control efforts and control speed. As the minimum maneuvering time case, third order response surface constructed based on 3 level full factorial sampling data is used to approximate real maneuvering tool TOP.

The results obtained by considering the full set of design variables are presented in Tables 24 and 25. In contrast to the previous case, the optimal vehicle seeking minimum thrust shows little improvement. This may be caused by inappropriate modeling of RSM on the true response rather than by physical inherent characteristics. In the table, $\delta_{T_{max}}$ and P_{avg} respectively represent maximum thrust and time-average power (thrust times vehicle velocity) during maneuvering. Although they are evaluated at the nominal and optimal cases only, their improvements shows strong coherency to each other.

For a complete discussion, optimization without RSM is performed over wider range of design variables. Tables 26 and 27 present the results. The optimal vehicle is capable of performing the maneuver with a meaningfully reduced (-22.0%) average thrust. The comparison between optimal and nominal vehicle is shown in fig. 71.

As suggested by the complex design space in fig. 65, this optimization results also indicates that the limited ability of RSM (particularly simple polynomial regression) to capture the complex nonlinearity of the design space may lead to little effectiveness of the optimization process. This difficulties may be avoided in two ways: by sufficiently restricting the design space (essentially, a smooth function will be well captured by polynomial regression in a small region) and exploiting other metamodeling techniques able to better capture the complexity of the design space. Complex nonlinearity of the design space essentially leads to a multi-modal structure problem requiring global optimum searching schemes. This features will be discussed in more detail in the next chapter.

Table 24: Optimal design configuration for full design variable set: minimum average thrust 40° heading-change maneuver.

Dimension	value	lower bound	upper bound	unit
d_c	0.0791	0.079	0.085	m
L_{fin}	0.2002	0.20	0.30	m
x_{fin}	3.4928	$L_{cone} + 0.4L_{fuse}$	$L_{cone} + L_{fuse}$	m
R_{veh}	0.1196	0.075	0.12	m
L_{veh}	3.5010	3.5	4.1	m
L_{cone}	1.8522	$0.1 L_{veh}$	$0.9 L_{veh}$	m
m	160.0	140	160	kg

Table 25: Performance of optimal design configuration for full design variable set: minimum average thrust 40° heading-change maneuver.

	Nominal	Optimal	unit	[%]
δ_{Tmax}	20.2089e+3	19.2232e+3	N	-4.9%
δ_{Tavg}	19.6719e+3	19.1294e+3	N	-2.8%
P_{avg}	3.3997e+6	3.26426e+6	J/s	-4.0%

Table 26: Optimal design configuration for full design variable set: minimum average thrust 40° heading-change maneuver (without RSM).

Dimension	value	lower bound	upper bound	unit
d_c	0.0690	0.02	0.1	m
L_{fin}	0.1883	0.15	0.25	m
x_{fin}	3.3621	L_{cone}	$L_{cone} + L_{fuse}$	m
R_{veh}	0.0968	0.05	0.15	m
L_{veh}	4.0586	3.5	4.5	m
L_{cone}	1.0276	0.1 L_{veh}	0.9 L_{veh}	m
L_{aft}	0.0722	0.01 L_{veh}	0.1 L_{veh}	m
m	147.5363	140	160	kg
V	82.8902	76	120	m/s

Table 27: Performance of optimal design configuration for full design variable set: minimum average thrust 40° heading-change maneuver (without RSM).

	Nominal	Optimal	unit	[%]
δ_{Tmax}	20.2089e+3	15.8075e+3	N	-21.8%
δ_{Tavg}	19.6719e+3	15.3369e+3	N	-22.0%
P_{avg}	3.3997e+6	2.5785e+6	J/s	-24.2%

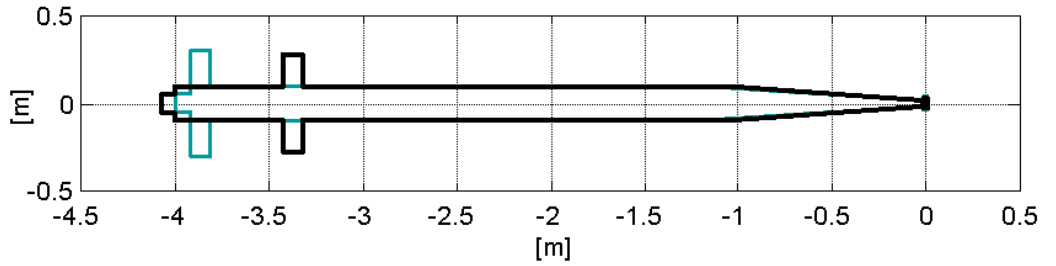


Figure 71: Optimal configurations of supercavitating vehicles based on minimum average thrust during fins-supported heading-changing maneuver.

5.4 *Conclusions*

The optimization process developed in the previous chapter is expanded to account for the vehicle's performance during a maneuver. The maneuver is defined by a set of operational and physical constraints and it is identified through the solution of a trajectory optimization problem. Given a vehicle configuration, the solution of the trajectory optimization problem identifies the trajectory, and the associated controls' histories maximizing an assigned performance index. The code utilized for the trajectory optimization has been developed at the Politecnico di Milano, and it has been here integrated as part of the configurational optimization process. In this chapter, the vehicle design is optimized in order to maximize a specified performance index related to the maneuver of the vehicle. The entire optimization process hence relies on two nested optimization loops. The inner loop consists in the evaluation of the optimal trajectory for a given vehicle configuration, while the outer loop performs a system-level optimization which seeks for the optimal vehicle configuration maximizing a maneuver-related performance index.

The considered reference maneuver consists in a heading change of a specified angle, which is optimized based on the minimization of the required time together with corresponding control efforts and rates. Two examples of system level optimizations are presented. The first one considers as system-level cost function the maneuver time. The computational cost for the evaluation of the cost function is reduced through the application of polynomial regression RSM. The analysis shows that although the accuracy of the approximating response surfaces suffers from the complex behavior of the true model, the process is able to produce a meaningful improvement in performance. A second case considers thrust as a performance index. The application of the RSM in this case does not produce a meaningful improvement in performance. In contrast, the solution without approximations, despite a longer computational time, yields better results. The application of RSM may therefore suffer from lack of accuracy at the cost of great computational efficiency, while the direct evaluation of maneuver code may suffer from expensive computation as well as local minima due to inherent nonlinearity and multi-modal structure of the design space.

In the next chapter, the vehicle optimization will be attempted by including the various

operating conditions considered so far. Specifically, trim conditions in level and turning flight, as well as the considered reference maneuver will be considered as constraints in a system-level optimization which seeks to maximize a selected performance index.

Chapter VI

INTEGRATED VEHICLE OPTIMIZATION

6.1 Overview

This chapter presents the configurational optimization of a supercavitating vehicle based on the combination of various performance requirements and design constraints developed in the previous chapters. The vehicle range is selected as the primary objective, while trim performance and maneuverability are considered as constraints. Specifically, the optimization process described in this chapter seeks for a maximum range vehicle which satisfies specified trim conditions as well as pre-defined maneuvering requirements. In particular, the maneuver constraint is implemented by pre-assigning an upper bound on the maneuvering time. The lower the time, the more stringent the requirements on the vehicle's configuration, while a loose (large) maneuvering time introduces a loose constraint on the process, which may remain mostly inactive during the optimization process. The methodology under consideration considers a limited spectrum of operating conditions, but it is formulated in a way that may allow its extension to include a number of such operational constraints, as required by specific mission requirements.

This methodology, attempts to include maneuvering flight as well as trim performance in the initial phase of the design process, can provide significant benefits and lead to a better performance according to desired mission profiles of the vehicle. In addition, the selection and the design of the control surfaces and of their degrees of freedom can be directly driven by the vehicle performance during critical maneuvers, or/potentially by the objective of extending the flight envelope.

As design conflicts between various performances are observed in previous chapters, their effect on the primary objective is estimated through the analysis of the history of the active constraints during the optimization iterations as well as of the final optimal solutions. Furthermore, difficulties related to nonlinearity and multi-modal structure of

the design space motivate the development of a simple methodology whose effectiveness is initially demonstrated on a sample problem characterized by a well-behaved objective function and discontinuous, multi-modal non-convex constraints.

6.2 Formulation of The Optimization Problem

The optimization procedure in eq. (68) is extended to include various trim conditions and maneuvers. The optimization procedure can be again expressed as:

$$\begin{aligned} \max_{\mathbf{d}} \quad & C(\mathbf{d}, \mathbf{y}_S, \mathbf{u}_S), \\ \text{s.t.:} \quad & \mathbf{c}(\mathbf{d}, \hat{\mathbf{y}}, \hat{\mathbf{u}}) \leq 0. \end{aligned} \tag{109}$$

where $\hat{\mathbf{y}}, \hat{\mathbf{u}}$ are vectors containing states and controls corresponding to the considered trim configurations, while $\mathbf{c}(\mathbf{d}, \hat{\mathbf{y}}, \hat{\mathbf{u}})$ defines an array of equality and inequality constraints corresponding to design and operational constraints:

$$\mathbf{c}(\mathbf{d}, \hat{\mathbf{y}}, \hat{\mathbf{u}}) = \begin{bmatrix} \phi_S(\mathbf{d}, \mathbf{y}_S, \mathbf{u}_S) \\ \phi_T(\mathbf{d}, \mathbf{y}_T, \mathbf{u}_T) \\ T(\mathbf{d}) - T^* \\ \mathbf{g}_t(\mathbf{d}, \hat{\mathbf{y}}, \hat{\mathbf{u}}) \\ \mathbf{g}_d(\mathbf{d}) \end{bmatrix} \tag{110}$$

where

$$\begin{aligned} \phi_S(\mathbf{d}, \mathbf{y}_S, \mathbf{u}_S) &= 0, \\ \phi_T(\mathbf{d}, \mathbf{y}_T, \mathbf{u}_T) &= 0 \end{aligned}$$

respectively define the level flight and turning trim conditions, with $\mathbf{y}_S, \mathbf{u}_S$ and $\mathbf{y}_T, \mathbf{u}_T$ denoting the corresponding state and control vectors as described in Chapter 4. Accordingly, in eq. (110):

$$\begin{aligned} \hat{\mathbf{y}} &= \begin{bmatrix} \mathbf{y}_S^T & \mathbf{y}_T^T \end{bmatrix}^T \\ \hat{\mathbf{u}} &= \begin{bmatrix} \mathbf{u}_S^T & \mathbf{u}_T^T \end{bmatrix}^T \end{aligned}$$

The level flight state vector includes the condition of zero angular velocity, as well as all the conditions on the remaining states pertaining to level flight as discussed in Chapters 3

and 4. The state vector for turning flight is defined by the same velocity V considered for level flight and an assigned angular velocity Ω which is specified by selecting a value for the load factor n .

The third constraint in eq. (110) is:

$$T(\mathbf{d}) - T^* \leq 0 \quad (111)$$

which expresses a condition on the maneuvering time for the heading-change maneuver considered in the previous chapter. Specifically, T denotes the maneuvering time corresponding to the optimal heading-change maneuver obtained using the trajectory optimization code. The result corresponds to a given configuration \mathbf{d} , and to initial and final trim states corresponding to level flight at velocity V . Hence the maneuver begins and ends at trimmed states with a vehicle velocity V coincident to the one considered as an input to the level flight trim constraint. The maneuver constraint imposes for T to be smaller than a predefined value T^* . Reducing the value of T^* makes the constraint more stringent, and more influential on the final solution.

The final conditions:

$$\mathbf{g}_t(\mathbf{d}, \hat{\mathbf{y}}, \hat{\mathbf{u}}) < 0$$

$$\mathbf{g}_d(\mathbf{d}) < 0$$

impose bounds on the cavity dimensions and on the design variables as previously indicated. The range D as described in Chapter 4 is selected as the objective:

$$D = C(\mathbf{d}, \hat{\mathbf{y}}, \hat{\mathbf{u}}).$$

6.3 Exploration of the Design Space

The range during level flight as an objective has shown to behave quite regularly in the initial optimization considered in Chapter 4. This clearly leads to an optimization problem which is easy to solve and does not typically suffer from the presence of local minima. An example of variation of range in terms of two design parameters (V and d_c) was shown in fig. 40. The introduction of turning trimmed flight as a constraint does not introduce significant

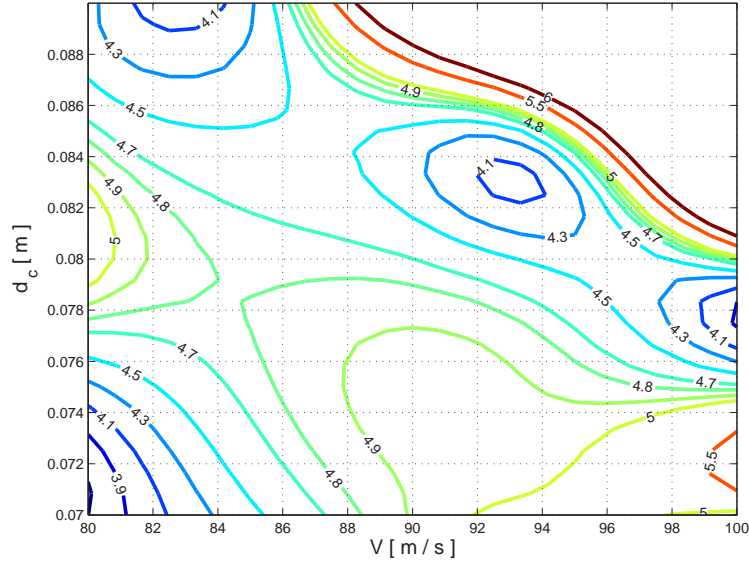


Figure 72: Variation of the minimum flight time in terms of V and d_c for a heading-change maneuver.

complexity, while the addition of the minimum maneuver time complicates the problem. In fact, the constraint introduced by the maneuvering time is characterized by a complex nonlinear behavior which affects the design space. Figure 72 shows for example the variation of the minimum flight time for the heading-change maneuver in terms of V and cavitator diameter d_c . Depending on the minimum time T^* selected in eq. (110), the maneuvering constraint may produce a non-convex and/or discontinuous design space. This is illustrated in fig. 73. Selecting $T^* = 4.9$ sec generates a single non-convex feasible region, while imposing a smaller time such as $T^* = 4.5$ sec produces three disconnected feasible regions. Figure 73 also depicts as a dot the optimal solution found within the considered ranges for V and d_c , which correspond to the case without turning and maneuvering constraints, or the case when such constraints are loose and not active. It is interesting to note, that this optimal value falls outside of the feasible space when a stricter requirement is imposed on the maneuvering time.

In general, the multi-modal structure of the design space causes difficulties, in particular when the response surface methodology with polynomial regression is applied. If constraints produce a non-convex and discontinuous feasible design space, the optimization problem

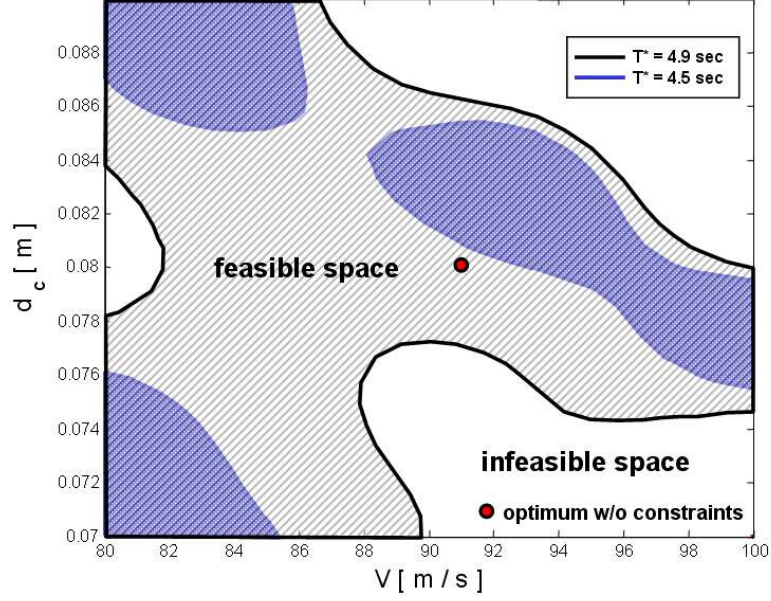


Figure 73: Feasible design regions for different choices of minimum allowed time for the maneuver.

becomes notoriously difficult in terms of global minimum evaluation and computational efficiency.

In this study, we attempt to develop a simple strategy to overcome such difficulties for the cases under consideration. The effectiveness of this simple methodology is evaluated by solving a well-known non-convex and discontinuous problem. In addition, the application of more sophisticated meta-models and optimization strategies such as Genetic Algorithms is still under investigation.

6.4 A Simple Optimization Strategy

6.4.1 Methodology

The developed approach is based on the assumption that the problem under consideration features a regularly varying objective function, and complex constraints. The process consists in several stages. At the first stage, the minimum of the regular objective function is found through an unconstrained optimization, in order to avoid the solution being trapped in local feasible regions. The main idea is illustrated in fig. 74. For example, if one considers the requirement of minimum maneuvering time as $T^* = 4.5$ second, the initial guess may cause the solution to be trapped in a local feasible space (lower left corner of the figure),

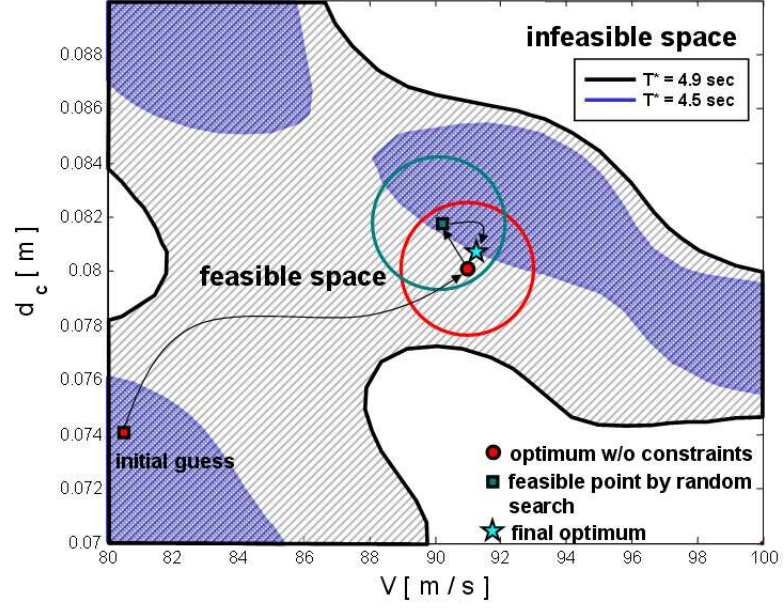


Figure 74: Example illustrating a heuristic optimization strategy.

which is far from the optimum value corresponding to the unconstrained case. At the second stage, constraints are evaluated at the optimum value to verify whether they are violated or not. If this optimum value lies in a feasible region, then the process is considered complete. In contrast, if constraints are violated, a feasible design point is searched in a region neighboring the optimal value, defined by a predetermined radius (red circle in the figure). The radius restricts the design space around the unconstrained global optimum. Once a feasible point is found through a random search, the design space is centered at this feasible point and the constrained optimization is performed in this restricted space (green circle in the figure), whose radial distance from the found feasible design point will be the same as the previous reduced region. The radius of the reduced search space is selected on the basis of some knowledge of the design space. For example the constraints can be evaluated along the optimization path generated during the unconstrained optimization. This information can be used to evaluate the number of transitions between feasible and infeasible regions, and the percentage of feasible points out of the entire number of design points evaluated along the path line. This data can guide the selection of the search radius.

As a result, this method looks for the optimum value in a feasible region close to the

unconstrained optimum value. In addition, it is expected to find the solution with a significantly lower number of constraints evaluation. This simple approach has the above advantages particularly when the optimization problem has the following characteristics: 1) the objective function is well-behaved and continuous over the entire design space, 2) the objective function is computationally inexpensive, 3) the constraints produce a non-convex and discontinuous feasible design space, 4) the evaluation of the constraints is computationally expensive. In addition, upon restriction of the design space, both constraints and objective can be better approximated through response surfaces. For a more robust and efficient method, the choice of the reduction of the design space and random search may be further sophisticated through probabilistic and statistic estimations based on accumulated information about the design space before the second stage optimization.

In the next section, the developed approach is tested on sample examples.

6.4.2 Example

The considered problem will be solved using the developed approach and the results and optimization performance will be compared with those from a standard, gradient-based constrained optimization performed on the full design space.

The following problem is considered

$$\begin{aligned} \min_x \quad & f(x) = \sum_{i=1}^N (x_i - 3)^2 \\ \text{s.t.} \quad & c(x) \leq 0. \end{aligned} \tag{112}$$

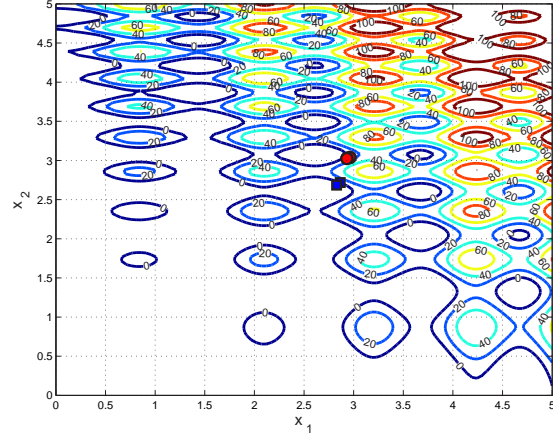
where

$$c(x) = 50 \left(\sum_{i=1}^N \sin(\omega_i x_i)^2 + \sum_{i=1}^N (x_i)^2 + \left(\sum_{i=1}^N x_i \right)^2 \right) - c_0$$

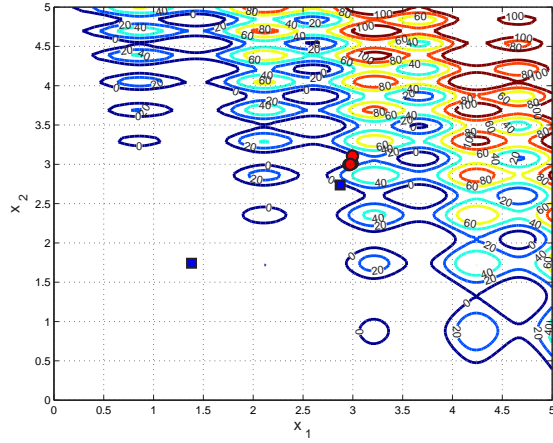
and

$$\omega_1 = \frac{2\pi}{1 + |x_1|^{1/3}}, \quad \omega_i = \frac{2\pi}{1 + |x_i|}$$

In eq. (112), N is the number of design variables, while ω_i and c_0 are parameters which define the shape of the constraints. Two problems are solved for $N = 3, 4$, and values of c_0 respectively equal to 150, and 250. Finally ω_i varies such that the wavelength of the constraint decreases for increasing distance of the design points from the origin ($x_i = 0, i =$



(a) N=3



(b) N=4

Figure 75: Design space and solutions: red circle point is the solution from the developed method, while the blue square indicates solutions found through the standard gradient method.

$1, \dots, 4$). The objective function has a global minimum at $x_i = 3, i = 1, \dots, 4$ when the constraints are neglected.

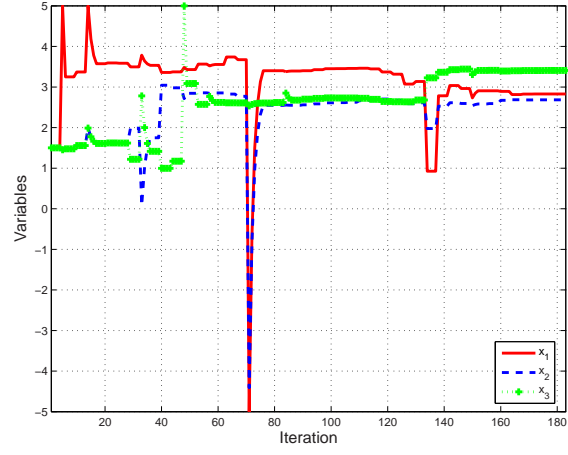
Figure 75 shows the variation of the design space in terms of two design variable x_1, x_2 . For visualization purposes, the design space is presented for $x_3 = x_4 = 0$. In the figures, the solutions given by this heuristic approach are denoted by red circle points, while the solutions given by the standard approach are denoted by the blue squares. Also, Tables 28 and 29 present optimal solutions and computational efficiency in terms of total number of function calls according to method and initial guess (i.g.).

Table 28: Comparison of solutions between standard and heuristic methods for $N = 3$.

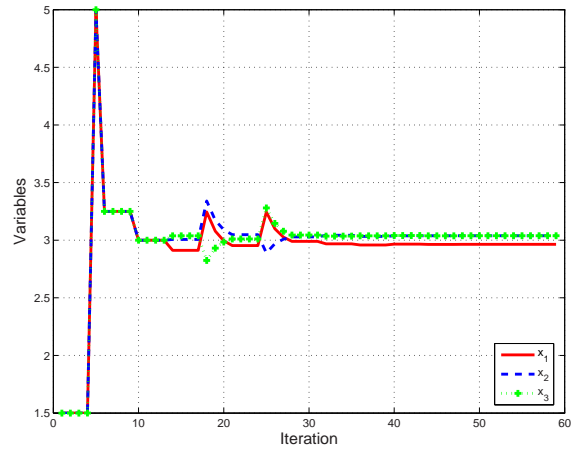
	f	x_1	x_2	x_3	obj. calls	con. calls
i.g.		0	0	0		
standard	0.1770	2.8648	2.7183	2.7183	98	98
heuristic	0.0043	2.9638	3.0384	3.0384	70	78
heuristic & RSM	0.0075	2.9321	3.0284	3.0456	50	28
i.g.		1.5	1.5	1.5		
standard	0.2954	2.8281	2.6841	3.4076	183	183
heuristic	0.0043	2.9638	3.0384	3.0384	59	62
heuristic & RSM	0.0062	2.9318	3.0248	3.0302	48	33

Table 29: Comparison of solutions between standard and heuristic methods for $N = 4$.

	f	x_1	x_2	x_3	x_4	obj. calls	con. calls
i.g.		0	0	0	0		
standard	0.2248	2.8730	2.7363	2.7363	2.7363	84	84
heuristic	0.0019	2.9597	2.9941	3.0103	3.0103	70	82
heuristic & RSM	0.0124	2.9958	3.1050	3.0077	3.0365	71	35
i.g.		1.5	1.5	1.5	1.5		
standard	4.6659	1.3810	1.7414	2.4075	2.6687	134	134
heuristic	0.0004	2.9930	3.0114	3.0114	3.0114	79	81
heuristic & RSM	0.0116	2.9748	2.9999	3.0001	3.1049	53	41



(a) standard approach



(b) heuristic approach

Figure 76: Evolution of design variables during optimization procedure for $N = 3$ with i.g. $x_1 = x_2 = x_3 = 1.5$.

The solutions obtained through the standard approach tend to be trapped by local minima and the quality of the solution depends on the initial guess. In contrast the two-step approach seems to be effective in handling the complexity introduced by the constraint, both in terms of quality of the solution and of number of required function calls. The developed approach is also tested in conjunction with the RSM method, specifically a second-order polynomial regression based on D-optimal sampling points available in MATLAB©, which uses coordinate exchange algorithms to minimize the generalized variance of the parameter estimators [73]. The solutions obtained show a good accuracy and efficiency in terms of number of function calls. Figure 76 shows the evolution of the design variables during the optimization iterations corresponding to standard optimization and the developed method without RSM. Figure 76 (b) shows that the first stage of optimization process (without considering constraints) reaches the optimum solution with a small number of function calls (13) due to the convexity of the objective function, while the second stage of the process successfully proceeds to find the feasible optimum solution with active constraints.

6.5 Optimization results

6.5.1 Preliminary optimization with reduced set of design variables

A preliminary optimization with a reduced number of design variables (V and d_c) is carried out for fins-supported flight as performed in Chapter 4. In order to capture the influence of various constraints on maximum range, several cases are conducted with increasing requirements on turning load factor n , and on maneuvering time T^* . As a first case, the optimization is carried out with all constraints being relaxed, i.e. with sufficiently low load factor and large maneuvering time. Results are presented in Tables 30 and 31. As one might expect, the solution of the optimization with highly relaxed constraints coincides with the solution obtained Chapter 4 (see Table 5 and 6). Figure 77 shows the evolution of objective, constraints, and design variables during the optimization process. In fig. 77 (b), constraints related to trim conditions represent the squared norm $\|\mathbf{f}\|^2$ of the residuals of Euler's equation (eq. (65)), constraints related to vehicle weight are normalized by 100 kg as : $\frac{m}{100} - \frac{m_{ub}}{100}$ for upper bound and $\frac{m_{lb}}{100} - \frac{m}{100}$ for lower bound, and the maneuvering constraint

Table 30: Reduced optimal design configuration with relaxed constraints.

Dimension	nominal	optimal	lower bound	upper bound	unit
d_c	0.08	0.0404	0.02	0.10	m
V	78	172.0734	76	200	m/s
Constraints					
Load factor		n	1.1		
Maneuvering time		T^*	40 sec		

Table 31: Performance of reduced optimal vehicle with relaxed constraints.

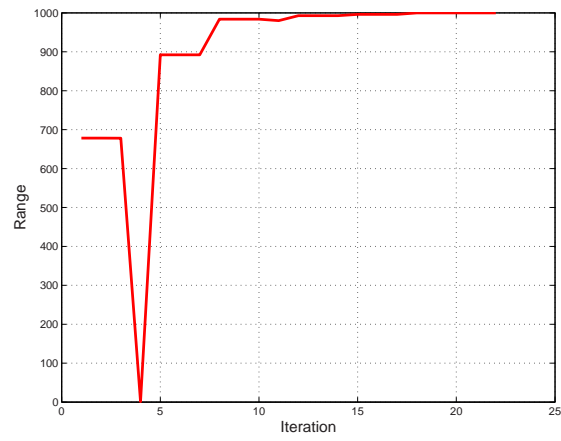
	Nominal	Optimal	unit	[%]
D	638.7	999.9	m	+ 56.5 %
T	4.9927	5.5508	sec	+ 11.2%
V	78	172.0734	m/s	+ 120.6 %
δ_T	18.3176e+3	25.8036e+3	N	+ 40.9 %
m	150	149.9452	kg	- 0.04 %

is plotted as $\frac{T}{T^*} - 1$. Also, all normalized constraints values are set to 1 in case of violation. During the optimization process none of the constraints are active except for one instance at iteration 4, when the vehicle configuration cannot even support level trim. The design variables in fig. 77 (c) are normalized with respect to the values selected as “nominal”. It should be kept in mind that without achieving level trim, turning flight and maneuvering conditions cannot be obtainable.

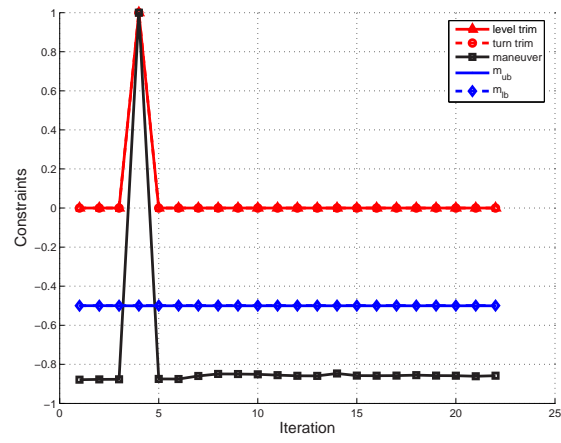
As a second case, the optimization is performed with relatively strict constraints, i.e. with higher load factor and smaller maneuvering time. Results are presented in Tables 32 and 33. The achieved performance is reduced by the active constraints. The histories of objective, constraints and design variables are shown in fig. 78, which clearly shows how the

Table 32: Reduced optimal design configuration with active constraints.

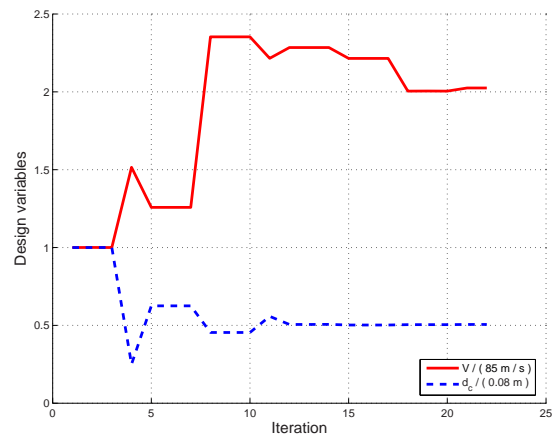
Dimension	value	lower bound	upper bound	unit
d_c	0.0432	0.02	0.10	m
V	175.8683	76	200	m/s
Constraints				
Load factor		n	2	
Maneuver time		T^*	5.5 sec	



(a) Range

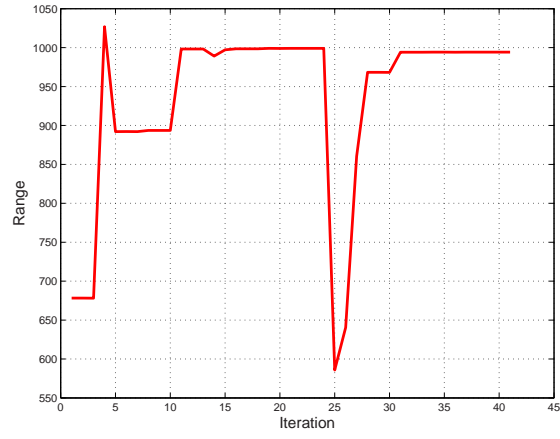


(b) Constraints

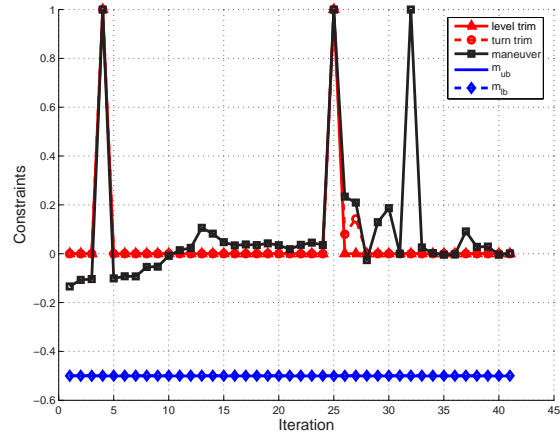


(c) Design variables

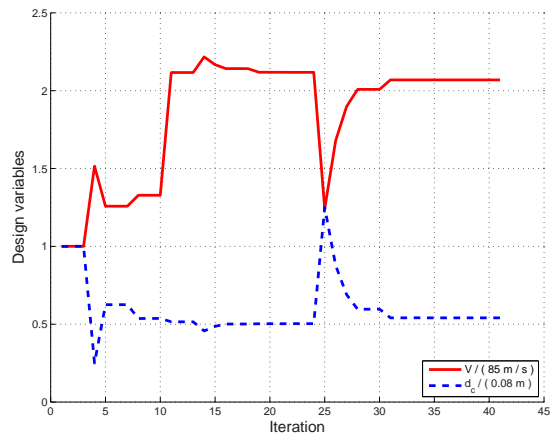
Figure 77: Evolution of objective, constraints, and design variables during optimization process with relaxed constraints.



(a) Range



(b) Constraints



(c) Design variables

Figure 78: Evolution of objective, constraints, and design variables during optimization with active constraints.

Table 33: Performance of reduced optimal vehicle with active constraints.

	Nominal	Optimal	unit	[%]
D	638.7	994.2	m	+ 55.7%
T	4.9927	5.4764	sec	+ 9.7%
V	78	175.8683	m/s	+ 125.5%
δ_T	18.3176e+3	26.5258e+3	N	+ 44.8 %
m	150	149.9479	kg	- 0.03%

optimization is affected by the tightly active constraints, and particularly by the constraint on the maneuvering time. In addition, the figure indicates that the maneuvering time is strongly conflicting with the vehicle range.

6.5.2 Optimization with full set of design variables

The optimization is then performed by considering the full set of design variables. As with the reduced optimization cases, the optimization is first performed with relaxed constraints and then with strict constraints.

The results of the optimization with relaxed constraints are presented in Tables 34 and 35. In the same way, the solution of the optimization with highly relaxed constraints coincides with the solution obtained in Chapter 4 (see Table 7 and 8). In addition to the same improvement in velocity, thrust and range, the optimal vehicle also produces a 23.7% reduction in maneuvering time. The obtained vehicle configuration shows that the mass coincides with the imposed upper bound, while the size of control surfaces coincides with the lower bound. Figure 79 (a) shows the history of constraints during optimization process, in which the occurrence of active constraints is low.

As a second case, the optimization is performed with relatively strict constraints. These results are presented in Tables 36 and 37, where stricter constraints reduce improvement in performance. Figures 79 (b) and (c) respectively show the history of constraints by heuristic and standard approaches in the beginning stage of the optimization process. With such strict constraints, violations are frequent and the standard optimization in particular suffers from lack of convergence. Figure 80 shows the optimized configurations for both cases.

Table 34: Optimal design configuration with relaxed constraints.

Dimension	value	lower bound	upper bound	unit
d_c	0.0400	0.04	0.11	m
L_{fin}	0.1500	0.15	0.25	m
x_{fin}	2.2975	L_{cone}	$L_{cone} + L_{fuse}$	m
R_{veh}	0.0957	0.05	0.15	m
L_{veh}	4.0823	3.5	4.5	m
L_{cone}	0.4082	0.1 L_{veh}	0.9 L_{veh}	m
L_{aft}	0.0798	0.01 L_{veh}	0.1 L_{veh}	m
V	112.4102	76	120	m/s
m	160.0	140	160	kg
Constraints				
Load factor		n	1.1	
Maneuver time		T^*	40 sec	

Table 35: Performance of optimal vehicle with relaxed constraints.

	Nominal	Optimal	unit	[%]
D	638.7	1570.5	m	+ 145.9%
T	4.9927	3.8070	sec	- 23.7 %
V	78	112.4102	m/s	+ 44.1%
δ_T	18.3176e+3	11.4524e+3	N	- 37.5 %
m	150	160.0	kg	+ 6.7 %

Table 36: Optimal design configuration with active constraints.

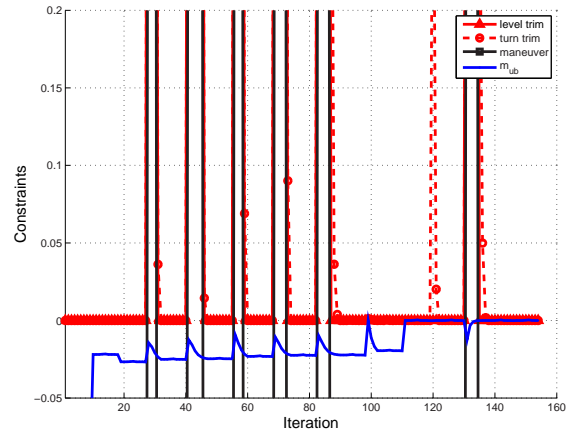
Dimension	value	lower bound	upper bound	unit
d_c	0.0412	0.04	0.11	m
L_{fin}	0.1508	0.15	0.25	m
x_{fin}	2.4486	L_{cone}	$L_{cone} + L_{fuse}$	m
R_{veh}	0.0943	0.05	0.15	m
L_{veh}	4.1244	3.5	4.5	m
L_{cone}	0.4370	0.1 L_{veh}	0.9 L_{veh}	m
L_{aft}	0.1013	0.01 L_{veh}	0.1 L_{veh}	m
V	112.7372	76	120	m/s
m	155.8	140	160	kg
Constraints				
Load factor		n	2	
Maneuver time		T^*	4.5 sec	

Table 37: Performance of optimal vehicle with active constraints.

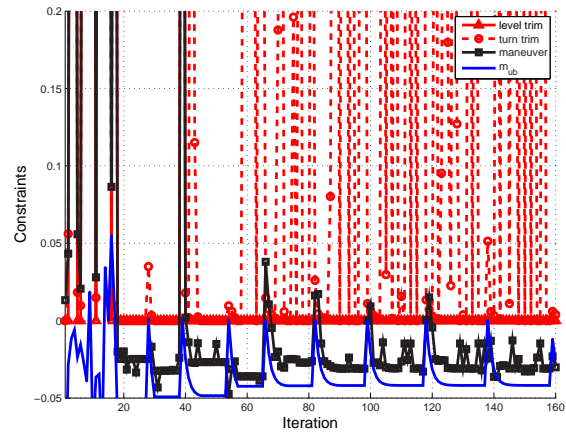
	Nominal	Optimal	unit	[%]
D	638.7	1512.2	m	+ 136.8 %
T	4.9927	4.3612	sec	- 12.6 %
V	78	112.7372	m/s	+ 44.5 %
δ_T	18.3176e+3	11.6169e+3	N	- 37.9 %
m	150	155.8	kg	+ 3.9 %

In order to identify how the constraints are active and how these affect the final optimal solution, optimization is carried out with different requirements on the maneuvering time T^* and, with $n = 2$. The results are listed in Table 38. In all cases, the same lower and upper bounds considered in Table 34 are applied for velocity, design variables and vehicle weight. The results show how the primary performance is adjusted by the imposed requirements on maneuvering time. As the required maneuvering time decreases (more stringent), the performance of the vehicle decreases. The preliminary study shows that the constraints produce cross-coupling effects on the primary performance. For example, the history of active constraints of turn rate and vehicle weight changes due to different optimization path caused by maneuvering time constraint being active. As a result, according to mission profile, we can implicitly investigate trade-offs between various requirements and primary performance.

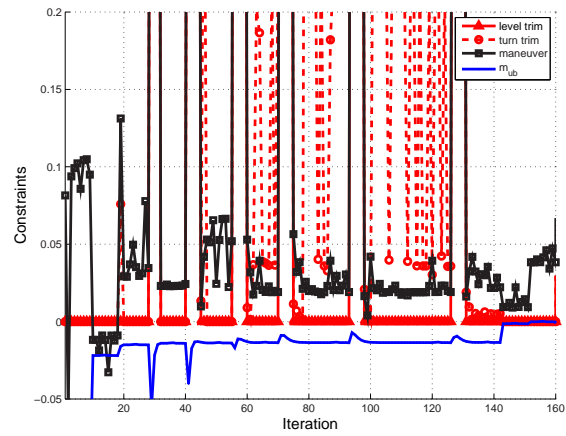
The results shows that the solutions obtained by the simple optimization strategy (cases 1, 2 and 3 in the table) produce a more significant improvement than those by standard approach (cases standard 1 and 2). Furthermore, the results also show the tendency that the effectiveness of the simple approach increases as the constraints are more stringent. This implies the two facts. First, the design space restricted by the considered requirements on turn rate and maneuvering time is a discontinuous and multi-modal surface. Second, the considered simple strategy is also effective in our problem.



(a) Relaxed constraints



(b) Strict constraints

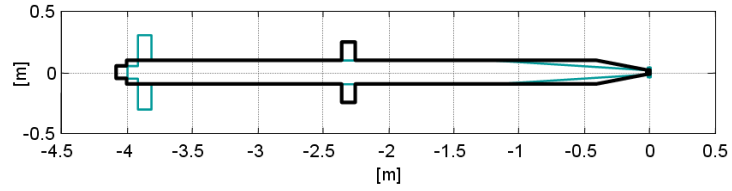


(c) Strict constraints (standard approach)

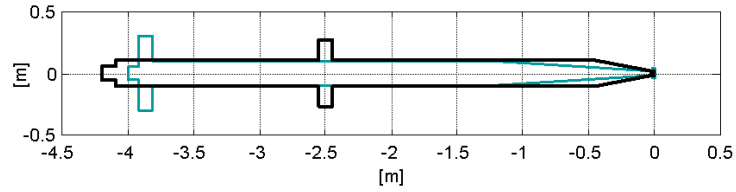
Figure 79: Evolution of constraints during optimization process.

Table 38: Performance of optimal vehicle with various constraint limitations

Performances						Constraints	
Cases	D (m)	T (sec)	V (m/s)	δ_T (N)	m (kg)	n	T^* (sec)
1	1551.4	4.5596	111.8540	11.3672e+3	157.7	2	5.50
2	1512.2	4.3612	112.7372	11.6169e+3	155.8	2	4.50
3	1498.0	4.0918	112.3307	11.3822e+3	151.8	2	4.25
standard 1	1535.1	4.5892	113.5646	11.7217e+3	158.4	2	5.50
standard 2	1450.0	4.4462	120.0000	13.0621e+3	157.8	2	4.50



(a) Relaxed constraints $n = 1.1$ and $T^* = 40$ sec



(b) Strict constraints $n = 2$ and $T^* = 4.5$ sec

Figure 80: Optimal configurations of supercavitating vehicles.

6.6 *Conclusions*

The vehicle configuration is optimized by integrating several operational requirements in the optimization process. Specifically, trim conditions in level and turning flight, as well as a heading-change maneuver are considered as constraints in a system-level optimization which seeks to maximize range during straight level flight. The requirements on turning performance and maneuverability affect the final optimal solution when all constraints are active based on the imposed limitations. Strict requirements reduce the amount of improvement in performance as a result of their restricting the feasible design space, while the solutions with relaxed constraints approach those previously obtained during the optimization process without constraints. The integrated approach provides a framework allowing designers to identify trade-offs as a result of conflicting needs defined by several operating conditions.

The results in this chapter show how constraints related to the considered maneuver may introduce significant complexity in the design space, and make the solution of the optimization more difficult. A simple optimization strategy is employed to handle a disconnected design space and to improve the computational efficiency of the process. However, failure to achieve convergence in certain specific cases indicates that the considered approach may still not be robust enough, and suggests the need for additional investigations on alternative optimization techniques better suited for the problem at hand.

Chapter VII

CONCLUDING REMARKS AND RECOMMENDATIONS

7.1 *Conclusions*

The main goal of this work is the development of a simulation-based design tool providing guidelines on basic vehicle configuration, hydrodynamic configuration, and control system for supercavitating vehicles. For this objective, a design tool capable of configurational optimization of the vehicle subjected to operational design requirements is developed.

The fundamental engine of the design tool is a dynamic flight simulator. The flight mechanics model for a 6 DOF rigid vehicle is developed with detailed implementation of hydrodynamic models. Particularly in this research, the interaction of the vehicle with cavity through control surfaces and afterbody is calculated without simplification in order to account for cavity memory effects. Two simplified models, Munzer-Reichardt's and Logvinovich's, are employed to describe the cavity configuration and dynamics. Although they are widely recognized as simplified and highly approximated ones, they can be conveniently used as part of the development of a dynamic flight simulator with merit of computational efficiency and sufficient accuracy for a preliminary study.

Prior to configurational optimization, the developed dynamic flight simulator is first utilized to investigate trim conditions and dynamic characteristics of supercavitating vehicles. The operating conditions, cavity models and their memory effects has significant influence on trim conditions for two classes of trimmed flights: level flight and level turning flight. In particular, the cavity memory effects introduces a favorable stabilizing effect on the dynamic behavior of the vehicle by providing restoring fins and planing forces. Dynamic simulations also show that fins-supported flight is desirable in terms of vehicle stability and control effectiveness, while fins and planing-supported flight shows potential for instability of a diverging oscillatory motion.

The configurational optimization of a supercavitating vehicle is performed to maximize

range, turn rate, and their combination at both trimmed flights, where the trim evaluation process is used as part of an optimization problem. In turn rate case, the maximum turn rate is defined at the corner speed over entire flight envelope, which is significantly different from that of a conventional vehicle due to different hydrodynamic coefficients as well as a unique operational conditions. The optimization process yields design configurations which significantly improve the vehicle range or maximum turn rate at each flight condition. In addition, the solutions of the optimization problem not only provide vehicle configuration, but also the corresponding optimal operating conditions, in terms of velocity and load factor. However optimal configurations indicate that a trade-off between two performances is required due to their conflicting requirements.

The configurational optimization is also applied to maneuvering vehicles employing polynomial regression RSM. The maneuver is identified through the solution of a trajectory optimization problem, which is carried out through a trajectory optimization code developed at the Politecnico di Milano and here integrated as part of the optimization process. The computational cost is reduced through the application of polynomial regression RSM. However, the RSM may suffer from lack of accuracy at the cost of great computational efficiency, while the direct evaluation of maneuver code may suffer from expensive computation as well as local minima due to inherent nonlinearity and multi-modal structure of the design space imposed by maneuvering requirements.

As a final demonstration of integrated design tool, trim conditions in level and turning flight, as well as the considered reference maneuvers are considered as constraints in a system-level optimization which seeks to maximize a selected performance index. In general, the primary objective and constraints will be determined according to the vehicle mission profile. In this work, maximum range is selected as a primary objective, while level and turning trim conditions, and reference maneuver are selected as constraints. Hence the requirements on turning performance and maneuverability affect the final optimal solution as active constraints. For instance, strict requirements reduce amount of improvement in performance by reducing feasible design space. This integrated approach provide remarkable improvement in performance in the preliminary design phase by bringing various design

requirements together without pre-restrained design space. In addition, it provides designers a tool to find trade-offs between conflict design performances. Furthermore, during optimization process, it may play as a useful tool to indirectly explore and identify the existence of conflicts between feasible design spaces, which may vary according to considered performance and requirement. Therefore, this approach potentially gives good information and insight particularly when designers make a decision about a desirable and affordable performance in early stage of design. In current work, constraints related to maneuver are extremely complex and reduce the robustness of optimization. As a conceptual attempt, a simple strategy is developed to increase computational efficiency and improve the capability to capture global optimum for this class of problems. This simple strategy shows better solution with better computational efficiency particularly for our problem.

7.2 *Recommendations for Future Research*

This research has developed a simulation-based design tool to achieve a improved design by integrating various performances and realistic requirements, which particularly includes maneuvering flight in the vehicle configurational optimization. With additional efforts in the following area, the potential advantages of this tool may be further improved.

- *Refined optimization* For a complex design space, a simple optimization strategy and polynomial regression RSM were used for global optimum and computational efficiency. This can be further improved with a more accurate metamodeling (e.g., Kriging) capturing the complexity of constraints and global optimum-searching methodology (e.g., GA). In addition, considering control system such as the numbers of fins and the DOF of the cavitator angle leads to a mixed continuous-discrete variable optimization problem which requires suitable methods including branch and bound or approximation methods.
- *Refined geometric definition of vehicle* In this current work, we used seven variables for vehicle geometry and control surface dimension. This can be further sophisticated through a more refined shape definition and non-dimensional parameter. For example, a common non-dimensional parameter in missile aerodynamics, the fineness ratio

$(L_{veh}/(2R_{veh}))$ can be used. Further, non-dimensional parameter such as $L_{veh}/(d_c)$ can be developed to improve the design process for supercavitating vehicles. Also the restriction on the basic shape by the cone and cylindrical body can be relaxed or specified through topology optimization before configurational (sizing) optimization.

- *Extension of requirements* The posteriori analysis of the structural performance of the optimized vehicles can be added to allow the assessment of the feasibility of the considered configurations from a structural perspective. Also, propulsion limitation as well as sophisticated weight estimation can be included. Particularly, a refined weight estimation must address the influence of system components such as propulsion.
- *Extended refined dynamic simulator* 6 DOF rigid body simulator has been established based on the relatively simple but appropriate hydrodynamic models including cavity memory effects. The work can be extended to fully account for the coupling between flexible body dynamics and the fluid, the cavity and the vehicle controls (aero-servo-elasticity), jet damping and so on. Further refinement may be considered to account for flights in launching stage through developing partial cavity dynamics. Refined vehicle dynamic models along with refined hydrodynamics may influence the dynamic behavior and the stability of the vehicle.
- *Extended maneuvering code* The current trajectory optimization tool developed at the Politecnico di Milano can be further refined. For example, the cavitation number considered as a constant can be relaxed, which affects the vehicle maneuvers particularly during dive-climb and three-dimensional trajectories. In addition, the tool can be essentially extended according to more refined flight simulator. For example, development of flight mechanics model for launching stage can be readily included into trajectory optimization tool through multi-phase analysis, which will account for vehicle trajectory over entire flight range and hence address more realistic conditions.
- *Stability analysis* The dynamic behavior of the vehicle is highly affected by the cavity memory effects. Therefore a classical dynamic stability based on linearized dynamic

equations is inappropriate for this class of vehicle. A sophisticated stability analysis to account for the memory effects, i.e. the time-lag related effects should be developed.

- *Structural aspect* The more information of vehicle dynamic characteristics from refined models can trigger fundamental structural study of this kind vehicle. From the results of simulation, structural aspects of the vehicle will be further investigated, which will enable structural analysis to be based on appropriate and realistic configurations and loading conditions.

REFERENCES

- [1] CTech Defense Corporation, “RAMICS (Rapid Airborne Mine Clearance System),” <http://www.ctechdefense.com/30mm.html>, May 2006.
- [2] Fleeman, E. L., *Tactical Missile Design*, AIAA Education Series, American Institute of Aeronautics and Astronautics, Inc., Reston, VA, 2001.
- [3] “FAS (Federation of American Scientists),” <http://www.fas.org/man/dod-101/sys/missile/row/shkval.htm>, May 2006.
- [4] Rand, R., Pratap, R., Ramani, D., Cipolla, J., and Kirschner, I. N., “Impact Dynamics of a Supercavitating Underwater Projectile,” *ASME Design Engineering Technical Conferences*, No. DETC97/VIB-39229, ASME, Sacramento, California, September 14-17 1997.
- [5] Ashley, S., “Warp-drive Underwater,” *Scientific American*, May 2001.
- [6] Kirschner, I. N., Fine, N. E., Uhlman, J. S., Kring, D. C., Rosenthal, B. J., Gieseke, T. A., Kuklinski, R., Varghese, A. N., Stinebring, D. R., Dzielski, J. E., Lindau, J. W., and Kunz, R. F., “Supercavitation Research and Development,” *Anteon Corporation - Engineering Technology Center, Naval Undersea Warfare Center Division, Applied Research Laboratory/Penn State University*, Waikiki, HI, October 2001.
- [7] Vasin, A. D., “Some Problems of Supersonic Cavitation Flows,” *45th AIAA/ASME/ASCE/AHS/ASC Structures, 4th International Symposium on Cavitation*, Pasadena CA, June 20-23 2001.
- [8] Ruzzene, M., “Non-axisymmetric buckling of stiffened supercavitating shells: static and dynamic analysis,” *Computers and Structures*, Vol. 82, 2004, pp. 257–269.

- [9] Ruzzene, M., “Dynamic buckling stability of periodically stiffened shells: application to supercavitating vehicles,” *International Journal of Solids and Structures*, Vol. 41, No. 4, 2004, pp. 1039–1059.
- [10] Savchenko, Y. N., “Control of Supercavitation Flow and Stability of Supercavitating Motion of Bodies,” RTO AVT lecture series on supercavitating flows, Von Karman Institute, Brussels Belgium, February 12-16 2001.
- [11] Kirschner, I. N., Rosenthal, B. J., , and Uhlman, J. S., “Simplified Dynamical Systems Analysis Of Supercavitating High-Speed Bodies,” *5th International Symposium on Cavitation(CAV2003)*, No. Cav03-OS-7-005, Osaka,Japan, November 1-4 2003.
- [12] Dzielski, J. and Kurdila, A., “A Benchmark Control Problem for Supercavitating Vehicles and an Initial Investigation of Solutions,” *Journal of Vibration and Control*, Vol. 9, 2003, pp. 791–804.
- [13] Kulkarni, S. S. and Pratap, R., “Studies on the dynamics of a supercavitating projectile,” *Applied Mathematical Modelling*, Vol. 24, 2000, pp. 113–129.
- [14] Abed, E. H., Balachandran, B., and Lin, G., “Control of supercavitating bodies and bodies with partial cavity,” The Institute for Systems Research, University of Maryland College Park, presentation material at ONR Meeting, June 2005.
- [15] Milwitzky, B., “Generalized theory for seaplane impact,” NACA Technical Report 1103, Naval Surface Weapons Center, White Oak Laboratory, 1952.
- [16] Goel, A., *Control Strategies For Supercavitating Vehicles*, Master’s thesis, University Of Florida, 2002.
- [17] Kirschner, I. N., Kring, D. C., Stokes, A. W., Fine, N. E., and James S. Uhlman, J., “Control Strategies for Supercavitating Vehicles,” *Journal of Vibration and Control*, Vol. 8, 2002, pp. 219–242.

- [18] Ruzzene, M. and Soranna, F., “Impact Dynamics of Stiffened Elastic Supercavitating Underwater Vehicles,” *Journal of Vibration and Control*, Vol. 10, No. 2, 2004, pp. 243–267.
- [19] Choi, J.-Y., Ruzzene, M., and Bauchau, O. A., “Dynamic Analysis of Flexible Supercavitating Vehicles Using Modal-Based Elements,” *Simulation-Transactions of The Society For Modeling And Simulation International*, Vol. 80, No. 11, 2004, pp. 619–633.
- [20] Alyanak, E., Venkayya, V., Grandhi, R., and Penmetsa, R., “Structural response and optimization of a supercavitating torpedo,” *Finite Elements in Analysis and Design*, Vol. 41, 2005, pp. 563–582.
- [21] Alyanak, E., Grandhi, R., and Penmetsa, R., “Optimum design of a supercavitating torpedo considering overall size, shape, and structural configuration,” *International Journal of Solids and Structures*, Vol. 43, 2006, pp. 642–657.
- [22] Ahn, S. S. and Ruzzene, M., “Optimal Design Of Cylindrical Shells For Enhanced Buckling Stability: Application To Supercavitating Underwater Vehicles,” *Finite Elements in Analysis and Design*, Vol. 42, 2006, pp. 967–976.
- [23] Betts, J. T., “Survey of Numerical Methods for Trajectory Optimization,” *Journal of Guidance, Control, And Dynamics*, Vol. 21, No. 2, 1998, pp. 193–207.
- [24] Ranta, J., *Optimal Control and Flight Trajectory Optimization Applied To Evasion Analysis*, Master’s thesis, Helsinki University of Technology, Espoo, FINLAND, March 2004, Licentiate Thesis.
- [25] Seywald, H., Cliff, E. M., and Well, K. H., “Optimal Trajectories for an Aircraft Flying in the Vertical Plane,” *Journal of Guidance, Control, and Dynamics*, Vol. 17, No. 2, 1994, pp. 389–398.
- [26] Bulirsch, R., Montrone, F., and Pesch, H. J., “Abort Landing in the Presence of Windshear as a Minimax Optimal Control Problem, Part 1: Necessary Conditions,” *Journal of Optimization Theory and Applications*, Vol. 70, No. 1, 1991, pp. 1–23.

- [27] Bulirsch, R., Montrone, F., and Pesch, H. J., “Abort Landing in the Presence of Windshear as a Minimax Optimal Control Problem, Part 2: Multiple Shooting and Homotopy,” *Journal of Optimization Theory and Applications*, Vol. 70, No. 2, 1991, pp. 223–254.
- [28] Bottasso, C. L., Croce, A., Leonello, D., and Riviello, L., “Optimization of Critical Trajectories for Rotorcraft Vehicles,” *Journal of the American Helicopter Society*, Vol. 50, 2004, pp. 165–177.
- [29] Bottasso, C. L., Croce, A., Leonello, D., and Riviello, L., “Rotorcraft Trajectory Optimization with Realizability Considerations,” *Journal of Aerospace Engineering*, Vol. 18, No. 3, 2005, pp. 146–155.
- [30] Haberkorn, T., Martinon, P., and Gergaud, J., “Low-Thrust Minimum-Fuel Orbital Transfer: A Homotopic Approach,” *Journal Of Guidance, Control, And Dynamics*, Vol. 27, No. 6, 2004, pp. 1046–1060.
- [31] Herman, A. L. and Conway, B. A., “Direct Optimization Using Collocation Based on High-Order Gauss-Lobatto Quadrature Rules,” *Journal Of Guidance, Control, And Dynamics*, Vol. 19, No. 3, 1996, pp. 592–599.
- [32] Herman, A. L. and Conway, B. A., “Optimal, Low-Thrust, Earth-Moon Orbit Transfer,” *Journal Of Guidance, Control, And Dynamics*, Vol. 21, No. 1, 1998, pp. 141–147.
- [33] Berend, N. and Talbot, C., “Overview of some optimal control methods adapted to expendable and reusable launch vehicle trajectories,” *Aerospace Science and Technology*, Vol. 10, 2006, pp. 222–232.
- [34] Azimov, D., “Active Rocket Trajectory Arcs: A Review,” *Automation and Remote Control*, Vol. 66, No. 11, 2005, pp. 1715–1732.
- [35] Breitner, M. H., “Robust Optimal Onboard Reentry Guidance of a Space Shuttle: Dynamic Game Approach and Guidance Synthesis via Neural Networks,” *Journal of Optimization Theory and Applications*, Vol. 107, No. 3, 2000, pp. 481–503.

- [36] Milam, M. B., *Real-Time Optimal Trajectory Generation for Constrained Dynamical Systems*, Ph.D. thesis, California Institute of Technology, Pasadena, CA, May 2003.
- [37] Brogan, W. L., *Modern Control Theory*, Prentice-Hall, Inc., Upper Saddle River, NJ, 3rd ed., 1991.
- [38] Sargent, R., “Optimal Control,” *Journal of Computational and Applied Mathematics*, Vol. 124, 2000, pp. 361–371.
- [39] Goldstine, H. H., *A History of the Calculus of Variations from the 17th through the 19th Century*, Studies in the History of Mathematics and Physical Sciences 5, Springer-Verlag, New York, 1980.
- [40] Arthur E. Bryson, J. and Ho, Y.-C., *Applied Optimal Control*, Hemisphere Publishing Corporation, New York, 1975.
- [41] Bryson, A. E., *Dynamic Optimization*, Prentice Hall, 1998.
- [42] Hestenes, M. R., *Calculus Of Variations And Optimal Control Theory*, Applied Mathematics Series, John Wiley and Sons, INC., New York, 1966.
- [43] Hull, D. G., “Conversion of Optimal Control Problems into Parameter Optimization Problems,” *Journal Of Guidance, Control, And Dynamics*, Vol. 20, No. 1, 1997, pp. 57–60.
- [44] Ross, I. M. and Fahroo, F., “A Perspective On Methods For Trajectory Optimization,” *AIAA/AAS Astrodynamics Specialist Conference and Exhibit*, No. AIAA 2002-4727, AIAA, Monterey, CA, August 5-8 2002.
- [45] Kamada, R., Ruzzene, M., and Bottasso, C. L., “Trajectory Optimization Strategies for Supercavitating Underwater Vehicles,” *45th AIAA/ASME/ASCE/AHS/ASC Structures, Structural Dynamics and Materials Conference*, No. AIAA 2004-1593, AIAA, Palm Springs, California, April 19 - 22 2004.

- [46] Ruzzene, M., Kamada, R., Bottasso, C. L., and Scorcelletti, F., "Trajectory Optimization Strategies for Supercavitating Underwater Vehicles," *Journal of Vibration and Control*, 2007, To appear.
- [47] Kamada, R., *Trajectory Optimization Strategies For Supercavitating Vehicles*, Master's thesis, Georgia Institute of Technology, Atlanta, GA, November 2004.
- [48] Bottasso, C. L., Borri, M., and Trainelli, L., "Integration of Elastic Multibody Systems by Invariant Conserving/Dissipating Schemes. Part I Formulation," *Computer Methods in Applied Mechanics and Engineering*, Vol. 190, 2001, pp. 3669–3699.
- [49] Savchenko, Y. N., "Supercavitation - Problems And Perspectives," RTO AVT lecture series on supercavitating flows, National Academy of Sciences - Institute of Hydromechanics, Kyiv, Ukraine, 2001.
- [50] Munzer, H. and Reichardt, H., *Rotational symmetric source-sink bodies with predominantly constant pressure distributions[sic]*, ARE Translation 1/50, Aerospace Research Establishment, England, (as described in May, 1975).
- [51] Garabedian, P. R., "Calculation of axially symmetric cavities and jets," *Pacific Journal of Mathematics*, Vol. 4, 1956, pp. 611–684.
- [52] Kiceniuk, T., "An experimental study of the hydrodynamic forces acting on a family of cavity producing conical bodies of revolution inclined to the flow," CIT Hydrodynamic Report E-12.17, California Institute of Technology, Pasadena, CA, 1954.
- [53] May, A., "Water Entry and the Cavity-Running Behavior of Missiles," SEAHAC Technical Report 75-2, Naval Surface Weapons Center, White Oak Laboratory, Silver Spring, MD, 1975.
- [54] Logvinovich, G. V., "Hydrodynamics of Free-Boundary Flow," Tech. rep., U.S. Department of Commerce, Washington, DC, 1972, translated from the Russian(NASA-TT-F-658).

- [55] Vasin, A. D., “The Principle of Independence of the Cavity Sections Expansion (Logvinovich’s Principle) as the Basis for Investigation on Cavitation Flows,” RTO AVT lecture series on supercavitating flows, Von Karman Institute, Brussels Belgium, February 2001.
- [56] Uhlman, J. S., Fine, N. E., and Kring, D. C., “Calculation of the Added Mass and Damping Forces on Supercavitating Bodies,” *4th International Symposium on Cavitation (CAV2001)*, Pasadena, CA, 2001.
- [57] Hassan, S. E., “Analysis of Hydrodynamic Planing Forces Associated With Cavity Riding Vehicles,” private communication.
- [58] Karman, T. V., “The impact of seaplane floats during landing,” Tech. rep., NACA TN 321, 1929.
- [59] Logvinovich, G. V., “Some Problems in Planing Surfaces [sic],” Trudy TsAGI 2052, Central Aero and Hydordyanmics Institute, Moscow, Russia, 1980, translated from Nekotoryyi voprosy glissirovaniya ikavitatsii [Some problems in planing and cavitation].
- [60] White, F. M., *Fluid Mechanics*, McGraw-Hill, New York, 3rd ed., 1994.
- [61] Ikeda, Y. and Katayama, T., “Porpoising Oscillations of Very-High-Speed Marine Craft,” *Philosophical Transactions: Mathematical, Physical and Engineering Sciences*, Vol. 358, No. 1771, 2000, pp. 1905–1915.
- [62] Asselin, M., *An Introduction to Aircraft Performance*, AIAA Education Series, American Institute of Aeronautics and Astronautics, Inc., Reston, VA, 1997.
- [63] Thomson, W. T., *Introduction To Space Dynamics*, Dover Publications, INC., New York, 2nd ed., 1986.
- [64] Hill, P. G. and Peterson, C. R., *Mechanics and Thermodynamics of Propulsion*, Addison-Wesley Publishing Company, Inc., 2nd ed., 1992.
- [65] Park, G.-J., Lee, T.-H., Lee, K. H., and yeon Hwang, K., “Robust Design: An Overview,” *AIAA Journal*, Vol. 44, No. 1, 2006, pp. 181–191.

- [66] Scorcelletti, F., *OTTIMIZZAZIONE DI TRAIETTORIE PER VEICOLI IN REGIME DI SUPERCAVITAZIONE (Trajectory Optimization For Vehicles In Supercavitation Regime)*, Master's thesis, Politecnico di Milano, Milan, Italy, 2006.
- [67] Betts, J. T., "Practical Methods for Optimal Control Using Non-Linear Programming," *SIAM*, 2001.
- [68] Barclay, A., Gill, P. E., and Rosen, J. B., "SQP Methods and their Application to Numerical Optimal Control," Report na 97-3, Department of Mathematics, University of California, San Diego, CA, 1997.
- [69] Renegar, J., "A Mathematical View of Interior Point Methods in Convex Optimization," *SIAM, Philadelphia*, 2001.
- [70] Gill, P. E., Murray, W., and Saunders, M. A., *Users Guide for SNOPT Version 7: Software for Large-Scale Nonlinear Programming*, University of California, San Diego and Systems Optimization Laboratory, Stanford University, February 2006.
- [71] Simpson, T. W., Peplinski, J. D., Koch, P. N., and Allen, J. K., "Metamodels for Computer-based Engineering Design: Survey and recommendations," *Engineering with Computers*, Vol. 17, No. 2, 2001, pp. 129–150.
- [72] Frits, A. P., *Formulation of an Integrated Robust Design and Tactics Optimization Process for Undersea Weapon Systems*, Ph.D. thesis, Georgia Institute of Technology, Atlanta, GA, month = December, note = , source = ,, 2004.
- [73] Atkinson, A. C. and Donev, A. N., *Optimum Experimental Designs*, Oxford statistical science series, Oxford Science Publications, New York, 1992.

VITA

Seong Sik Ahn was born in Gokseong, South Korea, in February, 1975. He received his Bachelors degree in Mechanical Engineering in 1997 from Korea University, Seoul, South Korea. After graduation, He had worked for Air Force of Republic of Korea as an officer. After completing the military service, he has joined the School of Aerospace Engineering at the Georgia Institute of Technology in May of 2002 as a grantee for National Scholarship of Studying Abroad for master's degree of aerospace engineering in 2001, where he received a Master of Science degree in Aerospace Engineering in May of 2004 and began a Ph.D. in May of 2004. He will be awarded his Ph.D. in Aerospace Engineering in May of 2007 by this presented work for the requirement of Doctor of Philosophy.